NUMERICAL METHODS FOR CHEMICAL ANALYSIS OF COMPLEX SURFACES

A Dissertation
Presented to
The Academic Faculty

by

Alexander C. Elder

In Partial Fulfillment
of the Requirements for the Degree
Doctor of Philosophy in the
School of Chemistry and Biochemistry

Georgia Institute of Technology
August 2018

Numerical Methods for Chemical Analysis of Complex Surfaces

Approved by:

Dr. Thomas M. Orlando Advisor
School of Chemistry and Biochemistry
Georgia Institute of Technology

Dr. Phillip N. First
School of Physics
Georgia Institute of Technology

Dr. David Sherrill
School of Chemistry and Biochemistry
Georgia Institute of Technology

Dr. Mostafa El-Sayed
School of Chemistry and Biochemistry
Georgia Institute of Technology

Dr. Angus Wilkinson
School of Chemistry and Biochemistry
Georgia Institute of Technology

Date Approved: July 13, 2018

To my grandfather, Dr. Max W. Brachvogel, M.D.

ACKNOWLEDGEMENTS

I would like to thank my advisor, Thom Orlando, for providing a research environment that allowed me to develop a strong foundational skillset and explore various areas of specialization. I also want to thank my girlfriend, Kayleigh Bosco, as well as my parents, Colin and Julie Elder, for their guidance and support. Finally, I would especially like to thank my colleagues: Aaron McKee, Kevin Benham, Souryadeep Bhattacharyya, Brant Jones, Alex Aleksandrov, Micah Schaible, Chris Bennett and Reuben Gann for six years of excellent collaboration that led to this thesis.

TABLE OF CONTENTS

LIST OF TABLES

LIST OF FIGURES

LIST OF SYMBOLS AND ABBREVIATIONS

TPD	Temperature Programmed Desorption
XPS	X-ray photoelectron spectroscopy
CuBDC	Copper Benzenedicarboxylate
ZnBDC	Zinc Benzenedicarboxylate
CoBDC	Cobalt Benzenedicarboxylate
MOF	Metal-Organic Framework
UHV	Ultra High Vacuum
P	Chamber Pressure
t	Time
C	Surface concentration
A	Sample Area
R	Universal gas constant
V	Chamber volume
T	Temperature
S	Pump rate
ν	Frequency Coefficient
θ	Fractional surface coverage
α	Temperature ramp rate
k	Kinetic order
E_a	Activation enthalpy
s	Signal
μ	Mean
σ	Standard deviation

Erf	Error function
a_i	Dirichlet parameters
b_i	Skew parameters, heterogeneous Raman broadening parameters
D	Diffusion coefficient
k_{rev}	Transient adsorption coefficient
ρ_i	Density of surface site i
λ	Mean free path
k_B	Boltzmann constant
m_{gas}	Mass per gas molecule
δ	Topological diffusion coefficient correction
L	Langmuir
N	Normal distribution
ϕ	Normal probability density function
Φ	Normal cumulative density function
Dir	Dirichlet probability density function
$\boldsymbol{\Upsilon}$	Hyperparameter vector
$\boldsymbol{\pi}$	Bayesian parameter vector
Q	Approximate posterior distribution
q_i	Factors of approximate posterior distribution
$\boldsymbol{\psi}$	Variational parameter vector
h	Shannon information content
$\mathbb{H}$	Shannon entropy
$D_{KL}(Q\|\|P)$	Kullback-Leibler Divergence
F	Bayesian free energy function

∇	Gradient operator
η_i	Raman intensity parameter
p_i	Raman peak position parameter
$\bar{s}$	Normalized signal
z	Normalization function
Σ	Covariance matrix
τ	Precision parameter
α	Gamma shape parameter
β	Gamma rate parameter
Γ	Gamma function
$\psi^{(0)}$	Digamma function
$\psi^{(1)}$	First polygamma function
$\mathbf{1}_{n\times 1}$	n-dimensional vector of ones
$\mathbf{0}_{n\times 1}$	n-dimensional vector of zeros
DMF	N,N-dimethylformamide
BDCA	1,4 benzenedicarboxylate

SUMMARY

Temperature programmed desorption (TPD) is a classic surface science experiment that provides information regarding gas adsorption thermodynamics and desorption kinetics. Conventional TPD data analysis methods are inadequate for desorption processes involving complex surfaces, such as those involving porous materials or heterogenous mixtures. To address this, numerical methods were developed for analysis of TPD from such materials. These signals, which consist of overlapping time-resolved mass spectra, are governed by dynamic chemical processes. The core innovation involves nonlinear regression of numerically integrated kinetic models in a method inspired by deconvolution analysis of X-ray photoelectron spectra. Fundamental details of implementation and accuracy are discussed, and the modeling approach is extended to address porous samples and amorphous surfaces. A probabilistic approach for TPD analysis based on Bayesian machine learning theory is introduced to quantify uncertainty in extracted kinetic parameters. This approach is also modified for application to Gaussian mixture decomposition. These methods are applied to surface analysis of metal-organic frameworks materials with an emphasis on application to membrane separation technologies.

CHAPTER 1. INTRODUCTION

1.1 Context and Motivation

Surface chemistry is of central importance to a wide range of industrial, biological, and environmental processes. These processes, which range from heterogeneous catalysis to surface diffusion and membrane transport phenomena, are governed by the distribution of chemical functionalities that terminate the solid phase.[1] Thermodynamic properties associated with surface chemical structures are typically related to asymmetric bonding conditions such as hydroxyl-bound metals at metal-oxide surfaces.[2] Such bonding motifs are often less stable than the bulk phase and therefore offer the potential for interesting interactions with the components of fluid phases to which they are exposed. The binding of fluid molecules to solid surfaces is called adsorption.[1]

A wide range of experimental methodologies have been developed to characterize the chemical components of exposed solid surfaces. The classical approach to surface science involves the application of ultrahigh vacuum chambers that are evacuated to pressures below 10^{-9} Torr. At sufficiently low pressures, solid surfaces can be cleaned of gases and weakly bound surface terminations. Once exposed, surface-sensitive measurement techniques can be applied to probe its chemical environment. Two of such techniques are X-ray photoelectron spectroscopy (XPS) and temperature programmed desorption (TPD).[3-5] Analysis of data from these experiments can be complicated, but is well-understood for simple surfaces, such as single terminations of single crystals.[3] However, as will be shown in chapter 1, conventional analysis procedures, which are usually some form of nonlinear regression analysis, are either biased or highly

susceptible to overfitting if the surface of interest is sufficiently complex. Temperature programmed desorption, specifically, has very sparse literature pertaining to data analysis for non-ideal samples while commercial software exists for analyzing complex XPS data.

The primary goal of this thesis is to develop methods for quantitative TPD signal analysis comparable to those used for XPS. Parameters extracted from these approaches can be used to infer surface structural information and may be thought of as complimentary to the elemental and bonding information provided by XPS. Quantitative TPD signal decomposition involves extensive application of numerical analysis to desorption kinetic models. Topics will include Runge-Kutta methods for integration of ordinary differential equations, finite difference analysis of partial differential equations, and constrained nonlinear optimization and evolutionary algorithms for global optimization. Once the fitting protocol has been developed and demonstrated, Bayesian methods will be introduced with the goal of reducing overfitting. These algorithms will be demonstrated for TPD data as well as Gaussian fitting, which relates directly to XPS analysis.

Experimental applications of the numerical fitting approaches that have been discussed will involve characterization of metal-organic framework (MOF) surfaces. MOF materials provide an ideal context for demonstrating the applicability of these approaches because they are microporous and contain a large number of possible adsorption sites including internal lattice positions, external sites, and an abundance of crystal defects. Both mass transfer limitation and overlapping signal effects will be considered.

1.2 Thesis Outline

The document is divided into two parts. The first will focus exclusively on quantitative TPD data analysis, which will alternatively be referred to as TPD signal decomposition because the curve is the sum of an ensemble of signals. The second chapter introduces the differential kinetic equations that model the TPD process and numerical approaches to solve them. The breakdown of naïve analysis in the case of complex data is also discussed. Chapter three introduces nonlinear least squares regression analysis and demonstrates its applicability to TPD signals. The problem of overfitting is also discussed. The method developed in this chapter is directly analogous to the widely used XPS deconvolution method and the mathematical complexity and details of implementation of the two methods are compared. Chapter four expands the method developed in chapter three to porous materials where mass transfer limitation impacts the signal shape. This chapter appeared in *Langmuir* under the same title in September 2017.[6] Chapter six introduces Bayesian nonlinear regression and variational Bayesian inference to kinetic and Gaussian signal decomposition. Variational Bayesian inference is applied to desorption profiles of carbon dioxide from copper benzenedicarboxylate (CuBDC) samples to examine the mechanism for the increase in CO_2 affinity exhibited by nanosheet particle morphologies compared to bulk crystals. Software was developed in 2017 and 2018 in C++ to perform this Bayesian analysis of surface signals and a link to its GitHub repository can be found in the appendix. Components of chapters two, three, five, and six will comprise a submission to *The Journal of Physical Chemistry C* in July 2018.[7]

Part 2 includes a single chapter that explores the decomposition of MOF nanomaterials under acid gas exposure. This work was conducted prior to the

development of the variational Bayesian inference software that is the focus of chapters five and six, however it makes extensive use of commercial XPS deconvolution software. Chapter seven was published under the same title in *The Journal of Physical Chemistry C* in April 2018. A brief conclusion and discussion of future work is given in chapter eight.

1.3 References

1. Vannice, A. M., *Kinetics of Catalytic Reactions*; Springer: New York, 2005.
2. Poston, M. J.; Grieves, G. A.; Aleksandrov, A. B.; Hibbitts, C. A.; Darby Dyar, M.; Orlando, T. M., Water Interactions with Micronized Lunar Surrogates Jsc-1a and Albite under Ultra-High Vacuum with Application to Lunar Observations. *J. Geophys. Res. E* **2013**, *118*, 105-115.
3. Jong, A. M. d.; Niemantsverdriet, J. W., Thermal Desorption Analysis: Comparative Test of Ten Commonly Applied Procedures. *Surf. Sci.* **1990**, *233*, 355-365.
4. King, D. A., Thermal Desorption from Metal Surfaces: A Review. *Surf. Sci.* **1974**, *47*, 384-402.
5. Wagner, C. D.; Riggs, W. M.; Davis, L. E.; Moulder, J. F.; Mullenberg, G. E., *Handbook of X-Ray Photoelectron Spectroscopy*; Perkin-Elmer Corporation: Eden Prairie, Minnesota, 1979.
6. Elder, A. C.; Aleksandrov, A. B.; Nair, S.; Orlando, T. M., Interactions on External MOF Surfaces: Desorption of Water and Ethanol from CuBDC Nanosheets. *Langmuir* **2017**, *33*, 10153-10160.
7. Elder, A. C.; Bhattacharyya, S.; Nair, S.; Orlando, T. M., Reactive Adsorption of Humid SO_2 on Metal–Organic Framework Nanosheets. *J. Phys. Chem. C* **2018**, *122*, 10413-10422.

CHAPTER 2. KINETIC MODEL OF TEMPERATURE PROGRAMMED DESORPTION

2.1 Introduction

Surface science seeks to evaluate the chemistry and physics of solid surfaces. These regions are interesting for many reasons owing both to the unique chemistries that arise due to bond-unsaturated surface complexes as well as the crucial role the interface plays in transport processes such as diffusion and heat transfer. Given that for most solids only a vanishingly small fraction of the population of atoms are on the surface, directly measuring interfacial processes is difficult. The importance of surface analysis to industry has resulted in the wide availability of powerful techniques for surface chemical analysis such as X-ray photoelectron spectroscopy and Energy Dispersive X-ray Spectroscopy. While these techniques are valuable in that they are easy to set up with commercially manufactured equipment and data analysis is straightforward with off the shelf software, they suffer from a distinct lack of surface specificity. This is to say, signals from these techniques may be contaminated by emissions from bulk atoms up to 70 nm below the surface depending on the material's density.[1]

TPD provides several advantages over other surface analysis techniques. While there are few commercially manufactured TPD systems, the experiment can be set up fairly easily in labs that are outfitted with general purpose ultra-high vacuum (UHV) equipment.[2] The experiment is based on measuring small-molecule desorption processes under UHV conditions and therefore it does not suffer from surface specificity errors if the surface is impenetrable to the analyte gas.[3] For many test gases, temperatures can be kept low such that the technique is non-destructive. While the main drawback of the

method is that data is very difficult to interpret, TPD signals contain a wealth of chemical information about the sample surface that is needed for engineering industrial products such as catalysts and membranes.[4]

Analysis and interpretation of TPD data f is the primary topic of this thesis. Rather than examining the specific kinetic behavior of known distributions of surface sites with chemically adsorbed species, the focus will be on the determination of distributions of functionalities via inference based on the low temperature desorption behavior of probe gases such as carbon dioxide and water. The experiments considered occur well below room temperature and therefore outside the range of temperatures where dissociative adsorption of covalent molecules might occur.[5] As a result, only first order desorption processes will be considered.

Many methods for quantitative analysis TPD signals have been proposed and applied in the literature.[3-4, 6] These methods tend to perform reasonably well for high phase-purity samples with a small number of distinct adsorption sites. However, their underlying assumptions break down for complex solid surfaces where signals associated with a distribution of similar adsorption sites often overlap. Materials with such surfaces include supported catalysts, nanoparticles, and membrane materials, which are of significant interest to industrial research in chemical manufacturing, electrochemical energy storage, and gas separation and storage.[7-10]

Excellent reviews of existing methods for quantitative analysis of TPD signals can be found elsewhere and different techniques tend to be suited to specific cases.[3, 6] A generally applicable method for TPD signal decomposition will be developed throughout this thesis. The foundation of this technique is the numerical integration of the ordinary

differential equation that governs the TPD process. In this chapter, the properties of this equation will be examined and a simple nonlinear least squares fitting procedure comparable to that of X-ray photoelectron spectra will be introduced. This chapter is foundational in that most of the other chapters build on the concepts introduced here. Some of the ideas will be reintroduced when they are improved upon in later chapters, but it is convenient to cover all of the basics here and to discuss some fundamental weaknesses of the approach.

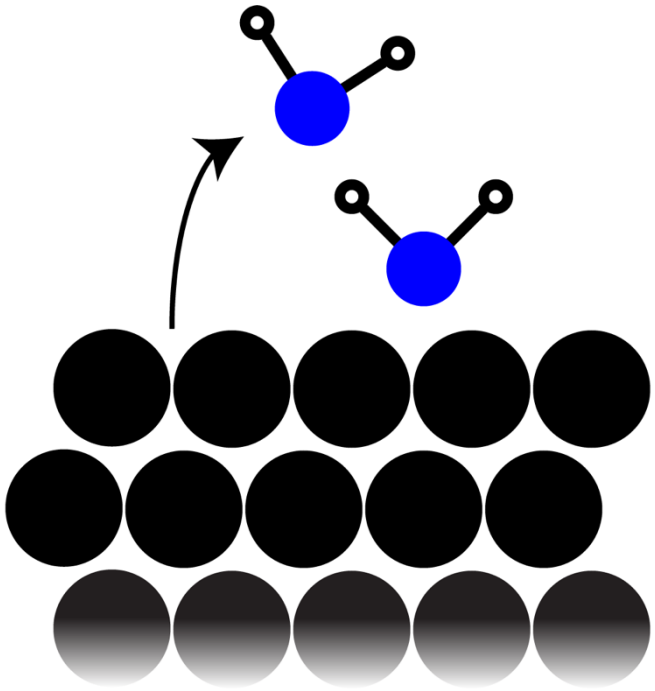

Figure 2.1 Cartoon representation of the desorption of molecular water from a metal surface.

2.2 Experimental Setup

As the name suggests, the fundamental process under consideration in a typical TPD experiment is the breaking of a bond between a gas molecule and a solid surface induced by a linear temperature ramp. A cartoon of this process is shown in Figure 2.1. The surface-gas system is isolated from the ambient conditions of the laboratory inside of a UHV chamber. The solid sample is installed at the end of a cryostat capable of cooling the solid well past the condensation temperature of the analyte gas under vacuum conditions. The desorption process is monitored by a pressure sensor or mass spectrometer located near the sample holder. The sensor is close enough that the molecular diffusion distance from the sample is minimized. UHV ion gauges and mass spectrometers emit charged particles that can induce premature desorption from the sample either via resistive heating or molecular collisions. Thus, the sensor may be installed with a shield to remove ambiguity in the desorption process.

The temperature ramp is accomplished using a high-powered heater installed in the immediate vicinity of the sample. The heater is positioned such that heat transfer is concentrated toward the sample rather than the components of the cryostat to minimize background desorption from the cryostat. The heater is often shielded to prevent radiative heating of cold components that may also contribute to the background. While some background signal is to be expected, interactions between the heater and cold components can lead to feedback effects resulting in chaotic behavior that is difficult to characterize and subtract from the final signal. Figure 2.2 shows a typical TPD chamber setup. An alternative configuration, which uses a small trough for powder samples, will be discussed in chapter 3.

A turbopump is used to pump the chamber to a base pressure below 10^{-9} Torr. The pump is also located close to the sample holder so that desorbing gases are unable to accumulate in the chamber. Prevention of gas accumulation inside the chamber removes the possibility of dynamic equilibrium between the chamber and the sample.

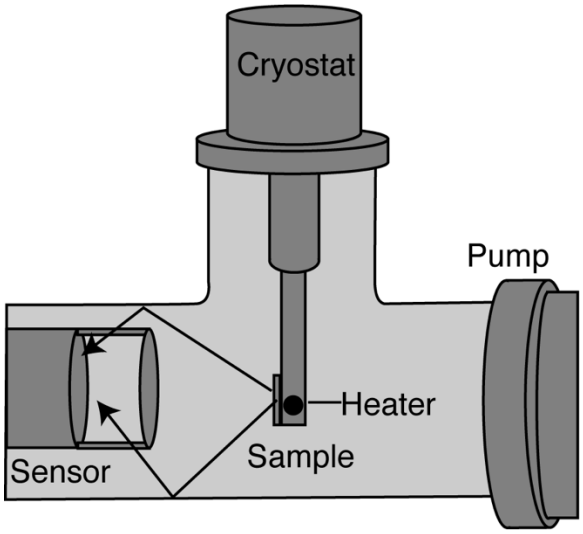

Figure 2.2 Schematic of TPD chamber setup.

The experiment is prepared by cooling the sample below the estimated desorption temperature but above the sublimation point and a calibrated volume of sample gas is introduced to the chamber. After the dose is complete, the pressure is allowed to recover, and the sample is cooled below the sublimation point to minimize surface diffusion processes. The heater is then activated with the aid of a power controller or pre-calibrated circuit such that the temperature increase is linear in time. The pressure in the chamber P varies as a function of time t according to equation 1, where C is the surface concentration, A is the sample area, R is the gas constant, V is the chamber volume, T_g is the temperature of the gas phase, and S is the pump rate.

$$\frac{dP}{dt} = -\frac{dC}{dt}\frac{ART_g}{V} - \frac{SP}{V} \tag{2.1}$$

For a sufficiently high pump rate $\frac{dP}{dt} \ll \frac{SP}{V}$, and the pressure in the chamber recorded by the mass spectrometer is inversely proportional to the desorption rate $P \propto -\frac{dC}{dt}$.[3]

2.3 Polanyi-Wigner Equation

The desorption rate proceeds as a function of temperature according to the Polanyi-Wigner equation, given in equation (2.2). The kinetic order is given by k, the pre-exponential frequency factor is given by $\nu(\theta, T)$, and the activation energy is given by E_a. These dependencies and the signal's sensitivity to errors in this factor will be explored in the next section.

$$\frac{dC}{dt} = C^n \nu(C, T) e^{-\frac{E_a}{RT}} \tag{2.2}$$

As the equation shows, the technique is flexible across varying temperature ranges and kinetic regimes. Intuitively, zeroth order desorption corresponds to ice sublimation, first order corresponds to desorption of physically adsorbed gases, and second order to recombinative desorption of dissociatively adsorbed molecular fragments.[5] Given a linear temperature ramp $\alpha\ [K/s]$, the temperature can be written $T = T_0 + \alpha t$.

An alternative notation applies the concept of the fractional surface coverage $\theta = \frac{C}{C_0}$, which is convenient when the site coverage must be explicitly written in the governing equation-such as in least squares regression. Equation 2.3 gives the desorption rate in terms of fractional coverage. Note that this is proportional to (2.2).

$$\frac{d\theta}{dt} = \theta^k \nu(\theta, T) e^{-\frac{E_a}{R(T_0 + \alpha t)}} \tag{2.3}$$

In the case of a surface with multiple sites, the signal intensity $s(t)$ is inversely proportional to the sum over the desorption rates $\frac{d\theta_i}{dt}$.

$$s(t) \propto \sum_{i=1}^{N} \frac{d\theta_i}{dt} \tag{2.4}$$

$$= \theta^n \nu(\theta, T) e^{-\frac{E_a}{R(T_0+\alpha t)}} \tag{2.5}$$

The frequency factor ν may be interpreted as the surface-adsorbate bond frequency for first order processes $(k = 1)$. In that case it may be very weakly dependent on coverage and temperature but will be assumed to be constant. In the second order processes $(k = 2)$, the frequency factor corresponds to the ratio of the partition function of an activated surface-bound complex to the product of the partition functions of the molecular fragments. In this case the desorption process has two steps: combination of molecular fragment adsorbates followed by desorption. The combination step is assumed to be rate-limiting and the frequency factor tends to be dependent on temperature and concentration.[5] Second order processes will not be considered in great detail and thus the reaction order n and the coverage and temperature dependence of ν will be dropped from the notation.

2.4 Parametric Dependence of TPD Signals

The following sections will examine hypothetical TPD signals. While TPD may be used to measure the frequency factor ν for a system with a known activation energy E_a, it is much more frequently used to measure the activation energy for known or estimated ν.

We will focus on this later application. The activation energy of desorption is equal to the enthalpy of adsorption for non-activated physical adsorption processes and provides an upper bound for the enthalpy of adsorption for activated processes such as dissociative adsorption. The base example will be a first order desorption process with parameters given in Table 1. This system was simulated using MATLAB's ode15s stepwise implicit ordinary differential equation solver over a temperature range from 120 K to 220 K with a ramp rate of 0.25 K/s. The initial surface coverage was assumed to be 10^{15} molecules/cm^2.

The simulated surface concentration and signal plots are show in figures 2.3 (a) and (b) respectively. The coverage decreases in time and the decay rate increases exponentially with the desorption rate. The inflection point of the surface coverage corresponds to the signal peak position at 182.6 K. The desorption rate intersects the coverage function at 186.8 K, which is the inflection point of the decreasing section of the TPD signal curve.

Table 2.1 Kinetic Parameters of Simple First Order Example

Parameter Name	Value
E_a	$50\ kJ/mol$
ν	$10^{13} Hz$

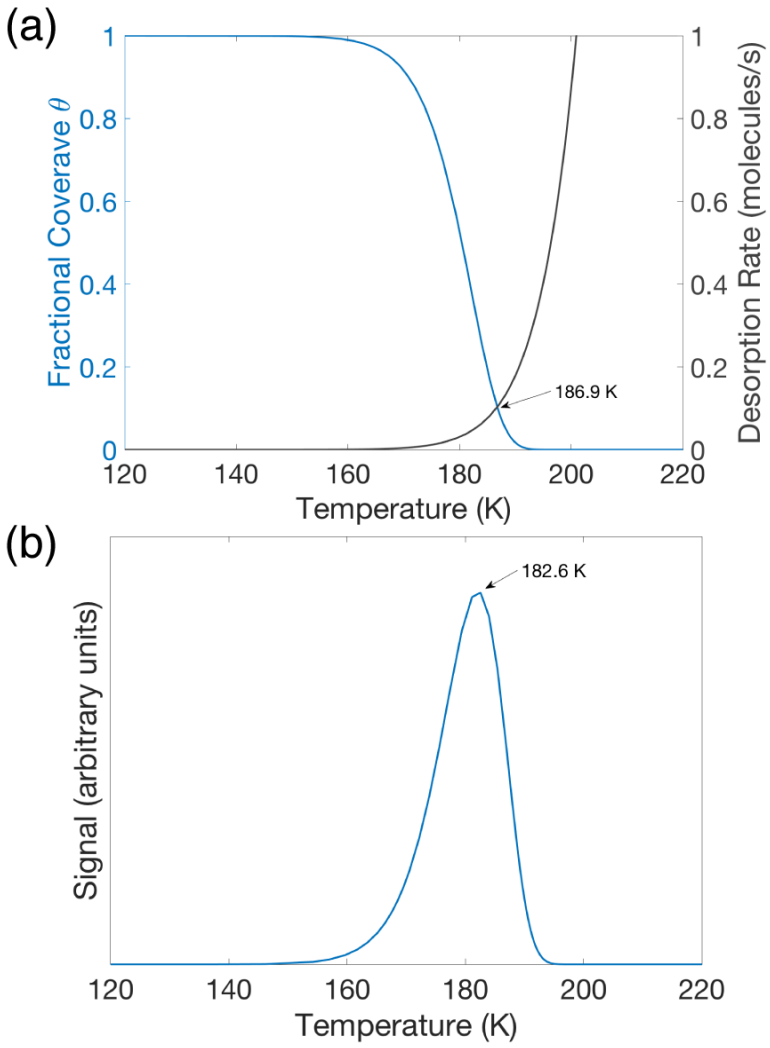

Figure 2.3 Overlay of simulated surface coverage decay and desorption rate (a) and TPD signal from single-site surface (b).

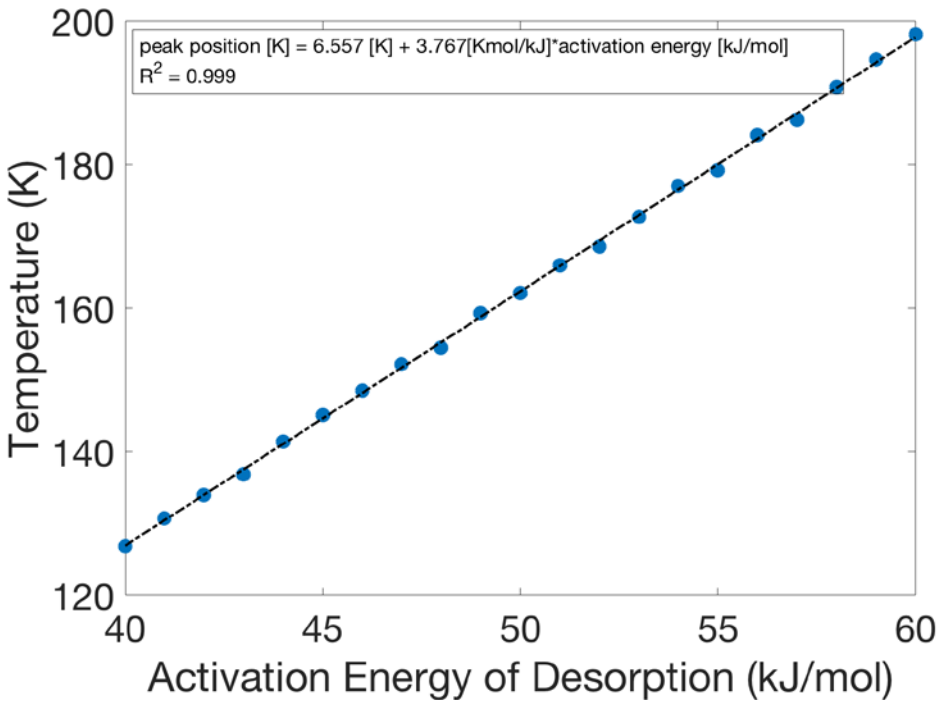

Figure 2.4 Single-site first order desorption peak position as a function of activation energy for fixed frequency factor and initial coverage. The blue dots represent simulated peak maxima while the hashed line is the linear regression curve.

The peak position for a fixed frequency factor varies linearly as a function of the activation energy. Figure 2.4 shows the results of a collection of simulations of single site surfaces over varied activation energies with fixed frequency $\nu = 10^{13}$ Hz and initial fractional coverage $\theta_0 = 1$. The relationship between the peak position and the activation energy of desorption is perfectly linear. Therefore, in the case of a single-site crystalline sample with a single, well-resolved peak, the activation energy of desorption can be extracted trivially using the relationship above. Unfortunately, most real samples are not as simple as this basic case. Even single crystal samples may contain a collection of different face terminations, edge sites, and surface defects to which gas molecules bind with varying energetics.

Consider another hypothetical crystalline sample, this time with four distinct adsorption sites. The relative concentrations of these sites can produce dramatically different TPD signals. Four site distributions, given in Table 2.2, were used to simulate the signals shown in Figure 2.5.

Table 2.2 Distributions of activation energies for a four-site sample

		Relative Site Concentration			
E_a (kJ/mol)	**ν (Hz)**	**Uniform**	**Increasing**	**Decreasing**	**Central**
50	10^{13}	25%	10%	40%	10%
53	10^{13}	25%	20%	30%	40%
56	10^{13}	25%	30%	20%	40%
59	10^{13}	25%	40%	10%	10%

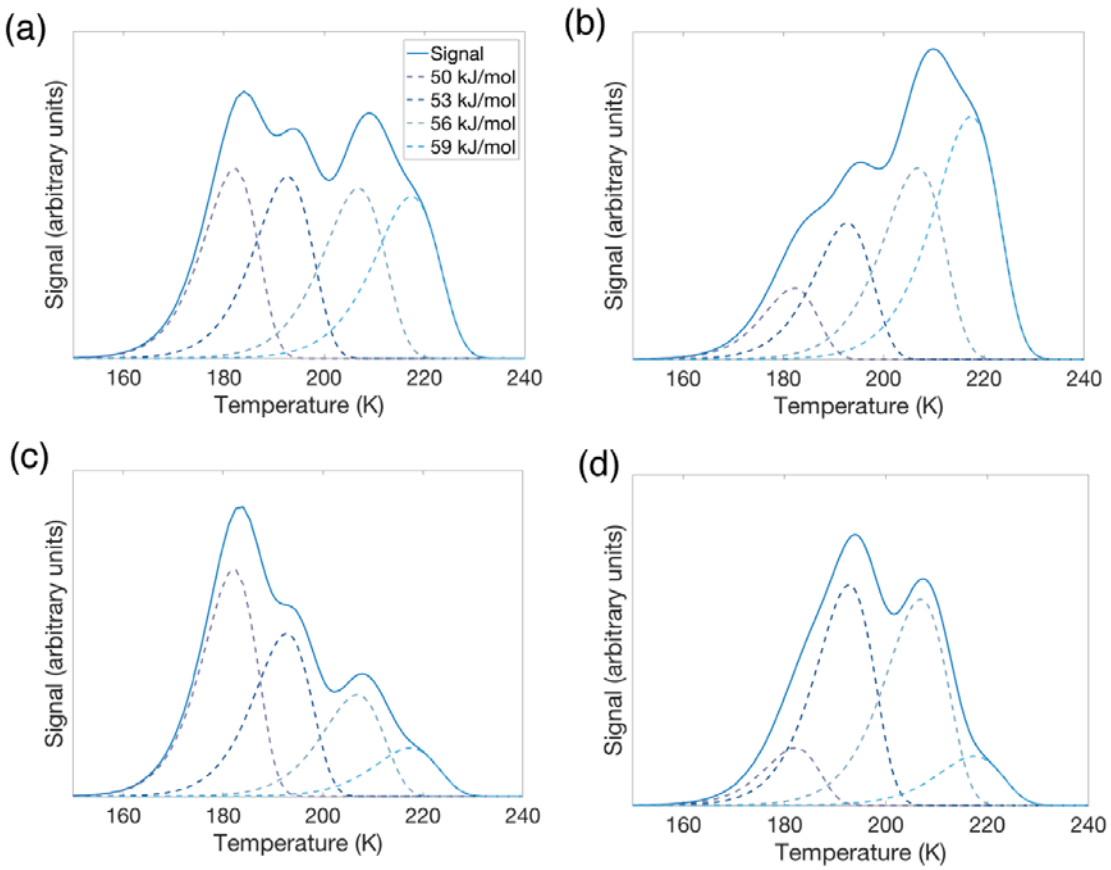

Figure 2.5 Simulated TPD profiles of uniform (a), increasing (b), decreasing (c), and central (d) site distributions. Contributions from each site are represented as dotted lines. The signal measured by a mass spectrometer is shown by a solid blue line.

The presence of multiple sites with similar adsorption bond energies results in overlapping peaks in the TPD signal. This causes distortions of the positions of peaks that are large enough to resolve and completely obscures those of smaller peaks. The asymmetry of the desorption signal results in dramatically different signals from inverted site distributions. Thus, it becomes impossible to resort to the linear model shown in Figure 4. Nevertheless, assuming the frequency factor can be measured accurately, it will be shown that these curves can be decomposed by nonlinear fitting techniques.

Recall that for a first order desorption process, the frequency factor ν is interpreted as the vibrational frequency of the bond between the adsorbate and the surface. While this value can be calculated via computational methods, it is often roughly approximated using the vibrational frequency of a comparable intermolecular attraction. For example, hydrogen bond vibrational frequencies are typically about 10^{13} Hz. This approximation will be used liberally throughout the development of numerical methods for quantitative analysis of TPD curves. In order to characterize the impact of approximation error on extracted desorption activation enthalpies, signals were simulated for a range of frequency factors with constant activation energy. Plots of these simulations are shown in Figure 2.6. The error in extracted activation energy can be determined by computing predicted energy from the linear model inset in Figure 4. This model is expressed as a function of the peak position $T(s_{max})$ in equation (2.6).

$$E_a = \left(0.265 \frac{kJ}{mol \cdot K}\right) T(s_{max}) - 1.741\ K \tag{2.6}$$

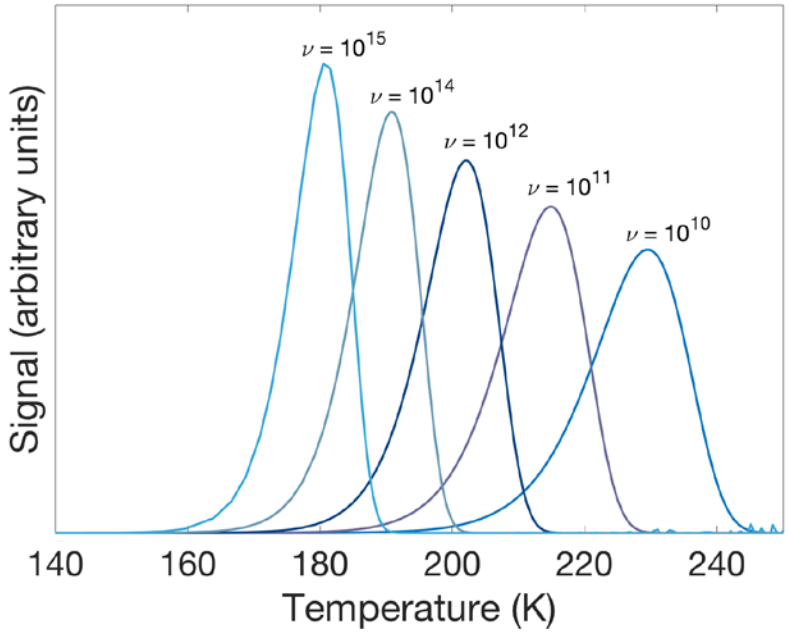

Figure 2.6. Desorption profiles for varied frequency factors at fixed activation energy $E_a = 50kj/mol$.

Table 2.3. Relative error in extracted activation energy associated with approximation error

Actual ν (Hz)	Approximate ν (Hz)	Peak Position (T)	Predicted E_a (kJ/mol)	Relative Error
10^{11}	10^{13}	229.3	59.0	18%
10^{12}	10^{13}	214.9	55.2	10.4%
10^{13}	10^{13}	202.3	50.0	0%
10^{14}	10^{13}	190.9	48.8	-2.3%
10^{15}	10^{13}	180.9	46.2	-7.6%

Table 2.3 shows the extracted activation energies and associated relative error for each magnitude of approximation error. Relative error is computed as the ratio of the extracted activation energy to the actual activation energy, which in this case is 50 kJ/mol. The predicted activation energy is insensitive to error in the frequency factor over the examined temperature range. Given the exponential form of the Polanyi-Wigner equation, this insensitivity of the signal shape to logarithmic variation in the frequency factor is perhaps not surprising. Nevertheless, it's worth demonstrating that the method is notably robust to error in the estimate of ν. Interestingly, the error in extracted activation energy is much lower if the frequency factor is overestimated than if it underestimated by the same magnitude. This property is the result of the dramatic asymmetry in the temperature dependence of equation (2.2). Hydrogen bond frequencies tend to range between 5.0×10^{12} and 1.0×10^{13}. Given the above results, we can confidently approximate $\nu \approx 10^{13}$ for water desorption from polar surfaces and expect less than 1% resulting error in the predicted desorption activation enthalpies.

All simulations discussed up to this point were performed with a constant ramp rate α. It is important to note that because the ramp rate impacts the exponential term of equation (2.2), that it can have significant impacts on the signal intensity. Figure 2.7 shows single-site simulations with kinetic parameters found in Table 2.1 with varied ramp rates. This property of desorption process is useful in that it allows the experimental parameters to be tuned to the sensitivity of the sensor and the surface area of the sample. For example, if the sample is very small, the ramp rate could be set very high to yield a large signal. Alternatively, if the surface area is very large, such as in the case of a porous film, the ramp rate could be set very low to avoid overloading the pump or the sensor.

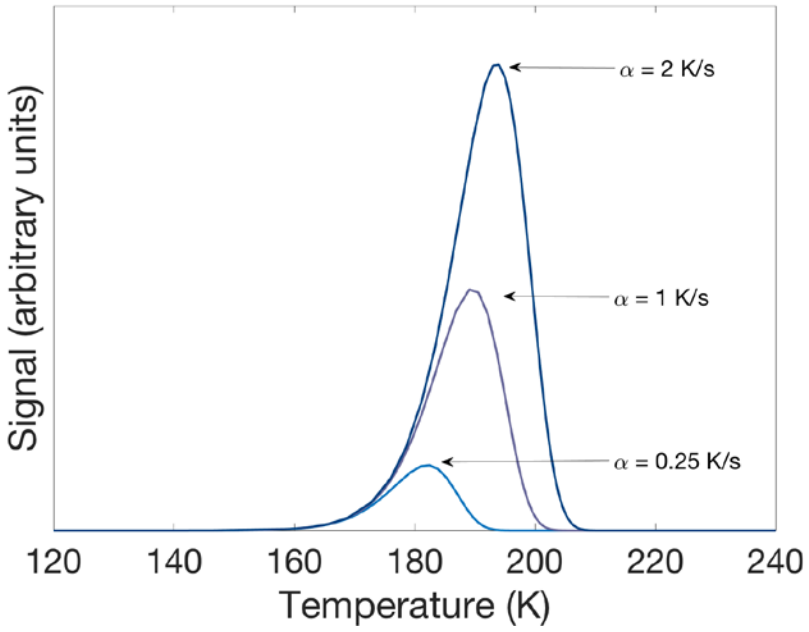

Figure 2.7. Desorption profiles at various ramp rates.

2.5 Continuous Site Distributions

The occasion often arises in modern surface characterization that part or all of the sample is amorphous. In such cases it is unreasonable to assume that a small set of distinguishable sites are exposed. These surfaces can be modeled with a continuous site distribution. We will constrain our analysis of continuous site distributions to gaussian and skewed gaussian probability density functions. The univariate Gaussian Normal probability density function $\phi(x;\ \mu, \sigma^2)$ and cumulative density function $\Phi(x;\ \mu, \sigma^2)$ are shown in equations (2.7) and (2.8) respectively. Equations (2.9) gives an alternative expression of the Gaussian Normal cumulative density function.

$$\phi(x;\mu,\sigma^2) = \frac{1}{\sqrt{2\pi\sigma^2}} e^{\frac{(x-\mu)^2}{2\sigma^2}} \tag{2.7}$$

$$\Phi(x;\ \mu,\sigma^2) = \frac{1}{\sqrt{2\pi}}\int_{-\infty}^{\frac{x-\mu}{\sigma}} e^{-t^2}dt \tag{2.8}$$

$$= \frac{1}{2}\left(1 + \text{erf}\left(\frac{x-\mu}{\sigma\sqrt{2}}\right)\right) \tag{2.9}$$

The terms μ and σ^2 are the usual location and shape parameters that determine the mean and variance of the distribution respectively. The error function of a scalar x is denoted by $\text{erf}(x)$. Asymmetric continuous distributions will be modeled using the skew normal distribution in equation (2.10).

$$f(x;\mu,\sigma^2,a) = 2\phi(x;\mu,\sigma^2)\Phi(bx;\mu,\sigma^2) \tag{2.10}$$

We begin by considering a Gaussian site distribution with mean $\mu = 50\,\frac{kJ}{mol}$ and considering three separate variances: $\sigma_1^2 = 1\ (kJ/mol)^2$, $\sigma_2^2 = 4\ (kJ/mol)^2$, and $\sigma_3^2 = 9\ (kJ/mol)^2$. The distributions of these site energies are shown in Figure 2.8.

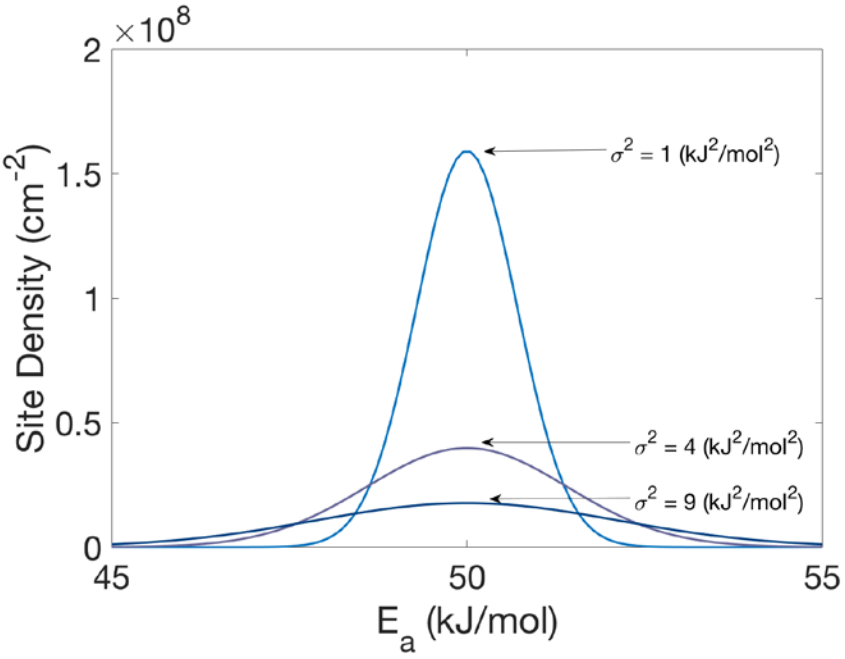

Figure 2.8 Gaussian distributions of site energies.

The distributions were simulated with 100 discrete sites each. The results of these simulations are shown in Figure 2.9. Contributions from each site are shown in the left column while the aggregate desorption rate is given on the right. The desorption peak broadens with larger variance in the activation energy and the maximum intensity decreases. The desorption peak position does not change with variance in the site distribution. These results indicate that TPD might be very useful for characterizing heterogeneous or amorphous surfaces using the mean and standard deviation as the fitting parameters.

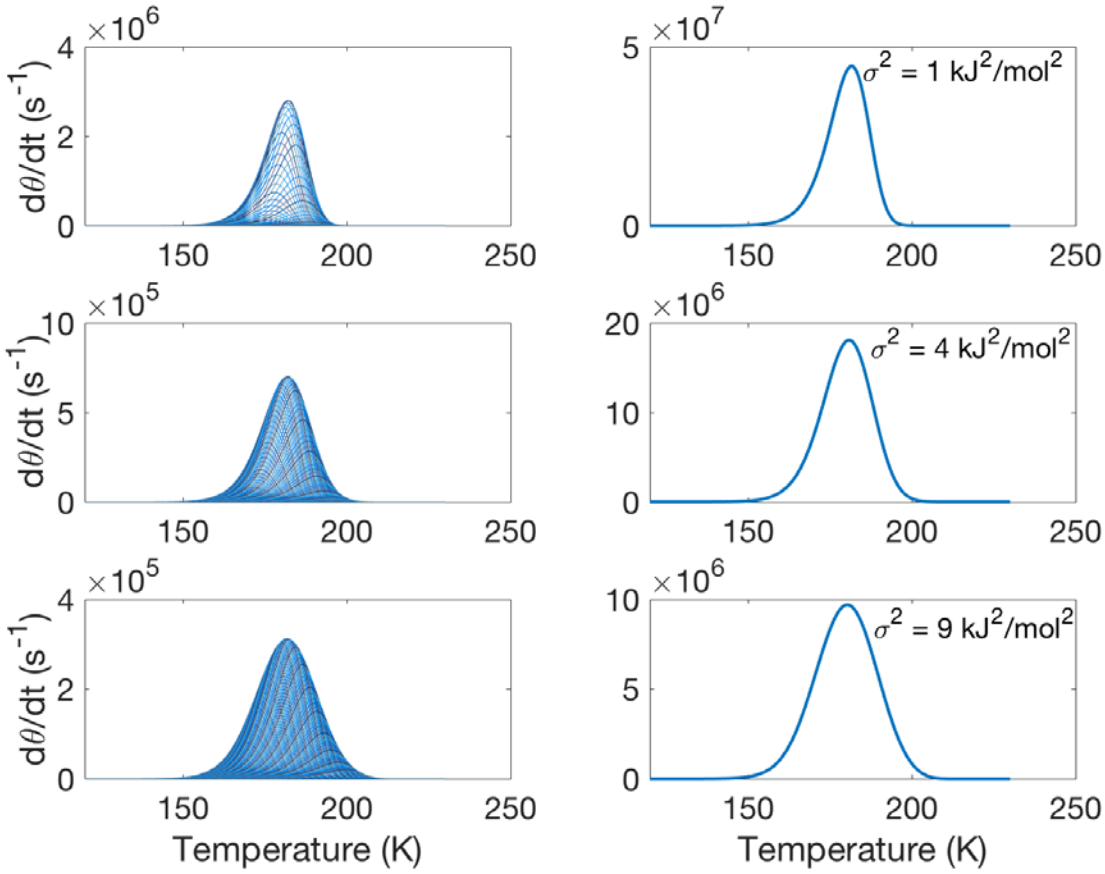

Figure 2.9 Desorption profiles of Gaussian site distributions of increasing variance. The contribution from each site is given on the left and the total desorption rate is given on the right. The variance of each row is inset in the plot of the aggregate desorption rate on the right.

Finally, consider a heterogeneous surface with a continuous distribution of desorption activation energies and a high concentration of surface defects that tend to bind adsorbates more strongly. This distribution will be modeled using the skewed Gaussian density function in given in equation (2.10) with skew parameters $b_1 = 0$, $b_2 = 8$, $b_3 = 12$. The mean will again be $\mu = 50\frac{kJ}{mol}$ and the variance $\sigma^2 = 4\ \left(\frac{kJ}{mol}\right)^2$. Figure 10 shows the site distribution and aggregate signals for each variance. Note that the signal is only moderately sensitive to the skew parameter but that, unlike the variance, it does impact the peak position. The skew position could thus also be considered as a fit parameter. However, because both the skew and the mean both impact the peak position, prior knowledge of one would be necessary to extract the other. For example, if the mean desorption activation energy for a given material surface were known, fitting the skew parameter of the distribution could then be used as a measure of the surface defect site density.

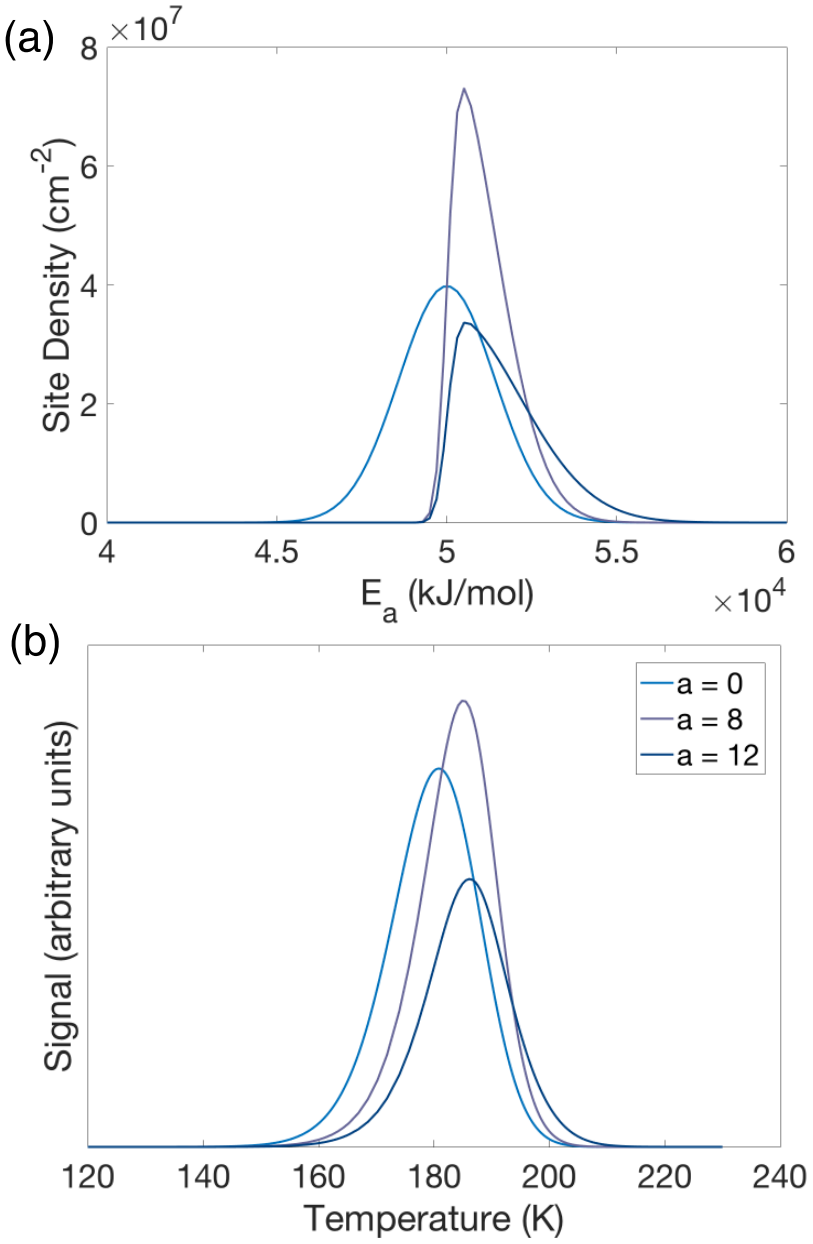

Figure 2.10 Skewed site distributions (a) and associated desorption profiles (b).

2.6 Conclusions

The relationship between the first order temperature programmed desorption signal and the underlying distribution of surface sites on a given sample can be defined for a wide range of surface classes. While existing methods for quantitative analysis of desorption curves focus on simple site distributions, models for complex site distributions show that naïve analysis can result in incorrect predictions of underlying thermodynamic properties of surface-adsorbate bonds due to signal distortions induced by parallel desorption processes. Desorption processes from distinct sites contribute topographical features to the TPD signal, even if the site concentration is too low to resolve a full peak. The asymmetry of the TPD process causes similar distributions to result in dramatically different peak shapes. This property will be used in the next chapter, where a nonlinear least squares fitting approach is developed.

2.7 References

1. Kasrai, M.; Lennard, W. N.; Brunner, R. W.; Bancroft, G. M.; Bardwell, J. A.; Tan, K. H., Sampling Depth of Total Electron and Fluorescence Measurements in Si L- and K-Edge Absorption Spectroscopy. *Appl. Surf. Sci.* **1996**, *99*, 303-312.
2. Poston, M. J.; Grieves, G. A.; Aleksandrov, A. B.; Hibbitts, C. A.; Darby Dyar, M.; Orlando, T. M., Water Interactions with Micronized Lunar Surrogates JSC-1A and Albite under Ultra-High Vacuum with Application to Lunar Observations. *J. Geophys. Res. E* **2013**, *118*, 105-115.
3. King, D. A., Thermal Desorption from Metal Surfaces: A Review. *Surf. Sci.* **1974**, *47*, 384-402.
4. Barrie, P. J., Analysis of Temperature Programmed Desorption (Tpd) Data for the Characterisation of Catalysts Containing a Distribution of Adsorption Sites. *Phys. Chem. Chem. Phys.* **2008**, *10*, 1688-1696.
5. Vannice, A. M., *Kinetics of Catalytic Reactions*; Springer: New York, 2005.

6. Jong, A. M. d.; Niemantsverdriet, J. W., Thermal Desorption Analysis: Comparative Test of Ten Commonly Applied Procedures. *Surf. Sci.* **1990**, *233*, 355-365.
7. Datta, S. J., et al., CO_2 Capture from Humid Flue Gases and Humid Atmosphere Using a Microporous Coppersilicate. *Science* **2015**, *350*, 302-306.
8. Han, G. B.; Park, N.-K.; Yoon, S. H.; Lee, T. J.; Han, G. Y., Direct Reduction of Sulfur Dioxide to Elemental Sulfur with Hydrogen over Sn−Zr-Based Catalysts. *Ind. Eng. Chem. Res.* **2008**, *47*, 4658-4664.
9. Malte, B., Heterogeneous Catalysis of CO_2 Conversion to Methanol on Copper Surfaces. *Angewandte Chemie International Edition* **2014**, *53*, 12022-12024.
10. Shao, M.; Peles, A.; Shoemaker, K., Electrocatalysis on Platinum Nanoparticles: Particle Size Effect on Oxygen Reduction Reaction Activity. *Nano Letters* **2011**, *11*, 3714-3719.

CHAPTER 3. NONLINEAR REGRESSION OF NUMERICALLY INTEGRATED FUNCTIONS

3.1 Nonlinear Regression for Surface Analysis

Nonlinear least squares regression is widely used in surface chemical analysis in the context of X-ray photoelectron spectroscopy (XPS). XPS peaks are convolutions of Gaussian and Lorentzian line shapes and the process of fitting them is therefore referred to as *deconvolution*.[1] This involves proposing an initial guess for the distribution chemical states of a given element on the surface of a material and then updating this guess by minimizing the sum of squared residuals between the guess and the data. Given the nonlinear form of the function, the minimum has no closed form solution and iterative algorithms are used. Typically, these algorithms are run under some specified set of constraints in order to encode the analyst's external knowledge of the system. Complex surfaces with wide distributions of chemical states can be expected to produce broad XPS signals with varying degrees of structure from which the underlying chemistry can be inferred. Each Gaussian peak profile includes at least three parameters and the risk for overfitting the signal is high.

Where XPS peaks are convoluted, overlapping TPD signals are decomposed, since the measured signal is simply the sum of the curves from different energies. The process for decomposition of TPD signals parallels XPS deconvolution in many ways. A guess distribution is proposed by the analyst and refined using an iterative optimization algorithm to extract the most likely position and shape parameters for the component kinetic processes. Risk of overfitting is comparable. The highly nonlinear relationships between parameters can result in poor performance of basic line search optimization methods and the search domain must be bounded in order to the maintain numerical stability of the integrated signal function. The

nonlinear least-squares objective function is non-convex and suffers from the local optimum problem. Moreover, the global minimum may not be the best representation of the underlying surface chemistry. Various aspects of these problems are studied in subsequent chapters. Despite these issues, we will see that, given high quality data, the kinetic parameters of the underlying surface can be extracted with high accuracy and the underlying surface chemistry can therefore be studied effectively. When this information is combined with techniques such as XPS and vibrational spectra, a detailed picture of the surface chemistry can be constructed.

3.2. Maximum Likelihood Estimation

Least squares regression is a natural result of elementary probability theory. This derivation will be reviewed here before proceeding to problem-specific numerical considerations. Consider a deterministic model $f(\boldsymbol{x}, \boldsymbol{\omega})$ of a data vector $\boldsymbol{y} = (y_1\ y_2\ \dots\ y_n)^T$ with a stochastic error term ϵ such that

$$y_i = f(\boldsymbol{x}_i, \boldsymbol{\omega}) + \epsilon_i. \tag{3.1}$$

We let $\boldsymbol{x}$ denote a vector of the predictor variables and $\boldsymbol{\omega}$ is the vector of model parameters. If the error term ϵ is normally distributed, then we can write the probability density p of the target variable y_i given the model parameters as

$$p(y_i; \boldsymbol{\omega}) = N(y_i; f(\boldsymbol{x}, \boldsymbol{\omega}), \sigma^2) \tag{3.2}$$

$$= \frac{1}{\sqrt{2\pi\sigma^2}} e^{-\frac{(y_i - f(\boldsymbol{x}, \boldsymbol{\omega}))^2}{2\sigma^2}}. \tag{3.3}$$

If we assume that data vector $\boldsymbol{y}$ consists of independent and identically distributed samples from $p(y; \boldsymbol{\omega})$, the joint density function over the data is the product of the density functions of each sample.

$$p\left(\{y_{1,}y_2,\dots,y_n\};\boldsymbol{\omega}\right)=\prod_{i=1}^{n}\frac{1}{\sqrt{2\pi\sigma^2}}e^{-\frac{(y_i-f(\boldsymbol{x}_i,\boldsymbol{\omega}))^2}{2\sigma^2}} \tag{3.4}$$

When considered as a function the parameter vector $\boldsymbol{\omega}$, equation 4 is called the likelihood function and the parameter vector $\boldsymbol{\omega}$* that corresponds to the highest probability of the data vector $\boldsymbol{y}$ is the maximum likelihood estimate. As a product over a potentially large number of probabilities that are by definition between 0 and 1, the direct computation of the likelihood function carries a high risk of numerical underflow. It is often convenient to use the log-likelihood function given in equation (5). The logarithmic function is monotonically increasing and therefore preserves the optimality conditions of the likelihood function.

$$\ln p\left(\{y_{1,}y_2,\dots,y_n\};\boldsymbol{\omega}\right)=\ln\prod_{i=1}^{n}\frac{1}{\sqrt{2\pi\sigma^2}}e^{-\frac{(y_i-f(\boldsymbol{x}_i,\boldsymbol{\omega}))^2}{2\sigma^2}} \tag{5}$$

$$=-\frac{n}{2}(\ln 2\pi+\ln\sigma^2)-\frac{1}{2\sigma^2}\sum_{i=1}^{n}\left(y_i-f(\boldsymbol{x}_i,\boldsymbol{\omega})\right)^2 \tag{6}$$

Under the assumption that the variance σ^2 is constant, then the log-likelihood function is maximized by minimizing the sum of squared residuals $\sum_{i=1}^{n}\left(y_i-f(\boldsymbol{x}_i,\boldsymbol{\omega})\right)^2$. This is the least squares criterion. Probabilistic models introduced in chapter 5 will not assume constant variance of the data about the model line.

3.3 Numerical Considerations

Iterative least squares optimization requires a potentially large number of evaluations of the model function, which itself involves a numerical integration of the Polanyi-Wigner equation under dynamic temperature conditions. Naïve implementations that rely too heavily on commercially available ordinary differential equation (ODE) solvers tend to perform poorly

because these programs are optimized for fundamentally different problem constraints. Codes such as those found in MATLAB's ODE library use complicated adaptive step calculations which are crucial to preserving accuracy when the state of the system at the next time step is unknown. However, given the monotonically decreasing behavior of the surface concentration throughout the TPD experiment, the dynamics of the state of the system can be roughly estimated before the integration is performed, and the step size can be fixed to ensure accuracy and stability while removing the large computational overhead associated with adaptive steppers.

The Polanyi-Wigner equation is an example of a stiff differential equation. While formal definitions of stiff differential equations vary, the term generally refers to equations in which the value of the state variable varies over many orders of magnitude over a short time period.[2] Such equations are problematic for adaptive integrators because these programs compute the size of each step using the dynamics of the steps preceding it. Applying this method to stiff ODEs can result in very long runtimes because temporal regions of large dynamic variation act to contract the step size to very short time intervals. These problems are typically solved using implicit ODE integration schemes, which are less accurate than explicit schemes such as the widely used Runge-Kutta 4-5 algorithm.[2]

There is also the problem of comparing a numerically integrated curve with a data set. In the case of an adaptive stepper, the support points of the integrated curve do not match those of the measured signal and the residuals must be calculated by interpolation. The interpolation step adds extra computational overhead to an otherwise costly procedure and the quality of the residual computation can be sensitive to the interpolation method applied. For example, cubic spline interpolations were found to perform much better than linear interpolation but come at additional computational cost. Both the interpolation and adaptive stepper problems can be

solved simultaneously by using the time steps in the dataset to define the integration steps. The time resolution of the time data is typically sufficient to provide a high accuracy integrated approximation if it is able to capture the dynamics of the desorption process during the measurement. If the density of measurements is not high enough to maintain numerical stability, the data set can be interpolated once as a preprocessing step. Linear interpolation procedures were found to perform as well as more advanced interpolations, such as cubic splines.

3.4 Platinum Nanoparticle Test Case

We conclude this chapter with an example of a nonlinear least squares fit of a simulated TPD curve. The oxygen reduction reaction is an important reaction in electrochemical processes. The reaction proceeds very slowly and presents a hard limit to the implementation of fuel cell technologies.[3] Consider a fuel cell with a graphite supported platinum nanoparticle cathode. Suppose we wish to measure the enthalpy of adsorption of oxygen gas on the porous cathode. If the nanoparticles are 1.8 nm in diameter and have five distinct sites. These sites are illustrated in Figure 3.1 and the associated desorption enthalpies of oxygen gas are given in Table 1. The sites are labelled according to the convention used by Shao *et al*. Oxygen binds strongly to these sites due to its diradical electronic structure but does not dissociate upon adsorption.[4] Therefore, first order TPD is an appropriate method to probe both the adsorption enthalpy and the site distribution. The vibrational frequency of the platinum-oxygen bond is unknown, however oxygen-metal bond absorptions tend to be in the far-infrared region of the electromagnetic spectrum and we therefore take $10^{13} Hz$ to be an appropriate overestimate of the frequency factor. Figure 3.2 shows the simulated TPD signal for a ramp rate of 0.25 K/s.

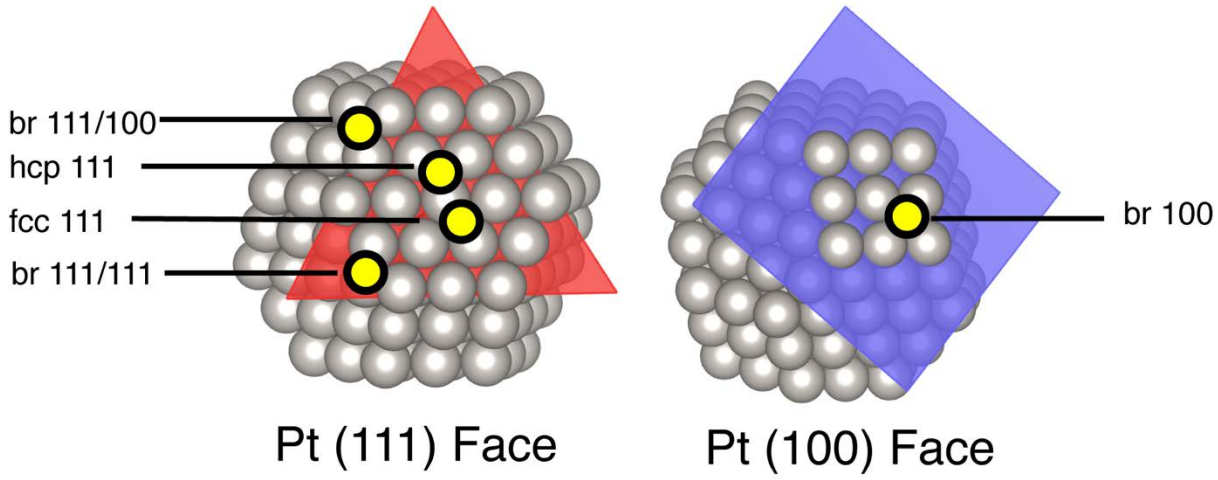

Figure 3.1 Adsorption Sites on 1.8 nm Pt nanoparticle faces.

Table 3.1 Enthalpy of adsorption of oxygen on Pt nanoparticle sites

Adsorption Site	Coordination Number	Adsorption bond enthalpy(kJ/mol)	Fraction of total sites
fcc 111	2	86.9	0.45
hcp 111	3	115.8	0.15
br 100	4	119.6	0.10
br 111/111	2	129.3	0.10
br 111/100	2	154.4	0.20

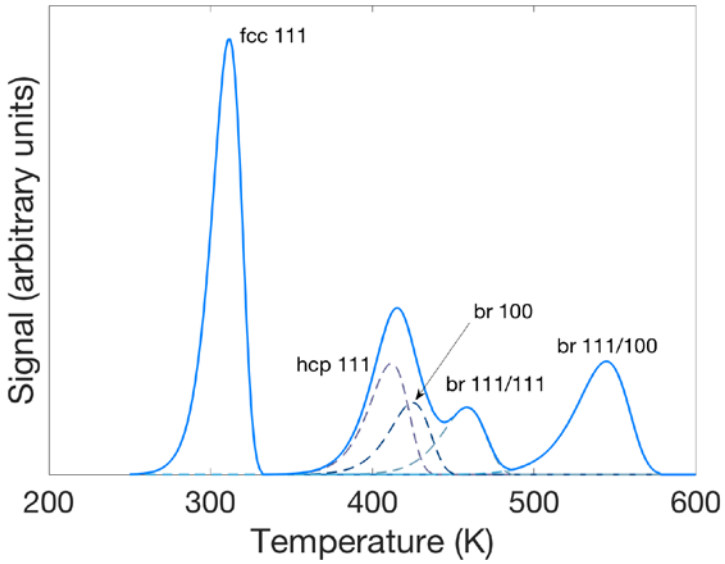

Figure 3.2 Simulated desorption profile of oxygen from 1.8 nm Pt nanoparticles.

Given the knowledge that there are 5 distinct adsorption sites, the least squares fitting procedure returns a very accurate decomposition of the signal. Figure 3.3 shows plots of the initial guess and the refined fit of the simulated oxygen desorption data. The initial guess included activation energies that were picked to center the peaks and a uniform distribution of relative site coverages ($\theta_0 = 0.2$ for each curve). The extracted activation energies of desorption are given in Table 3.2. Recall that for a first order process these values are equal to the enthalpy of adsorption.

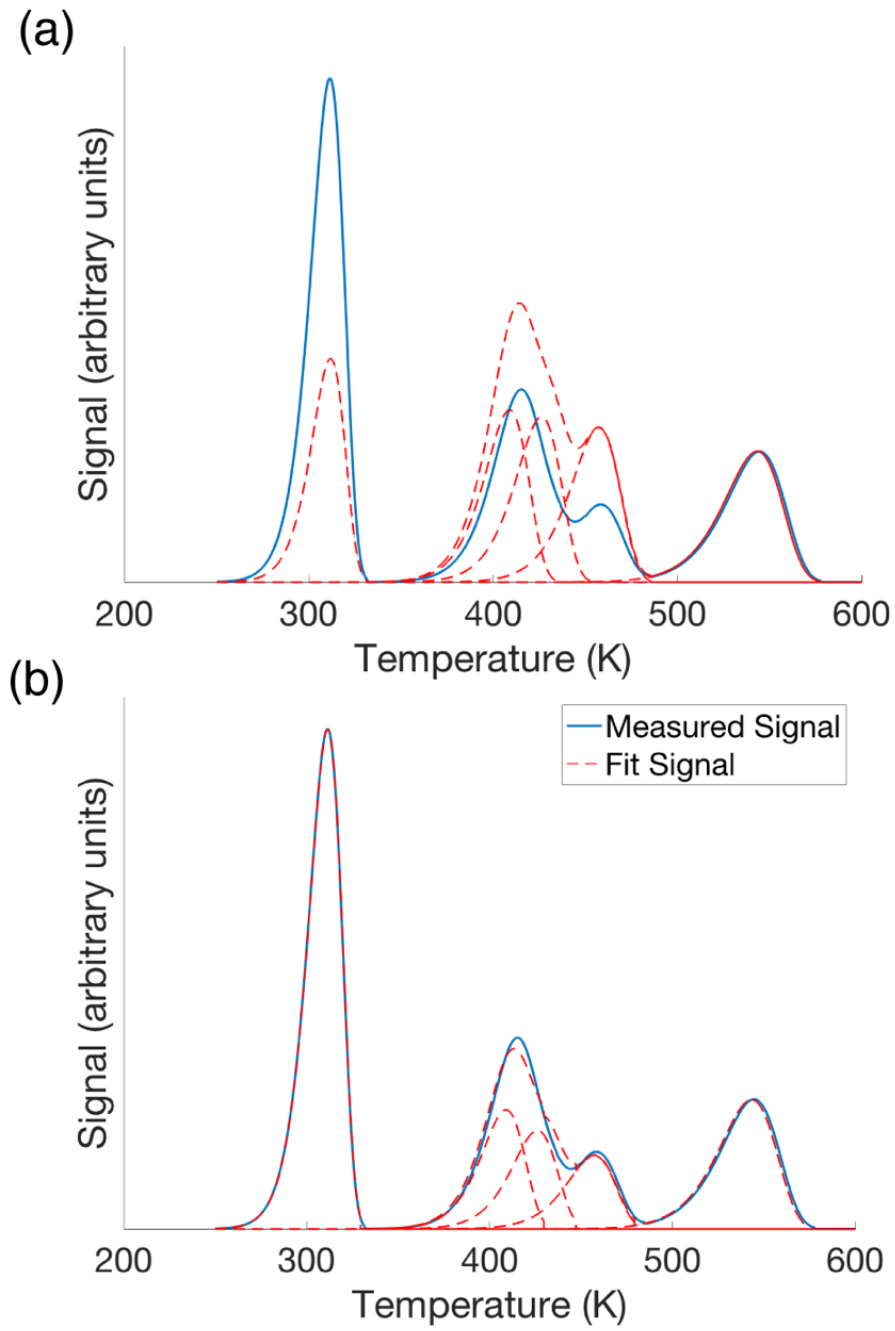

Figure 3.3 Initial guess signal (a) and refined signal (b) after least squares fit procedure.

Table 3.2 Comparison of fit parameters with actual values

Peak Position	Parameter	Value	Relative Error
310.8 K	E_a	87.0 kJ/mol	0.1%
	θ_0	0.448	-0.4%
408.1 K	E_a	115.0 kJ/mol	-0.7%
	θ_0	0.14	-6.6%
426.0 K	E_a	120.0 kJ/mol	0.3%
	θ_0	0.12	20%
458.5 K	E_a	129.0 kJ/mol	-0.2%
	θ_0	0.095	5%
542.1 K	E_a	154.0 kJ/mol	-0.3%
	θ_0	0.19	5.3%

The nonlinear least squares algorithm performs very well in fitting the activation energy parameter and reasonably effectively with the coverage parameter. The average absolute relative error in the predicted activation energy was 0.32% while the average relative error magnitude in the predicted coverage parameter was 7.4%. The average magnitude of the relative error of the coverage parameter was brought down by the non-overlapping peaks, which lead to less ambiguity in the underlying distribution than the overlapping peaks.

This technique is clearly very effective; however, the results don't give any indication of the uncertainty in the parameter estimates. In later chapters, probabilistic models will be incorporated to build a more complete picture of the fit quality.

3.5 References

1. Wagner, C. D.; Riggs, W. M.; Davis, L. E.; Moulder, J. F.; Mullenberg, G. E., *Handbook of X-Ray Photoelectron Spectroscopy*; Perkin-Elmer Corporation: Eden Prairie, Minnesota, 1979.
2. Beers, K. J., *Numerical Methods for Chemical Engineering: Applications in Matlab*; Cambridge University Press: Cambridge, 2006.
3. Ferrizz, R. M.; Gorte, R. J.; Vohs, J. M., TPD and XPS Investigation of the Interaction of SO_2 with Model Ceria Catalysts. *Catalysis Letters* **2002**, *82*, 123-129.
4. Shao, M.; Peles, A.; Shoemaker, K., Electrocatalysis on Platinum Nanoparticles: Particle Size Effect on Oxygen Reduction Reaction Activity. *Nano Letters* **2011**, *11*, 3714-3719.

CHAPTER 4. INTERACTIONS ON EXTERNAL MOF SURFACES: DESORPTION OF WATER AND ETHANOL FROM CUBDC NANOSHEETS

4.1 Introduction

This chapter was published in *Langmuir* in September 2017.[1] It is reproduced here with permission from the journal. There has been a rapid growth in research efforts directed towards understanding the structural and chemical properties metal-organic framework (MOF) materials in recent years. MOFs are composed of metal ions bound by linker ligands into reticular crystal lattices. [2] These materials have high surface areas, chemical modularity, and in some cases, mechanical functionality.[3-5] Potential applications that follow naturally from these properties include catalysis, chemical sensing, and gas adsorption.[6-8] MOFs have also been proposed for inclusion as the active components of separations membranes.[7, 9-10]

MOF nanosheets are crystals with thicknesses on nanometer length scales and typically with pore structures that run roughly normal to the plane of the sheet. They have recently gained attention because of their high stacking efficiency, which allows development of thinner, more tunable membranes.[7-8, 11-12] They have been synthesized by a number of methods, including top-down exfoliation of layered crystals as well as bottom-up approaches that make use of modulating ligands or diffusion-mediated processes.[11-16] The external surfaces of MOF crystals have not been well studied, though they play an important role as gateways to the bulk pore structure.[17] MOF nanosheets are uniquely suited for studying the chemistry at external MOF surfaces because a single crystallographic face comprises a significant portion of the total surface area. As will be shown, outer adsorption sites interact more strongly with some guest molecules than internal sites. The implications of this result are that sorption properties of MOF particles

depend on their morphology and that degradation models, such as that of ligand displacement by water, may need to account for kinetic variation at the surface.[18-21]

We motivate our choice of adsorbate gases in the context of the rising need for alternative fuel sources, such as bioethanol, in the face of global climate change.[22] Separation of water and ethanol is an important step in the production of biofuels and accomplishing this process by membrane separation can be more energy-efficient than distillation.[23-24] However, water and ethanol interact strongly and the challenge in designing a suitable membrane lies in finding a material that selectively binds one over the other.[25] Carboxylate-based MOFs tend to have a high affinity for water and therefore various topologies have been proposed or demonstrated for application as the active component of ethanol-water separations membranes.[9, 19, 26-27]

In this paper, we explore the differences between interaction of water and ethanol at interior and external adsorption sites by a combination of Fourier transform infrared (FT-IR) spectroscopy, powder X-ray diffraction (PXRD) and temperature programmed desorption (TPD) from copper benzenedicarboxylate (CuBDC) nanosheets. The goal is to extract the kinetic parameters of desorption from external surface and internal pore sites. Complications due to diffusion arise in the analysis of the desorption signal from porous materials.[17-18] Numerical methods have been demonstrated to be effective in assisting the analysis of complicated surface phenomena.[28] Herein we develop a numerical approach for the quantitative analysis of TPD from porous media that deviates from previously applied approaches by attributing peak broadening primarily as diffusion rather than as contributions from defect sites.[29] The diffusion coefficients of water and ethanol are also extracted from the TPD data, demonstrating versatility in the method.

4.2 Experimental Methods

CuBDC Synthesis: CuBDC nanosheets were synthesized using a scaled-up version of the layered synthesis reported by Rodenas *et al*.[12] In a high aspect ratio beaker, measuring 1.4 cm in radius and 10 cm in height, 300 mg of terephthalic acid were dissolved into a mixture of 20 mL dimethylformamide (DMF) and 10 mL of acetonitrile to form the linker layer. A spacer layer was made by mixing 10 mL acetonitrile and 10 mL DMF. The spacer layer was then poured over the linker layer slowly to avoid mixing. The metal layer was made by mixing 300 mg $Cu(NO_3)_2 \cdot 3H_2O$ in 20 mL acetonitrile and 10 mL DMF then poured slowly over the spacer layer. The system was allowed to react for 24 hours at room temperature, after which the precipitate was recovered by centrifugation at 500 rpm for 25 minutes and washed three times with 10 mL acetonitrile. 3-6 hours were allowed for solvent exchange between washes to facilitate a more gentle activation process at 150 ˚C, which is lower than previously reported.[12, 30] This was done to minimize thermal degradation of the surface. The resulting 7 mg of light blue crystalline MOF powder was suspended in acetonitrile for storage. This corresponds to a 2.3% yield by mass.

Nanosheet Characterization: Particle shape was confirmed using a Hitachi SU8230 Field Emission Scanning Electron Microscope (SEM) with a landing potential of 1000 V. The SEM sample was prepared by drop-coating the particle suspension on a piece of highly oriented pyrolytic graphite (HOPG). A Veeco Dimension Atomic Force Microscope (AFM) was used to measure the thickness of the nanosheets that had been similarly drop cast onto an atomically flat piece of cleaved HOPG. The crystal structure was confirmed by drop-coating on an amorphous silicon sample holder and recording the PXRD pattern using a Panalytical X'pert Pro Powder X-ray diffractometer. Brunauer–Emmett–Teller (BET) surface area was measured using a Micrometrics Flowsorb III. Transmission FT-IR spectroscopy was performed on a Bruker Vertex 70 spectrometer using KBr pellets. Raman spectroscopy was performed using a Bruker Senterra

Raman microscope with 0.2 mW (532 nm) laser power integrated over 60 seconds to avoid local heating and damage to the sample.

Temperature Programmed Desorption: Experiments were carried out in an ultrahigh vacuum (UHV) chamber with base pressure $\sim 10^{-10}$ Torr. This system has been described in detail previously.[31] Relative pressure of gas inside the chamber was measured with a Pfeiffer PrismaPlus residual gas analyzer quadrupole mass spectrometer. CuBDC nanosheets were deposited on a gold-coated oxygen-free high conductivity copper sample holder by repeated drop-coating from the acetonitrile suspension. The sample film was 1 mm thick and covered the 3.9 cm^2 sample bed. MOF activation was carried out by heating the sample at 150˚ C for 24 hours. Vapor doses were applied by cooling the sample to 180 K and maintaining 10^{-7} Torr of the desired gas for 40, 160, 640, or 1600 seconds corresponding to 4, 16, 64, or 160 L exposures. After dosing, the sample was cooled to 120 K and the chamber pressure was allowed to equilibrate. TPD experiments were carried out with a ramp rate of 0.25 K/s, heating the sample from 120 K to 400 K. Three trials were conducted for each measurement to test reproducibility. The sample stage was mechanically detached from the high-surface area cooling system during heating to minimize the background signal, which was measured by exposing the system to the same dosing and ramp procedure as the sample. Background subtraction was conducted by linear interpolation of the TPD traces.

Co-adsorption measurements were conducted by dosing the chamber sequentially with 4 L of pure water and pure ethanol each at 180 K, followed by cooling to 120 K and heating to 400 K at 0.25 K/s. This was also repeated in reverse order with the water dose following ethanol.

Temperature Programmed Desorption Curve-Fit Simulation: MATLAB 2015 was used for all curve fitting and simulations. Temperature programmed desorption data was analyzed

quantitatively by integrating the boundary value problem in one dimension discussed below. The simulated film had a height of 1 mm, which corresponds to the bed depth in the TPD experiment. The film was discretized using the central difference approximation with a grain width of 100 μm. The discretized boundary value problem was integrated over 920 seconds using MATLAB's ode15s stiff ordinary differential equation solver. Nonlinear least squares regression was fit using MATLAB's genetic algorithm for constrained, stochastic optimization.

4.3 Results and Discussion

4.3.1 Characterization of CuBDC nanosheets

Figure 1 shows various measurements of the particle morphology. Most particles grow into well-defined squares of varying sizes visible in the SEM image in Figure 1(a). While there are a few large sheets, the majority are under 1 μm^2. The smaller sheets are more easily viewed in the AFM image in Figure 1(b). The histogram in Figure 1(c) shows that the distribution of sheet thicknesses and the average is approximately 9.4 nm. Given that there are 2.11 layers per nm of thickness, the sheets are roughly 20 layers thick on average and therefore 5% of copper adsorption sites are located on the external surface for fully activated samples. This is a significant portion of sites compared to a three-dimensional crystal. For example, in a 1 μm-thick crystal, just 0.09% of copper adsorption sites are located on the surface.

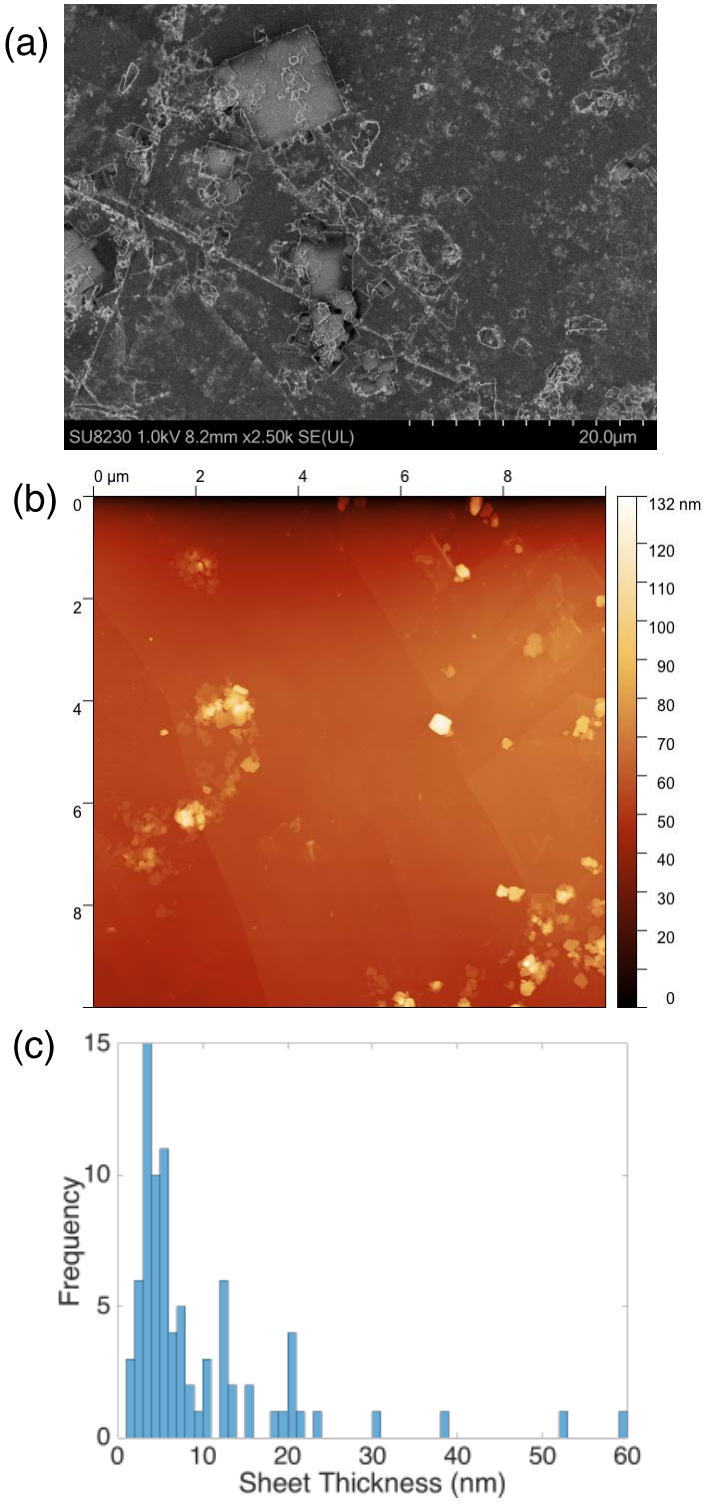

Figure 4.1 Morphology of CuBDC nanosheets: SEM (a) and AFM (b) images of particles on HOPG. Histogram of sheet thickness measured using AFM (c).

CuBDC grows rapidly inside the $(\bar{2}01)$ plane as coordinate bonds between Cu(II) and 1,4-benzenedicarboxylate (BDC) form the net-like structure of the individual lamina. It has been reported that MOF crystal growth follows a two-step process in which metal ions adsorb to the surface before migrating to and binding with an uncoordinated linker.[32] For laminar MOFs such as CuBDC, this means that adsorbed metal ions either migrate to the sheet's edge or nucleate a new sheet. In this case, nucleation of new lamina is restricted in the reagent-limited growth region of the layered reaction setup. This results in particles that are composed of a relatively small number of internal lamina. The termination of the dominant plane is simply the face of a laminar sheet. The lateral edges of the sheet are likely composed of dangling BDC linkers since an unsaturated copper complex would undergo rapid substitution at the bottom of the reactor where completed sheets settle and dissolved linkers are in excess. Carboxylic acid groups at the edges are likely to interact with water or ethanol however the minimization of the overall particle thickness also minimizes their contribution to the desorption signal.

Figure 2 illustrates the crystal structure of the CuBDC nanosheets. The PXRD pattern in Figure 2a shows only two reflections and these correspond to the $(\bar{2}01)$ plane and the higher order $(\bar{4}02)$ reflection. While the three-dimensional analog's PXRD pattern has many peaks, only these two peaks are visible because the particles lie flat in the plane of the sample holder.[12] Figure 2b shows the crystal structure of CuBDC and its orientation relative to the nanosheet geometry. Because of the stacking pattern, the pores do not run normal to the sheet particle's face. As a result, the lengths of pores are somewhat longer than the thicknesses of the particles.

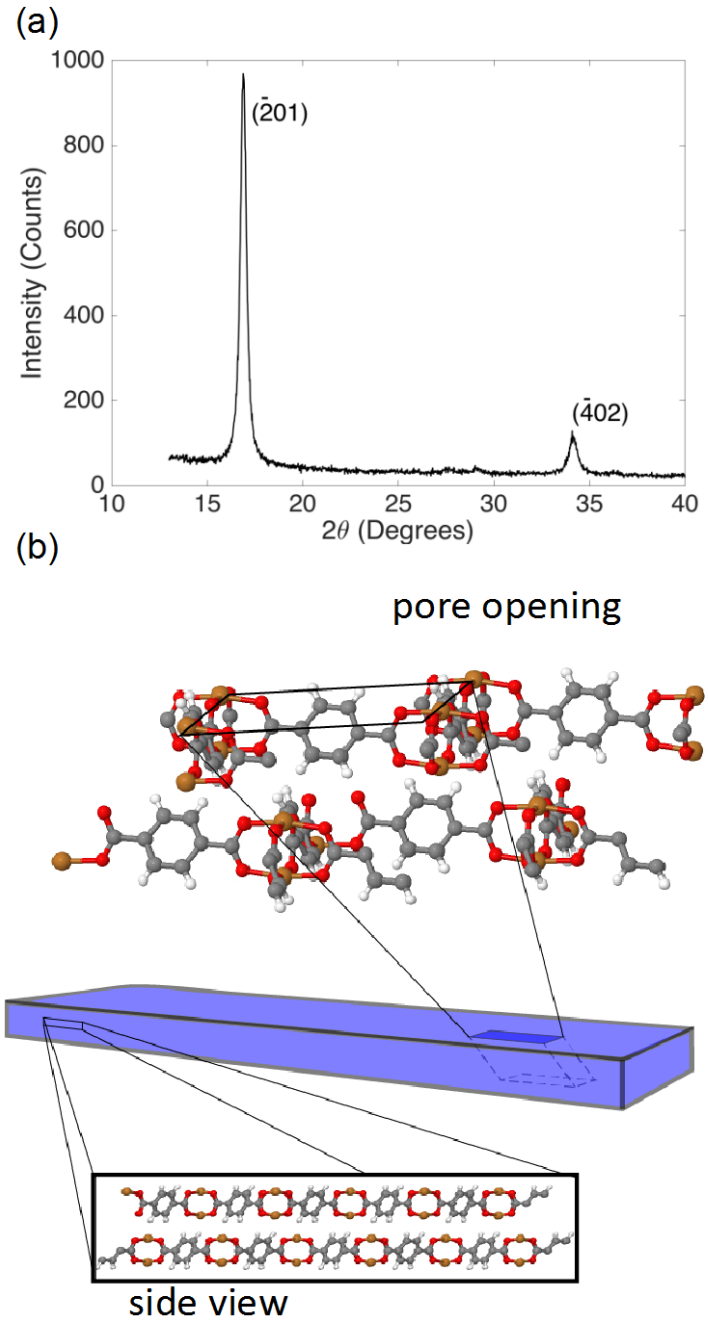

Figure 4.2 Powder X-ray diffraction pattern of CuBDC nanosheets (a) and diagram of the crystal structure (b), including its orientation with respect to the shape of the nanosheets. Copper, oxygen, hydrogen, and carbon atoms are shown in brown, red, white, and grey respectively.

The BET surface area of the material was measured to be 269 m^2/g. Given the large surface area, measuring the absolute loading resulting from a given exposure is difficult. The specific surface area of the material has been reported as high as 902 m^2/g and was achieved using a high activation temperature while various wash procedures have been shown to allow partial activation at lower temperatures.[12, 33] The surface area obtained in this work was achieved by sequential solvent exchanges with acetonitrile and dichloromethane followed by thermal activation at 150 ˚C and is consistent with Kim *et al*'s results.[34] The procedure followed in our work was chosen to minimize thermally induced defects in the lattice that might unnecessarily complicate the TPD signal. Additionally, by allowing some crystal domains to remain closed off due to the lattice orientation, the fraction of the total surface area that is comprised by the external surface is increased from 5% to 17%. Instead of fully loading the MOF film with adsorbate, doses were simply measured in Langmuir for consistency and it is assumed that full loading wasn't reached. Indeed, with increasing doses, the resulting change in integrated signal intensity did decrease but did not level off.

Figure 3 shows FT-IR (a) and Raman (b) spectra of activated CuBDC samples that were measured to confirm that the pores were clear of organic solvents. The peaks at 2966 cm^{-1} and 3069 cm^{-1} in the FT-IR spectrum correspond to the aromatic C-H stretching modes while bending mode overtones can be observed at 1940 cm^{-1} and 1838 cm^{-1}. The strong absorption at 1693 cm^{-1} corresponds to carbonyl C=O groups that terminate the edges of the sheets, this matches the broad carboxylic acid O-H peak centered at 3000 cm^{-1}. The C-O stretches of coordinated linkers are shifted to lower frequency from the uncoordinated carboxylate groups, appearing at 1387 cm^{-1}. The absorptions corresponding to C=C stretching in the aromatic ring of

the linker are located at 1425 cm^{-1}, 1508 cm^{-1}, and 1570 cm^{-1}. The broad peak at 3431 cm^{-1} is attributed to water that has filled the activated pores of the material.

The Raman spectrum largely mirrors the FT-IR spectrum, with the aromatic C-H stretch appearing at 3078 cm^{-1} and the C=C stretch at 1615 cm^{-1}. Peaks at 1425 cm^{-1} and 1518 cm^{-1} correspond to asymmetric and symmetric C-O stretches respectively. The BDC ring stretch can be seen at 1141 cm^{-1}. There is no indication that significant concentrations of the solvents used: acetonitrile, N, N-dimethylformamide, or dichloromethane, are present in the sample prior to the adsorption and TPD measurements.

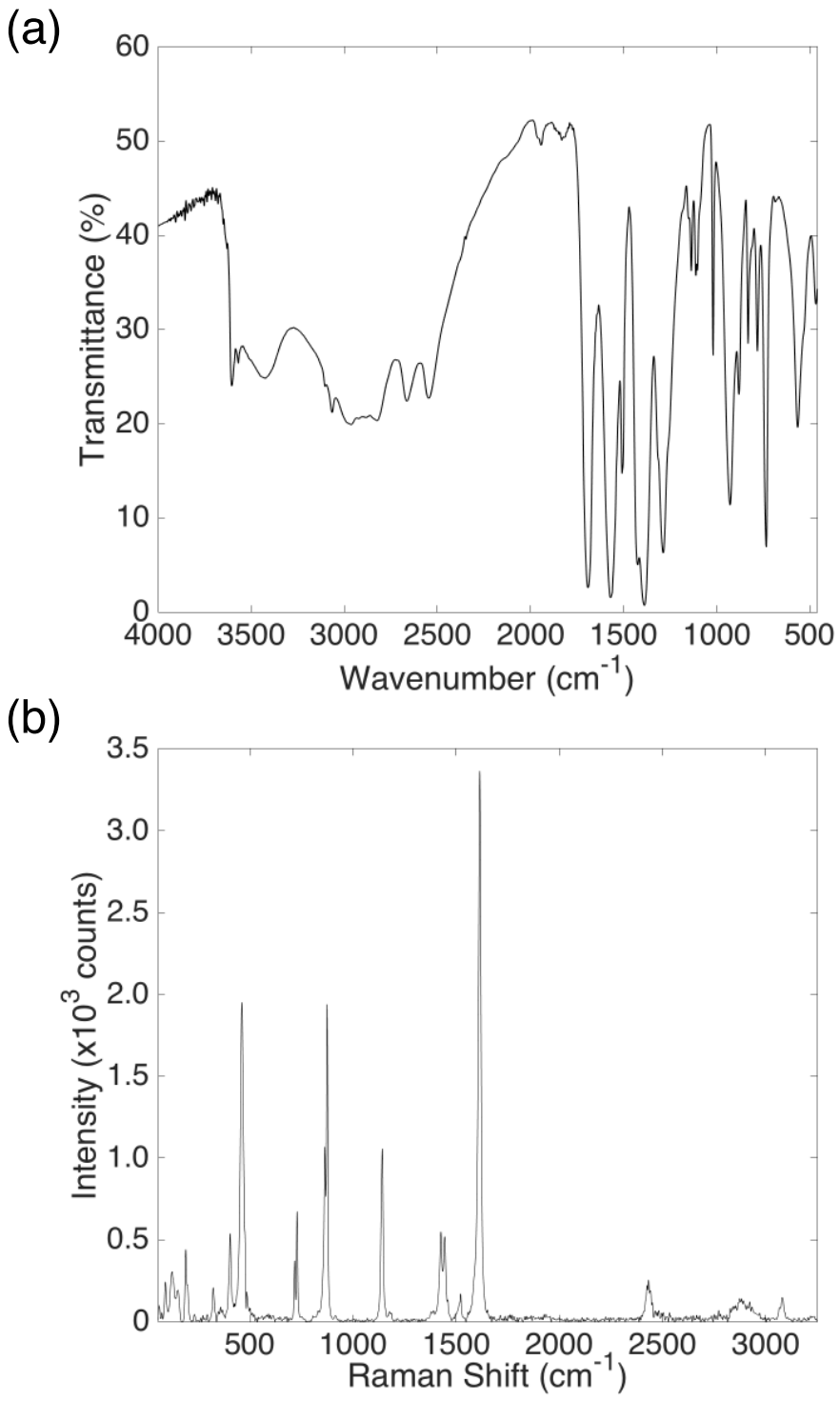

Figure 4.3 FT-IR (a) and Raman (b) spectra of activated CuBDC nanosheets. Note that there is no evidence for the presence of solvent in the pores.

4.3.2 Qualitative analysis of TPD spectra

TPD was originally developed to measure desorption kinetics from well-defined crystalline surfaces.[35] Correct application of TPD theory and interpretation of the signal is therefore dependent on having a well-controlled and understood MOF sample. As the preceding analysis demonstrates, the CuBDC nanosheet system has been sufficiently controlled such that rigorous analysis of the TPD results can be performed.

Figure 3 shows TPD plots for ethanol and water adsorbed to identical CuBDC samples. Water desorption was monitored via the m/z = 18 molecular ion current and has a dominant peak centered at 220 K. The behavior of water desorption above 360 K is complicated by a strong background signal that is difficult to subtract reliably. None of the peak positions change as a function of exposure, indicating that the desorption kinetics are first order. Because the reaction is first order and the adsorbed species are stable molecules, we characterize the adsorption of water to CuBDC as primarily physical adsorption or strong physisorption.

A small signal was also observed in the water TPD signal at 170-180 K. The tail is obscured by the main peak and it seems to be saturated by exposures lower than 16 L. This signal appears in the background spectrum as well and is likely condensation of background water inside the chamber that occurred when the stage was cooled below 180 K.

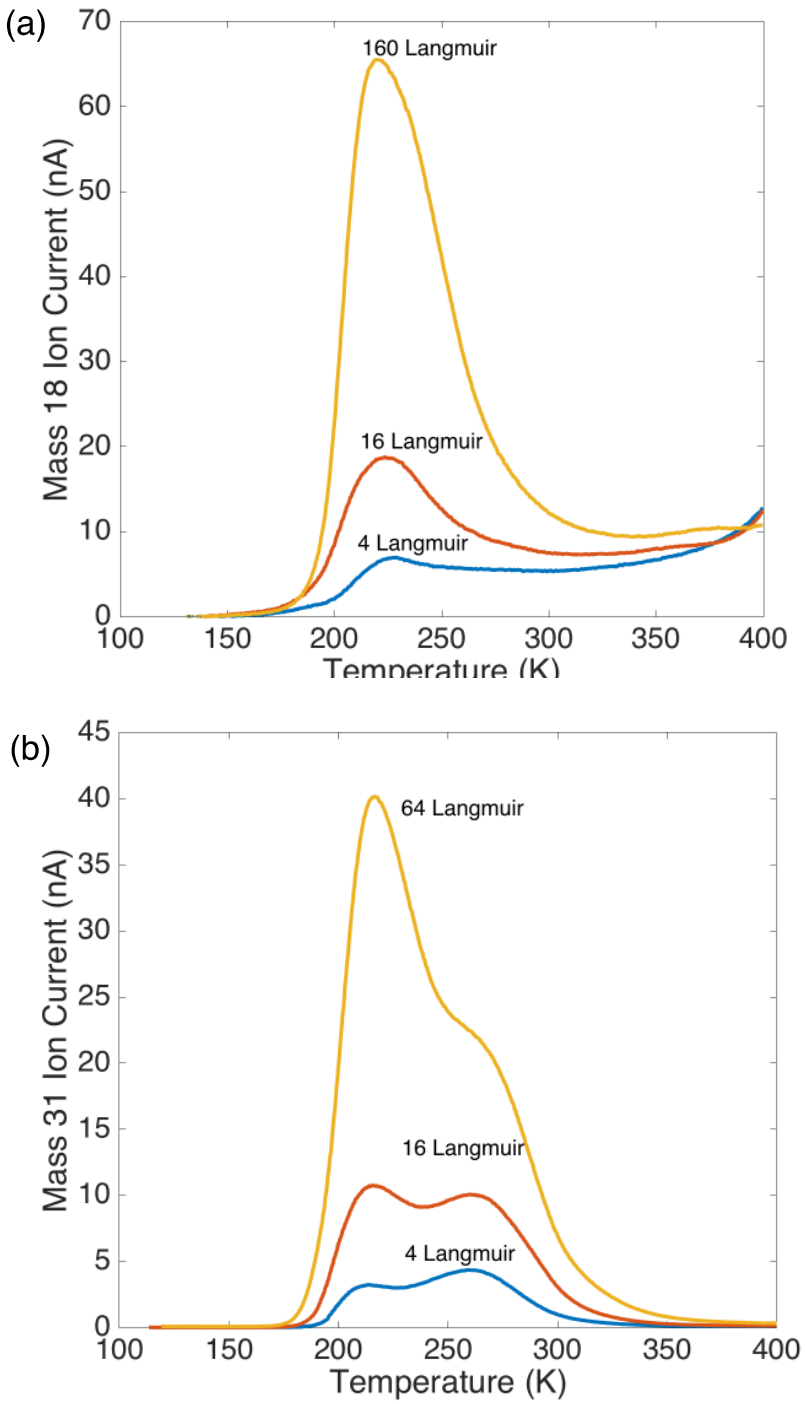

Figure 4.4 Temperature programmed desorption plots of water (a) and ethanol (b) from CuBDC nanosheets.

Ethanol desorption was monitored by the m/z = 31 ion current that corresponds to a $[CH_2OH]^+$ fragment, which is the dominant peak in the ethanol mass spectrum. The ethanol signal has two peaks, the first centered at 213 K and the second at 260 K. This indicates that ethanol molecules bind to at least two distinct sites with different activation energies of desorption. The first matches water closely while the second has no analog in the water TPD signal, indicating that water either is not interacting with these sites or it is interacting with both sites with the same binding energy. The ethanol peak at 213 K grows faster with exposure than the peak at 260 K. This indicates that the higher energy sites are approaching saturation earlier. The fact that saturation of the lower energy sites is not reached implies that these are more abundant and likely internal metal sites.

We hypothesize that the peak at 260 K in the ethanol signal corresponds to the external metal sites because the molecule can bind in a more stable configuration that is sterically inaccessible at the interior sites. Figure 5 demonstrates the proposed binding configurations of water and ethanol at external and internal sites. Note that water is smaller and the proximity of the aromatic rings of the linkers does not influence its adsorption configuration. We propose that the minimum energy configuration sees the oxygen associated with the positively polarized copper center while the hydrogens are positioned adjacent to the negatively polarized oxygen atoms. Alternatively, the ethanol molecule orients at the surface site such that its aliphatic region is aligned with the edge of the linker. In this configuration, the ethanol associates via hydrogen bonding to an oxygen bound to copper as well as through dispersion forces between the hydrocarbons and the edge of the aromatic ring. The X-ray diffraction peak at 16.64˚ is associated with the $(\bar{2}01)$ plane along which the internal lamina stack. It has a d-spacing of 5.4 Å and a resulting inter-laminar spacing of 3.3 Å. Due to the small distances between internal

sheets and their staggered stacking pattern, edge-on interactions with the aromatic rings of the linkers are sterically inaccessible to ethanol molecules adsorbed to internal sites. Therefore, the binding strength of ethanol to interior sites is comparable to that of water on both internal and external sites.

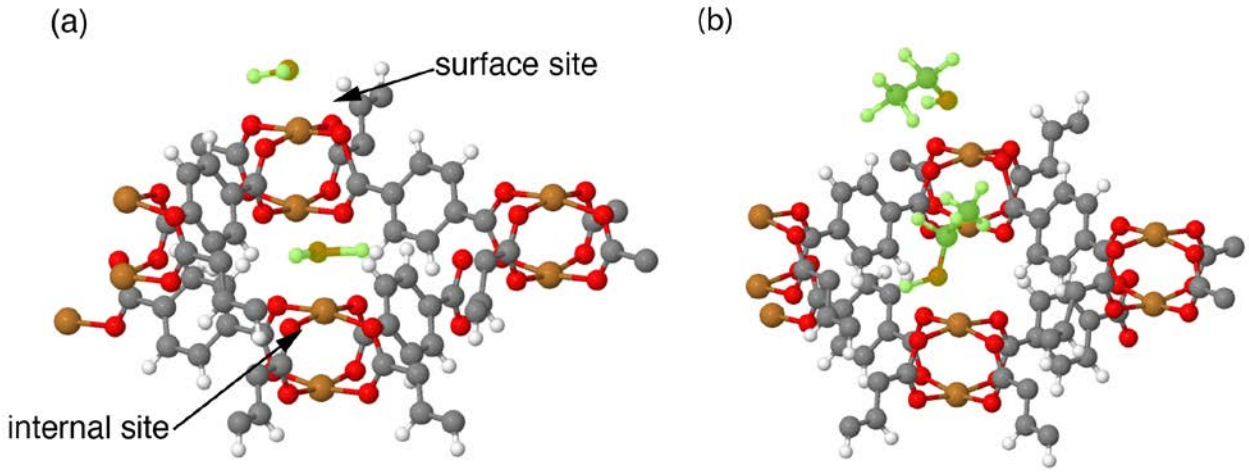

Figure 4.5. Proposed adsorption configurations of water (a) and ethanol (b) at internal and external metal sites. Atoms have been removed from the structure for clarity. Copper, oxygen, hydrogen, and carbon atoms are shown in brown, red, white, and grey respectively. Adsorbed atoms are highlighted in green.

In view of this hypothesis, the activation energy of ethanol desorption at the external surface should be shifted by the strength of the dispersion interaction between the aromatic ring and the BDC linker. The excess molar enthalpy of ethanol-benzene mixtures has been reported to be -14.0 kJ/mol.[36] This suggests that the activation energy of desorption of ethanol from external surfaces may be increased by approximately half this amount due to the reduced number of interactions in the adsorbed state vs. a fully solvated state in an ethanol-benzene solution.

4.3.3 Quantitative analysis of TPD signal

Conventional quantitative analysis of TPD results assumes that the mass signal, σ, is proportional to the desorption rate, which is the rate limiting step in the experiment.[35] In this case, diffusion through the sample film and transport occur on much shorter timescales than the desorption step. Given a linear temperature ramp with rate α from initial temperature T_0, the TPD signal is proportional to the rate of change of the fractional surface coverage $\sigma \propto \partial\theta/\partial t$. For surfaces with n distinct types of sites the signal is proportional to the sum of the rates of change of the fractional coverage of each site $\sigma \propto \sum_{i=1}^{n} \partial\theta_i/\partial t$. The relative site density and surface bond vibrational frequency of site i are given by ρ_i and ν_i respectively.

$$\sum_{i=1}^{n} \frac{\partial \theta_i}{\partial t} = -\sum_{i=1}^{n} \rho_i \theta_i \nu_i \exp\left(\frac{-E_{a,i}}{R(T_0 + \alpha t)}\right) \tag{4.1}$$

Due to the small pore size of CuBDC and the efficient packing enabled by the nanosheet geometry, diffusion through the sample bed is slow and its influence can be seen in the rounded peaks and long tails of the TPD signals. To extract the kinetic parameters from the signal, the diffusion process must be accounted for. This was accomplished by incorporating equation (4.1) into a binary desorption-diffusion model. Equation (4.2) is the mass balance for this model based on Fick's law. In this case, the signal is proportional to the flux across the surface of the sample film. The concentration C is a function of time and position z and must be solved to simulate the signal.

$$\frac{\partial C}{\partial t} = D(t)\frac{\partial^2 C}{\partial z^2} + \sum_{i=1}^{n} \rho_i \theta_i \nu_i \exp\left(\frac{-\mathrm{E_{a,i}}}{\mathrm{R(T_0 + \alpha t)}}\right) - \sum_{i}^{n} \rho_i (1-\theta_i)\mathrm{k_{rev,i}} \tag{4.2}$$

The sample film was 1 mm thick spread over 1 cm^2, meaning diffusion in the z-axis dominates the mass transfer process and the lateral dimensions can be neglected. The first summation on the

right-hand side of the equation is the desorption rate as described in equation (4.1). The second summation is the re-adsorption rate, which is dependent only on the abundance of open sites and the collisional cross section of those sites; physical adsorption is not an activated process and this term is therefore independent of temperature. The diffusion coefficient is temperature dependent and is computed using kinetic theory as shown in equation (4.3).

$$D(t) = \min\{\lambda, d\}\frac{\delta}{3}\sqrt{\frac{8k_B(T_0 + \alpha t)}{\pi m_{gas}}} \tag{4.3}$$

The mass of the gas is given by m_{gas}. The coefficient δ is an empirical correction for the tortuosity and constrictivity of the pore structure. The parameters λ and d are the kinetic mean free path and pore diameter respectively. The initial condition is complete coverage of surface sites with an otherwise evacuated film. The system is bounded by a no-flux Neumann boundary condition at the bottom surface and zero concentration Dirichlet boundary condition at the upper surface, corresponding to the ultra-high vacuum environment of the chamber. No analytical solution to equation (4.2) exists so this system was solved using the finite difference approximation and fit to the data according to the least squares criterion. The sum of squared residuals is non-linear in this case and, in addition to being non-convex, the solution space also contains numerically unstable combinations of parameters. To constrain the curve fitting process to stable parameter choices and avoid convergence to sub-optimal local minima, MATLAB's genetic algorithm was used to minimize the sum of squared residuals. The fit parameters included the activation energies $E_{a,i}$, initial site concentrations $\rho_i\theta_{i,0}$, diffusion coefficient correction factor δ, and re-adsorption rate constants $k_{rev,i}$. The vibrational frequency was assumed to be 10^{13} s^{-1}, which is typical of metal-hydroxyl physisorption interactions. Both the simulated and experimental signals were normalized to allow comparison.

Figure 4.6 shows fits for 16 L exposure of water (a) and 4 L exposure of ethanol (b). These exposures were chosen for the fitting procedure because each had the best peak definition of the exposure levels surveyed. This experiment was repeated and fit three times for each gas; the extracted parameters are given in tables 4.1 and 4.2. The small variances in the extracted parameters reflect the reproducibility of the experiment and the close fit of the proposed model. The water signal was truncated at 360 K because, as mentioned previously, above this temperature the strong background signal obscures the signal from the sample.

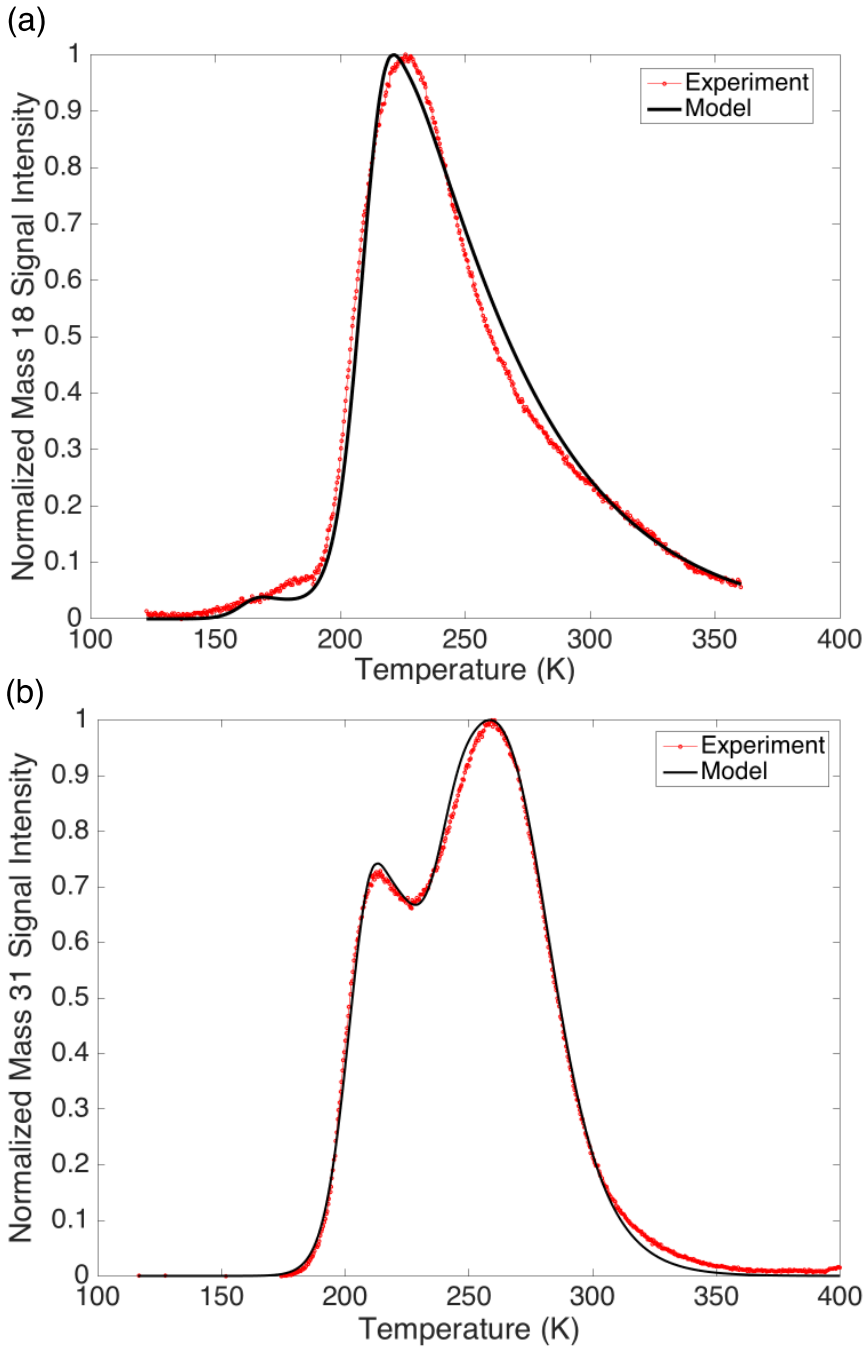

Figure 4.6 Overlays of simulated (solid black line) and measured (dotted red line) desorption profiles of 16L water (a) and 4L ethanol (b).

Each fit parameter corresponds to a different aspect of the signal's shape. The activation energies dictate where the centers of the peaks are located. The site concentrations correspond to the overall intensity of each peak and because the total loading of the sample was unknown these may be interpreted as the initial loading per unit area. The empirical diffusion coefficient correction δ, which measures deviation from the kinetic Knudsen diffusion model given by equation (4.3), impacts the weight of the tails of the signals, particularly at higher temperatures, far from the peak. Smaller values of δ cause the tail to be heavier with the signal taking longer to return to the baseline. Only one value of δ is extracted for a given species and it is a measure of mass transfer rate averaged over transport both inside and outside the pores. The re-adsorption rate $k_{rev,i}$ can be interpreted as being proportional to the scattering cross section of an adsorption site, which is only relevant at temperatures near the desorption temperature or at high pressures. Thus, the re-adsorption rate constant determines the roundedness of the top of the peak.

Table 4.1 Fit parameters for pure water desorption

Peak Position (K)	E_a (kJ/mol)	$k_{rev,i}$ (s^{-1})
180	44 ± 2	1.1 ± 1.7
220	58 ± 1	0.40 ± 0.21

Table 4.2 Fit parameters for pure ethanol desorption

Peak Position (K)	E_a (kJ/mol)	$k_{rev,i}$ (s^{-1})
213	58 ± 1	0.2 ± 0.01
260	66 ±0 .4	0.8 ± 0.05

The high temperature peak in the ethanol signal corresponds to an activation energy of desorption that is 8 kJ/mol greater than that of the 213 K peak. This is consistent with the hypothesis posited on page 14 that the activation energy may be shifted by interactions with the aromatic ring. The measured value of 8 kJ/mol is roughly half that of the excess molar enthalpy of ethanol-benzene mixtures. As already mentioned, this could be due to the reduced interactions at the surface relative to a more fully solvated ethanol molecule. The deviation from ethanol-benzene mixtures may also be attributed to the electron withdrawing carboxylate groups of terephthalic acid. The values of δ extracted from the water and ethanol data were and 0.3 ± 0.13 and 0.2 ± 0.02 respectively. This discrepancy may be due to attractive interactions between diffusing ethanol and the organic linkers that is not explicitly accounted for in the model.

4.3.4 Co-adsorption of water and ethanol

To better understand the differences between internal and surface sites as well as the interactions between adsorbates, simultaneous desorption of water and ethanol was measured. The shape of the desorption profile was independent of the order in which the sample was exposed to the gases and the ethanol signal did not change compared to that of the pure exposure. However, the water signal is dramatically different in the presence of ethanol. Figure 7 shows a fit overlay of typical TPD profiles of co-adsorbed water and ethanol from CuBDC nanosheets. The main difference in water's TPD signal in the presence of ethanol is a new peak centered at 260 K. The extracted desorption parameters averaged over three trials are given in table 3. The low temperature edge feature and high temperature tail of the water signal were excluded from the set in the fit algorithm.

The activation energy of desorption associated with the water peak centered at 220 K is unchanged between the two experiments while the activation energy associated with the higher temperature peak is 68 kJ/mol. This is 2 kJ/mol larger than the activation energy extracted from the higher temperature ethanol peak centered at 258 K. This can be explained by contributions of both co-adsorbed surface water-ethanol complexes and singly adsorbed surface ethanol molecules contributing to the TPD signal. Given the similarities in desorption activation energy it is impossible to separate these components of the signal.

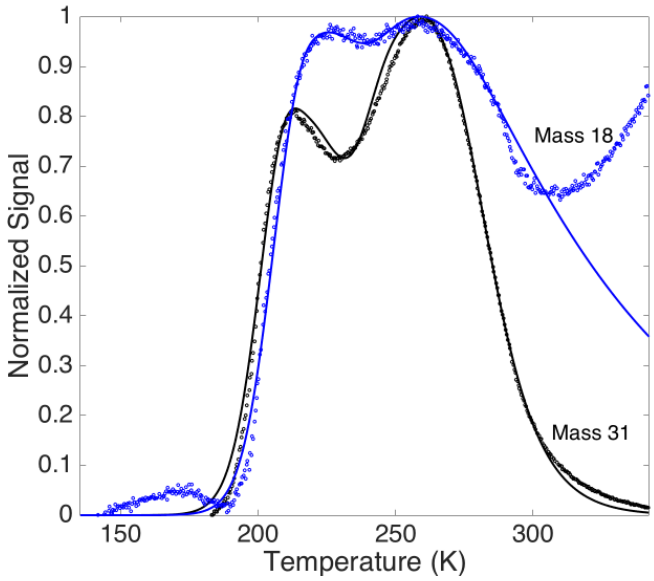

Figure 4.7 TPD traces of co-adsorbed ethanol and water from CuBDC (4 L each). Measured mass 18 (violet, water) and mass 31 (black, ethanol) signals shown as open circles. Simulated signals shown as solid lines of the corresponding color.

Table 4.3 Fit parameters for co-adsorbed gas desorption profiles

Adsorbate	Peak Position	E_a (kJ/mol)	$k_{rev,i}$(s^{-1})
H_2O	225	58 ± 0.2	0.60 ± 0.3
H_2O	260	68 ± 0.7	1.1 ± 0.6
Ethanol	214	57 ± 0.3	0.2 ± 0.01
Ethanol	258	66 ± 0.3	1.1 ± 0.2

The diffusion coefficient correction terms δ extracted for co-adsorbed water and ethanol were 0.05 ± 0.01 and 0.3 ± 0.02 respectively. The slight difference between the values for co-adsorbed ethanol and pure ethanol can be attributed to the fact that the co-adsorption experiments were run after the single-gas experiments and the packing density of the sample bed may have changed after repeated heating and cooling cycles. The change in the correction term for water is much larger because much of the higher energy peak's tail is obscured, reducing the accuracy of the fit.

A result of the higher temperature water signals obscurity is that mechanistic data is difficult to extract. However, the retention of water at higher temperatures in the presence of ethanol suggests that the more strongly interacting ethanol molecules, which we have attributed to surface sites, interact with water to form stable hydrogen-bond complexes. A possible configuration for such a complex can be found in Figure 4.8. In this model, the water hydrogen that is bent away from the linker oxygen in the single adsorption case is instead associated with the ethanol oxygen.

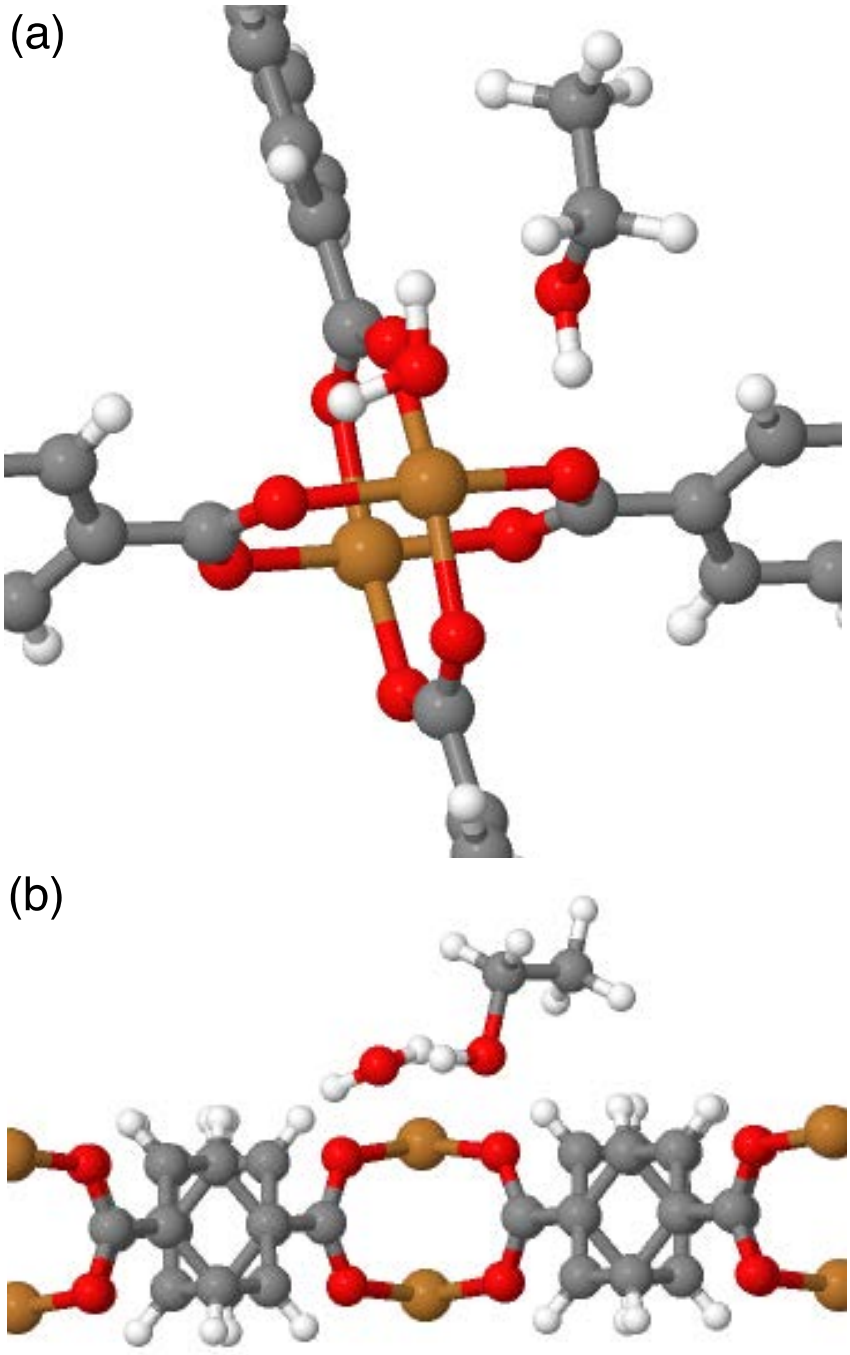

Figure 4.8 Proposed water-ethanol adsorption complex at an external CuBDC surface site shown from top-down (a) and side (b) views. Internal lamina omitted for clarity. Copper, oxygen, hydrogen, and carbon atoms are shown in brown, red, white, and grey respectively.

The interactions between water and ethanol in solution are very complicated and have been the topic of active research for decades.[24-26] Ethanol-water hydrogen bond enthalpies range from 16-25 kJ/mol in binary mixtures.[37] Thus, the retention of water at higher temperatures in the co-adsorbed system cannot be explained simply by water hydrogen bonding to ethanol at the surface. Rather, it is probable that water and ethanol form a complex at external surface sites with ethanol oriented as described above. Water is then positioned such that it is involved in three hydrogen bonds: 1) with ethanol's hydroxyl hydrogen, 2) with a carboxylate oxygen, and 3) with ethanol's oxygen. This configuration, shown in Figure 4.8, would include enough hydrogen bonds to equal the measured activation energy of desorption.

4.3 Conclusion

We have examined the interactions of pure and co-adsorbed water and ethanol with CuBDC nanosheets. Water desorbs with activation energies of 44±2 kJ/mol at edge sites and 58±1 kJ/mol at internal and surface sites while ethanol desorbs with activation enthalpies of 58±1 and 66±0.4. Co-adsorption of water and ethanol demonstrated the importance of adsorbate behavior at MOF external surfaces. Specifically, adsorbate-adsorbate interactions at the surface cause water to remain at higher temperatures, desorbing with an activation energy of 68 ± 0.7kJ/mol. This work shows that interactions at the external surfaces of MOF crystals can be probed using nanosheet analogs and that quantitative kinetic and transport parameters can be reliably extracted from diffusion-impacted TPD signals. Given that the adsorption/desorption behaviors of water and ethanol with this material are similar when co-adsorbed, its utility in separations will depend on the variation in the diffusivity mainly within the pores.

4.5 References

1. Elder, A. C.; Aleksandrov, A. B.; Nair, S.; Orlando, T. M., Interactions on External Mof Surfaces: Desorption of Water and Ethanol from CuBDC Nanosheets. *Langmuir* **2017**, *33*, 10153-10160.
2. Rowsell, J. L. C.; Yaghi, O. M., Metal–Organic Frameworks: A New Class of Porous Materials. *Micropor. Mesopor. Mater.* **2004**, *73*, 3-14.
3. Huang, L.; Wang, H.; Chen, J.; Wang, Z.; Sun, J.; Zhao, D.; Yan, Y., Synthesis, Morphology Control, and Properties of Porous Metal–Organic Coordination Polymers. *Micropor. Mesopor. Mater.* **2003**, *58*, 105-114.
4. Deng, H.; Doonan, C. J.; Furukawa, H.; Ferreira, R. B.; Towne, J.; Knobler, C. B.; Wang, B.; Yaghi, O. M., Multiple Functional Groups of Varying Ratios in Metal-Organic Frameworks. *Science* **2010**, *327*, 846-850.
5. Ferey, G.; Serre, C., Large Breathing Effects in Three-Dimensional Porous Hybrid Matter: Facts, Analyses, Rules and Consequences. *Chem. Soc. Rev.* **2009**, *38*, 1380-1399.
6. Czaja, A. U.; Trukhan, N.; Muller, U., Industrial Applications of Metal-Organic Frameworks. *Chem. Soc. Rev.* **2009**, *38*, 1284-1293.
7. Mueller, U.; Schubert, M.; Teich, F.; Puetter, H.; Schierle-Arndt, K.; Pastre, J., Metal-Organic Frameworks-Prospective Industrial Applications. *J. Mater. Chem.* **2006**, *16*, 626-636.
8. Li, J.-R.; Kuppler, R. J.; Zhou, H.-C., Selective Gas Adsorption and Separation in Metal-Organic Frameworks. *Chem. Soc. Rev.* **2009**, *38*, 1477-1504.
9. de Lima, G. F.; Mavrandonakis, A.; de Abreu, H. A.; Duarte, H. A.; Heine, T., Mechanism of Alcohol–Water Separation in Metal–Organic Frameworks. *J. Phys. Chem. C* **2013**, *117*, 4124-4130.
10. Hill, J.; Nelson, E.; Tilman, D.; Polasky, S.; Tiffany, D., Environmental, Economic, and Energetic Costs and Benefits of Biodiesel and Ethanol Biofuels. *Proc. Natl. Acad. Sci. U.S.A.* **2006**, *103*, 11206-11210.
11. Peng, Y.; Li, Y.; Ban, Y.; Jin, H.; Jiao, W.; Liu, X.; Yang, W., Metal-Organic Framework Nanosheets as Building Blocks for Molecular Sieving Membranes. *Science* **2014**, *346*, 1356-1359.
12. Rodenas, T.; Luz, I.; Prieto, G.; Seoane, B.; Miro, H.; Corma, A.; Kapteijn, F.; Llabrés i Xamena, F. X.; Gascon, J., Metal–Organic Framework Nanosheets in Polymer Composite Materials for Gas Separation. *Nat Mater* **2015**, *14*, 48-55.
13. Xu, H.; Gao, J.; Qian, X.; Wang, J.; He, H.; Cui, Y.; Yang, Y.; Wang, Z.; Qian, G., Metal-Organic Framework Nanosheets for Fast-Response and Highly Sensitive Luminescent Sensing of Fe^{3+}. *J. Mater. Chem. A* **2016**, *4*, 10900-10905.
14. Zhan, G.; Zeng, H. C., Synthesis and Functionalization of Oriented Metal–Organic-Framework Nanosheets: Toward a Series of 2d Catalysts. *Adv. Funct. Mater.* **2016**, *26*, 3268-3281.

15. Li, Y.-N.; Wang, S.; Zhou, Y.; Bai, X.-J.; Song, G.-S.; Zhao, X.-Y.; Wang, T.-Q.; Qi, X.; Zhang, X.-M.; Fu, Y., Fabrication of Metal–Organic Framework and Infinite Coordination Polymer Nanosheets by the Spray Technique. *Langmuir* **2017**, *33*, 1060-1065.
16. Laokroekkiat, S.; Hara, M.; Nagano, S.; Nagao, Y., Metal–Organic Coordination Network Thin Film by Surface-Induced Assembly. *Langmuir* **2016**, *32*, 6648-6655.
17. Feldblyum, J. I.; Liu, M.; Gidley, D. W.; Matzger, A. J., Reconciling the Discrepancies between Crystallographic Porosity and Guest Access as Exemplified by Zn-Hkust-1. *J. Am. Chem. Soc.* **2011**, *133*, 18257-18263.
18. Nguyen, J. G.; Cohen, S. M., Moisture-Resistant and Superhydrophobic Metal−Organic Frameworks Obtained Via Postsynthetic Modification. *J. Am. Chem. Soc.* **2010**, *132*, 4560-4561.
19. Tan, K.; Nijem, N.; Gao, Y.; Zuluaga, S.; Li, J.; Thonhauser, T.; Chabal, Y. J., Water Interactions in Metal Organic Frameworks. *CrystEngComm* **2015**, *17*, 247-260.
20. Todaro, M.; Buscarino, G.; Sciortino, L.; Alessi, A.; Messina, F.; Taddei, M.; Ranocchiari, M.; Cannas, M.; Gelardi, F. M., Decomposition Process of Carboxylate MOF HKUST-1 Unveiled at the Atomic Scale Level. *J. Phys. Chem. C* **2016**, *120*, 12879-12889.
21. Zang, J.; Nair, S.; Sholl, D. S., Prediction of Water Adsorption in Copper-Based Metal–Organic Frameworks Using Force Fields Derived from Dispersion-Corrected Dft Calculations. *J. Phys. Chem. C* **2013**, *117*, 7519-7525.
22. Balat, M.; Balat, H.; Öz, C., Progress in Bioethanol Processing. *Prog. Energy Combust. Sci.* **2008**, *34*, 551-573.
23. Huang, H.-J.; Ramaswamy, S.; Tschirner, U. W.; Ramarao, B. V., A Review of Separation Technologies in Current and Future Biorefineries. *Sep. Purif. Technol.* **2008**, *62*, 1-21.
24. Mulder, M. H. V.; Hendrickman, J. O.; Hegeman, H.; Smolders, C. A., Ethanol—Water Separation by Pervaporation. *J. Membr. Sci.* **1983**, *16*, 269-284.
25. Egashira, K.; Nishi, N., Low-Frequency Raman Spectroscopy of Ethanol−Water Binary Solution: Evidence for Self-Association of Solute and Solvent Molecules. *J. Phys. Chem. B* **1998**, *102*, 4054-4057.
26. Shigematsu, A.; Yamada, T.; Kitagawa, H., Selective Separation of Water, Methanol, and Ethanol by a Porous Coordination Polymer Built with a Flexible Tetrahedral Ligand. *J. Am. Chem. Soc.* **2012**, *134*, 13145-13147.
27. Li, Y.; Wang, X.; Xu, D.; Chung, J. D.; Kaviany, M.; Huang, B., H_2O Adsorption/Desorption in MOF-74: Ab Initio Molecular Dynamics and Experiments. *J. Phys. Chem. C* **2015**, *119*, 13021-13031.
28. Dauphin-Ducharme, P.; Arroyo-Currás, N.; Kurnik, M.; Ortega, G.; Li, H.; Plaxco, K. W., Simulation-Based Approach to Determining Electron Transfer Rates Using Square-Wave Voltammetry. *Langmuir* **2017**, *33*, 4407-4413.
29. Barrie, P. J., Analysis of Temperature Programmed Desorption (Tpd) Data for the Characterisation of Catalysts Containing a Distribution of Adsorption Sites. *Phys. Chem. Chem. Phys.* **2008**, *10*, 1688-1696.
30. Ishiguro, S.-i.; Jeliazkova, B. G.; Ohtaki, H., A Calorimetric Study of N,N-Dimethylformamide Complexes of Copper(Ii) in Acetonitrile. *J. Solution Chem.* **1987**, *16*, 1-10.
31. Poston, M. J.; Grieves, G. A.; Aleksandrov, A. B.; Hibbitts, C. A.; Darby Dyar, M.; Orlando, T. M., Water Interactions with Micronized Lunar Surrogates JSC-1A and Albite under Ultra-High Vacuum with Application to Lunar Observations. *J. Geophys. Res. E* **2013**, *118*, 105-115.

32. Patterson, J. P.; Abellan, P.; Denny, M. S.; Park, C.; Browning, N. D.; Cohen, S. M.; Evans, J. E.; Gianneschi, N. C., Observing the Growth of Metal–Organic Frameworks by in Situ Liquid Cell Transmission Electron Microscopy. *J. Am. Chem. Soc.* **2015**, *137*, 7322-7328.
33. Carson, C. G.; Brunnello, G.; Lee, S. G.; Jang, S. S.; Gerhardt, R. A.; Tannenbaum, R., Structure Solution from Powder Diffraction of Copper 1,4-Benzenedicarboxylate. *European Journal of Inorganic Chemistry* **2014**, *2014*, 2140-2145.
34. Kim, H. K.; Yun, W. S.; Kim, M.-B.; Kim, J. Y.; Bae, Y.-S.; Lee, J.; Jeong, N. C., A Chemical Route to Activation of Open Metal Sites in the Copper-Based Metal–Organic Framework Materials Hkust-1 and Cu-MOF-2. *J. Am. Chem. Soc.* **2015**, *137*, 10009-10015.
35. King, D. A., Thermal Desorption from Metal Surfaces: A Review. *Surf. Sci.* **1974**, *47*, 384-402.
36. Massucci, M.; Wormald, C. J.; Yan, L., Excess Molar Enthalpies of Ethanol-Hexane, Ethanol-Cyclohexane and Ethanol-Benzene from 453.5 to 522.9 K and up to 4.5 MPa. *J. Chem. Soc., Faraday Trans.* **1993**, *89*, 4193-4197.
37. Dolenko, T. A.; Burikov, S. A.; Dolenko, S. A.; Efitorov, A. O.; Plastinin, I. V.; Yuzhakov, V. I.; Patsaeva, S. V., Raman Spectroscopy of Water–Ethanol Solutions: The Estimation of Hydrogen Bonding Energy and the Appearance of Clathrate-Like Structures in Solutions. *J. Phys. Chem. A* **2015**, *119*, 10806-10815.

CHAPTER 5. VARIATIONAL BAYESIAN INFERENCE FOR SURFACE SIGNAL ANALYSIS

5.1 Introduction

It was shown in chapter 2 that, given sufficient peak resolution, nonlinear surface signals can be decomposed reliably. However, the analysis of metal-organic framework surfaces discussed in chapter 4 showed that such resolution may be unavailable. In such cases, the analyst proposes a number of shape and position parameters based on their knowledge of the system and refines this knowledge using the subsequent least squares fit. This external knowledge, which may include the sample's crystal structure, stoichiometry, and polar functionality, is then used to qualitatively justify the choice of model parameters in the context of the fit results. The fundamental drawback of combining qualitative and quantitative arguments in this way is that it obscures the assumptions that led to the initial choice in fit parameters.

Bayesian methods offer an alternative perspective to data modelling that interprets the fit parameters themselves to be random variables.[1] The data analyst is able to encode their independent knowledge or beliefs in the possible range of values of these random variables using probability distribution functions (PDFs). These PDFs are called priors, because they represent the analyst's knowledge prior to examining the data set. Bayes theorem is then used to update the prior using the data to construct a new distribution called the posterior. Thus, the posterior estimate of the fit parameters represents a quantitative reconciliation of the external knowledge of the system with the information contained in the data and typically provides a more conservative fit than a basic least squares approach. The alternative to Bayesian statistics is called frequentist statistics and this school of thought considers the experimental data to contain

all possible information regarding the system being studied. The data modeling approaches that have been applied in previous chapters are frequentist methods.

Bayesian methods have historically been criticized in the statistics community for the subjective nature of the prior.[1] In many contexts such criticism may be warranted, however, in the case of nonlinear chemical signal analysis the subjectivity of the prior can be viewed as advantageous. This is because even without the prior, the analyst is imposing an inherently subjective decision in the choice of the number of parameters to use. Moreover, given that nonlinear fit algorithms typically find local minima, the choice in the initial guess is also subjective. The construction of the prior, which may also be used as the initial guess in iterative fitting algorithms, forces the analyst to enumerate and quantify their assumptions independent of the spectral data. This results in high fidelity data analysis and reduces the ambiguity of scientific arguments.

Bayesian models, also known as probabilistic models, have experienced a recent surge in popularity due to their application by the machine learning community. They have also been widely applied in analytical chemistry.[2] Later sections of this chapter will derive an advanced method for Bayesian nonlinear regression analysis. With this in mind, a brief review of conditional probability theory and Bayesian statistics is provided in the next section. Variational approaches for approximating the posterior are introduced in section 3. These are directly analogous to variational methods in computational chemistry. This approach is applied naïvely to Raman spectral analysis in section 4 using Google's Edward probabilistic modeling library.[3] Application of variational inference becomes more complicated when no analytical form for the model function is known, as in the case of TPD modeling.[4] Therefore, the final two sections of

this chapter develop a stochastic gradient construction approach for numerical models and applies it to TPD signal decomposition.

5.2 Bayesian Statistics

The following section is a review of probability theory and Bayesian statistics. These theorems range from 70 to 300 years old and can be found in many undergraduate and graduate level texts. For a complete development of this theory, see David Mackay's *Information Theory, Inference, and Learning Algorithms,* on which the spirit of this section is modeled.[1]

As the name suggests, Bayesian statistics involves the application of Bayes' Theorem to statistical inference. Bayes' Theorem is a fundamental law of probability theory that allows the knowledge of a distribution to be updated as new information arises. We will begin by briefly reviewing the derivation of Bayes' Theorem using conditional probabilities.

Definition 5.1

Consider a discrete space $\Omega = \{\omega_1, \omega_2, \ldots \omega_n\}$ *and define a measure* P *on* Ω *such that* $0 \leq P(\omega_i) \leq 1 \; \forall \; \omega_i \in \Omega$. *We say* $P: \Omega \rightarrow [0,1] \in \mathbb{R}$ *is a probability measure if*

1. $P(\{\emptyset\}) = 0$ *and* $P(\Omega) = 1$ *where* $\{\emptyset\}$ *is the empty set.*
2. P *satisfies the countable additivity property for all countable collections* $\{E_i\}$ *of pairwise disjoint sets:*

$$P\left(\bigcup_{i \in I} E_i\right) = \sum_{i \in I} P(E_i)$$

Note that definition 5.1 implies that the sum of the probabilities of events in Ω sum to 1. This definition also provides a formula for the conditional probability of an event A given some other event B.

$$P(A|B) = \frac{P(A \cap B)}{P(B)} \tag{5.1}$$

$P(A \cap B)$ is the probability that events A and B occur together. If $P(A|B) = P(A)$ the events A and B are said to be independent.

Definition 5.2

A function $X: \Omega \to \mathbb{R}$ is a real valued random variable if it is measurable under some measure P on Ω.

We call $P(X)$ the probability distribution of X and $P(X, Y)$ the joint probability distribution of X and another random variable Y. We can define the conditional probability distribution of X given Y analogously to equation (5.1).

$$P(X|Y) = \frac{P(X, Y)}{P(Y)} \tag{5.2}$$

Note that we have dropped the set notation because we random variables are functions, rather than subsets, of Ω. Equation (5.2) is symmetric in that it can be written equivalently as $P(Y|X)P(X) = P(X|Y)P(Y)$. Now that we can write the conditional probability of X in terms of Y, suppose we wanted to recover the $P(X)$. In that case, denote the domain of Y as $\{y_i\}$ and compute

$$P(X) = \sum_{y_i \in \{y_i\}} P(X|Y = y_i)\, P(Y = y_i). \tag{5.3}$$

This computation is known as *marginalization*. Bayes' theorem follows from this result:

$$P(Y|X) = \frac{P(X|Y)P(Y)}{\sum_{y_i \in \{y_i\}} P(X|Y = y_i)\, P(Y = y_i)} \tag{5.4}$$

In this context, $P(Y)$ is called the prior, as it represents the belief in the probability of Y before observing X. $P(X|Y)$ is the called the likelihood function of X given Y and $P(X) = \sum_{y_i \in \{y_i\}} P(X|Y = y_i)\, P(Y = y_i)$ is called the evidence. The posterior $P(Y|X)$ is the probability distribution of Y given the observation of X. Note that this necessarily can change for different specific values of X and therefore the posterior is at least a bivariate function. These results transfer readily to the continuous case where the probability distribution functions $P(X)$ and $P(Y|X)$ are replaced with continuous probability density functions $f_X(X)$ and $f_{X|Y}(Y|X)$. The summation in the marginalization computation is replaced with an integration over the domain of $f_X(X)$.

In the context of data modeling, equation 4 can be written to reflect prior and posterior estimates of the model parameter vector $\boldsymbol{\pi}$ given a set of observations of the data vector $\boldsymbol{x}$. We also introduce a vector of hyperparameters $\boldsymbol{\Upsilon}$ that define the prior $P(\boldsymbol{\pi}|\boldsymbol{\Upsilon})$.

$$P(\boldsymbol{\pi}|\boldsymbol{x}, \boldsymbol{\Upsilon}) = \frac{P(\boldsymbol{x}|\boldsymbol{\pi}, \boldsymbol{\Upsilon})P(\boldsymbol{\pi}|\boldsymbol{\Upsilon})}{P(\boldsymbol{x}|\, \boldsymbol{\Upsilon})} \tag{5.5}$$

Equation 5 can be solved analytically in very simple cases. Such solutions are covered in detail elsewhere and are outside the scope of this work. Rather than cover these, we will skip to the application of variational Bayesian inference, in which a test distribution is used to approximate the posterior via an optimization algorithm.

5.3 Gradient Ascent Variational Bayesian Inference

Variational methods are commonly employed in statistical physics and quantum chemistry to represent a complex distribution (e.g. of electrons in space) with a simpler,

computationally tractable approximation.[5-6] These methods seek to optimally approximate the true distribution of particles in a system by minimizing the energy of the approximating function over its distribution parameters. Once a sufficiently accurate approximation of the particle distribution is found, it can be generalized to predict the physical properties of the system.

Variational Bayesian inference applies a mechanistically identical procedure to approximate a complex posterior $P(\boldsymbol{\pi}|\boldsymbol{x},\ \boldsymbol{\Upsilon})$. Claude Shannon's generalized the concept of statistical entropy to abstract probability distributions in his development of information theory.[7] This provides a clear path to the formulation of an energy function of an approximating distribution $Q(\boldsymbol{\pi};\boldsymbol{\psi})$ with variational parameters $\boldsymbol{\psi}$**.** Information theoretic entropy is introduced here and will be denoted by $\mathbb{H}$ to distinguish it from the physical entropy $\mathbb{S}$. Though the definitions of these two notions of entropy are mathematically identical, the contexts in which they are applied are quite different and this distinction in notation will be enforced to avoid confusion. The following definitions will be used to derive the variational Bayesian inference algorithm.

Definition 2.1: *Let a sample space X and probability measure P be given. Then the* Shannon information content *of an outcome $x \in X$ is given by*

$$h(x) = \ln \frac{1}{P(x)}.$$

The information theory literature typically defines the Shannon information content using the base-2 logarithm.[1] This is because of the field's historic alignment with computer science and the related importance of the binomial distribution of strings of binary bits. We will be primarily concerned with exponential distributions and thus it is more convenient to define the Shannon

information with the natural logarithm. Units of Shannon information defined as such are measured in units called *nats*, which correspond to increments of Euler's number.

Definition 2.2: *Let a sample space X and probability measure P be given*. Then the *information entropy* of the distribution P is given by

$$\mathbb{H}[P] = \sum_{x \in X} P(x) \ln \frac{1}{P(x)}.$$

If the sample space A is continuous then we use the differential entropy*:*

$$\mathbb{H}[P] = \int_{-\infty}^{\infty} P(x) \ln \frac{1}{P(x)} dx.$$

Intuitively, the Shannon entropy of a probability distribution is the expected value of the information content of the distribution. Entropy's additive properties allow us to define the following measure to compare two distributions.

Definition 2.3: *The* Kullback-Leibler divergence *between distributions $Q(x)$ and $P(x)$ that are defined over the same sample space A is*

$$D_{KL}(Q||P) = \sum_{x \in X} Q(X) \frac{Q(x)}{P(X)}.$$

As with the entropy, the differential analog for continuous sample spaces is

$$D_{KL}(Q||P) = \int_{-\infty}^{\infty} Q(x) \frac{Q(x)}{P(x)} dx.$$

Also known as the relative entropy*, this function satisfies $D_{KL}(Q||P) \geq 0$ with equality only if $P = Q$. The Kullback-Leibler divergence is an imperfect analog of the difference between two distributions, with $D_{KL}(Q||P) \neq D_{KL}(P||Q)$ in general.*

The Kullback-Leibler divergence provides a scalar-valued measure of the accuracy of the approximating distribution that approaches zero as Q approaches P. Indeed, it can be shown that the energy function for variational methods in statistical physics is equal to the relative entropy up to some additive constant.[8] Thus, we write the Kullback-Leibler divergence of the approximate distribution $Q(\boldsymbol{\pi};\boldsymbol{\psi})$ from the target distribution $P(\boldsymbol{\pi}|\boldsymbol{x},\boldsymbol{H})$.

$$D_{KL}\big(Q(\boldsymbol{\pi};\boldsymbol{\psi})||P(\boldsymbol{\pi}|\boldsymbol{x},\boldsymbol{\Upsilon})\big) = \int_{-\infty}^{\infty} Q(\boldsymbol{\pi};\boldsymbol{\psi})\ln\frac{Q(\boldsymbol{\pi};\boldsymbol{\psi})}{P(\boldsymbol{\pi}|\boldsymbol{x},\boldsymbol{\Upsilon})}\,d^k\theta \tag{5.6}$$

$$= \int_{-\infty}^{\infty} Q(\boldsymbol{\theta};\boldsymbol{\psi})\ln\frac{Q(\boldsymbol{\theta};\boldsymbol{\psi})}{P(\boldsymbol{x},\boldsymbol{\pi}|\boldsymbol{\Upsilon})}\,d^k\theta \tag{5.7}$$

$$- \int_{-\infty}^{\infty} Q(\boldsymbol{\theta};\boldsymbol{\psi})\ln P(\boldsymbol{x}|\boldsymbol{\Upsilon})d^k\theta$$

$$= \int_{-\infty}^{\infty} Q(\boldsymbol{\theta};\boldsymbol{\psi})\ln\frac{Q(\boldsymbol{\theta};\boldsymbol{\psi})}{P(\boldsymbol{x},\boldsymbol{\pi}|\boldsymbol{\Upsilon})}\,d^k\theta + \ln\frac{1}{P(X|H)}. \tag{5.8}$$

The term in the denominator in equation (5.6) is the called the joint likelihood function and is the product of the likelihood function and the prior probability distribution function. Dropping the constant entropy term from (5.6) and expanding about the ratio in the logarithm yields a $\boldsymbol{\pi}$-dependent entropy term and an expectation over $\boldsymbol{\theta}$ of the log joint likelihood function. We take this expression as the objective function $F(\boldsymbol{\theta})$ of the variational Bayesian inference procedure, this is also called the free energy function.[9]

$$F(\boldsymbol{\pi}) = -(\mathbb{H}\big[Q(\boldsymbol{\pi};\boldsymbol{\psi})] + \mathbb{E}_Q[\ln P(\boldsymbol{x},\boldsymbol{\pi}|\boldsymbol{\Upsilon})]\big) \tag{5.7}$$

Note that for a uniform prior distribution $F(\boldsymbol{\pi})$ reduces to the log-likelihood function given in chapter 2. Thus, variational Bayesian inference is a natural generalization of maximum likelihood estimation to more general probabilistic models. To minimize the objective $F(\boldsymbol{\pi})$, we

seek to maximize the sum inside the parentheses in equation (5.7). As with nonlinear least squares, we can apply line search methods using the gradient of the objective function

$$\nabla_{\boldsymbol{\psi}} F(\boldsymbol{\pi}) = \nabla_{\boldsymbol{\psi}} \mathbb{H}[Q(\boldsymbol{\pi}; \boldsymbol{\psi})] + \nabla_{\boldsymbol{\psi}} \mathbb{E}_Q[\ln P(\boldsymbol{x}, \boldsymbol{\pi} | \boldsymbol{\Upsilon})]. \tag{5.8}$$

A source of complexity in the implementation of optimization algorithms using equation (5.8) is the presence of intractable expectation terms in the second term on the right-hand side of the equation. In such cases a stochastic search vector must be constructed using Monte Carlo sampling. This will turn out to be the case in the TPD fitting problem but before we address this in sections 5 and 6, we will demonstrate the technique with Raman spectral fitting

5.4 Probabilistic Raman Fitting

Raman spectra provide bond vibrational data via inelastic Raman scattering processes. These processes are not surface sensitive. However, porous carbide derived carbons are amorphous porous materials with such large specific surface areas that they can be considered to have no bulk domain.[10]

In this study, carbide derived carbons were synthesized by exposing titanium carbide to chlorine gas at elevated temperatures. The gas etched the titanium carbide to produce titanium chloride gas, leaving microporous amorphous carbon material behind. The specific surface area of the material was measured by our collaborators to be roughly 3000 m^2/g but the distribution of functional groups within the material was unknown. Given the stoichiometry of the synthesis reaction it was reasonable to assume that the material contained isolated remnant domains of unreacted titanium carbide, and some concentration of alkyl halides, alkane, alkene, and alkyne groups, as well as aromatics. Carbonyl and alcohol groups were also expected to be present due

to post-synthesis treatments with sodium hydroxide. The sorption properties of the material are heavily dependent on the distribution of functional groups in the material.

The chemical functionalities in synthesized samples were studied using X-ray photoelectron spectroscopy (XPS). These results yielded hypothetical concentrations of various functional groups, but the features were poorly resolved due to the wide range of possibilities. To refine this estimate, Raman spectra of the samples were collected with a Bruker Senterra Raman microscope.

The goal of this work was to use the information obtained from XPS analysis as well as the stoichiometry of the synthesis reaction to provide a rational fit to the Raman signal. As can be seen in figure 1, the Raman signal has some structure, but it is obscured by heterogeneous broadening that results from the amorphous structure of the CDC. Given the extent of this broadening, we can conclude that the Raman signal is dominated by a Gaussian line-shape and proceed to fit the peaks without attempting to deconvolute the Lorentzian contribution that results from excited state lifetime uncertainty due to quantum operator non-commutation. Therefore, the overall model function f is a mixture of Gaussian line shapes in which each component peak i has a corresponding position p_i, broadening b_i, and intensity η_i parameter.

$$f(\nu) = \sum_{i=1}^{n} \frac{\eta_i}{\sqrt{2\pi b_i}} e^{-\frac{(\nu - p_i)^2}{b_i^2}} \tag{5.9}$$

Each parameter p_i, b_i, and η_i in turn has a set of hyperparameters associated with the prior distributions and approximate posterior distributions Q_i. Each parameter is modeled as a Gaussian normal distribution with mean μ and variance σ^2. The prior distributions reflect initial beliefs resulting from XPS analysis that was performed by a collaborating group. Tables 5.1 and 5.2 give the mean values of the prior Gaussian Normal distributions for untreated and treated

samples respectively. Standard deviations were chosen to be 5 wavenumbers for the position and broadening priors and 5 for the intensity priors. Variational Bayesian inference was run for 5000 iterations. The resulting curve fits are shown in Figure 5.1. The posterior hyperparameters are listed in Tables 5.3 and 5.4.

Table 5.1 Prior distribution parameters for CDC sample without NaOH treatment

Mean Position Prior (cm^{-1})	Mean Broadening Prior (cm^{-1})	Mean Intensity Prior
250	100	50.0
355	100	70.0
600	100	25.0
975	100	25.0
1150	100	2.70
1190	100	6.30
1249	100	2.70
1275	100	12.5
1355	100	100.0
1495	100	20.0
1565	100	100.0
1700	100	56.35
2450	100	90.0
2800	100	90.0

Table 5.2 Prior distribution parameters for CDC sample with NaOH treatment

Mean Position Prior (cm^{-1})	Mean Broadening Prior (cm^{-1})	Mean Intensity Prior
600	100	27
975	100	50
1150	100	15
1190	100	63
1249	100	4.38
1275	100	20
1355	100	100
1395	100	40
1400	100	20
1565	100	100
1700	100	24
2650	40	30
2800	100	10

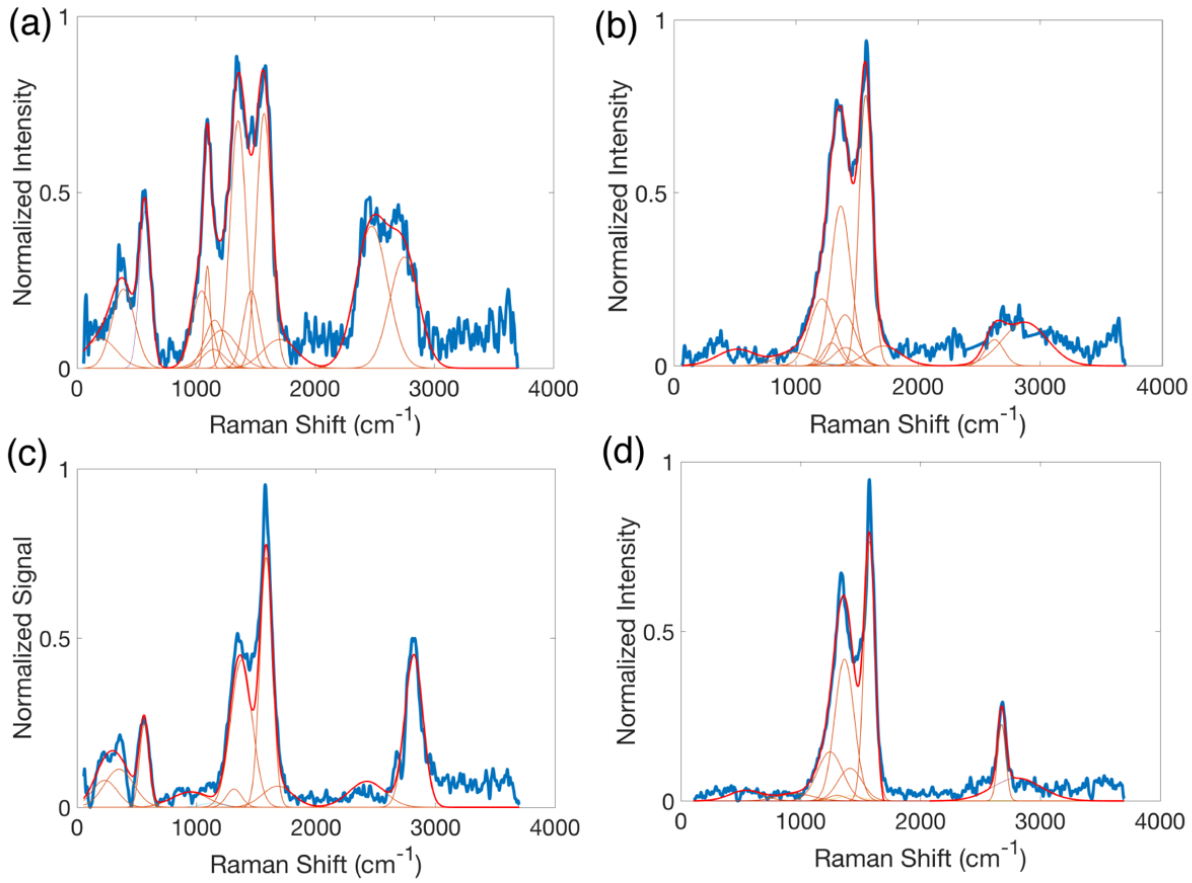

Figure 5.1 Raman spectra with Gaussian fits by variational Bayesian inference. Spectra (a) and (c) were recorded from samples without exposure to sodium hydroxide while spectra (b) and (d) were measured from exposed samples. Distributions of parameters for spectra (a) and (b) are given in tables 5.3 and 5.4 respectively.

Table 5.3 Posterior Distribution Parameters for untreated sample

Intensity Mean	Intensity Standard Deviation	Broadening Mean (cm^{-1})	Broadening Standard Deviation (cm^{-1})	Position Mean (cm^{-1})	Position Standard Deviation (cm^{-1})
28.3	0.03	134.0	0.11	196.6	0.44
53.4	0.03	94.9	0.04	389.2	0.05
53.1	0.01	47.4	0.04	571.5	0.01
44.9	0.03	81.7	0.02	1047.02	0.02
18.7	0.14	25.7	0.01	1094.45	0.01
12.3	0.15	92.1	0.03	1146.72	0.06
29.4	0.001	85.9	0.04	1155.73	0.07
34.7	0.04	128.5	0.06	1213.44	0.09
117.9	0.02	66.9	0.01	1352.6	0.01
36.5	0.03	66.5	0.05	1462.87	0.04
114.0	0.01	62.8	0.01	1570.16	0.01
29.1	0.024	141.5	0.01	1701.96	1.50
135.4	0.05	133.8	0.02	2473.41	0.01
97.1	0.015	122.7	0.04	2747.65	0.01

Table 5.4 Posterior Distribution Parameters for NaOH treated sample

Intensity Mean	Intensity Standard Deviation	Broadening Mean (cm^{-1})	Broadening Standard Deviation (cm^{-1})	Position Mean (cm^{-1})	Position Standard Deviation (cm^{-1})
19.3	0.02	160.9	0.06	519.4	0.3
13.4	0.01	137.0	0.02	977.3	0.1
1.0	0.004	108.2	1.2	1165.8	18.2
48.9	0.01	100.8	0.03	1212.2	0.02
1.3	0.005	110.0	0.60	1252.5	3.16
11.3	0.03	68.0	0.20	1293.4	0.12
96.0	0.02	82.9	0.01	1367.0	0.02
33.5	0.02	90.85	0.07	1402.2	0.05
12.6	0.01	95.5	0.10	1406.8	0.20
106.2	0.02	54.17	0.01	1571.5	0.007
20.7	0.02	143.8	0.14	1714.4	1.125
14.6	0.01	77.2	0.08	2625.9	0.11
57.9	0.01	183.8	0.03	2875.4	0.08

The posterior distributions in tables 5.3 and 5.4 can be used to construct posterior intervals. Posterior intervals are analogous to confidence intervals in the frequentist setting. The result of the inference procedure is that given the prior estimates of the parameters and the Raman data, very narrow estimates for the posterior parameter values were constructed. Note that in many cases the intensity of peak not present in the data was sent to zero.

There are a number of improvements that could be made to this analysis. The first is to replace the normal models with more appropriate distributions. The position term can be assumed under the central limit theorem to be normally distributed given that it's the mean of the sum of a large number of random variables, each corresponding to a single photon scattering process. However, there is no reason to believe that the intensity or the broadening terms should follow this distribution. Indeed, the broadening term is the variance in the Gaussian distribution for which the position is the mean and should be expected to be chi-squared distributed. The distribution of the intensity parameter is less clear because it relates to both the concentration of the associated bond as well as the scattering probability of its vibrational mode. Given that the parameter must be non-negative and that the majority of its probability density should be localized about its mean, a non-central chi-squared distribution may suffice. Further improvements would involve using multivariate distributions to model collections of parameters in order to encode correlations between them. At the time this analysis was conducted, Google's Edward library for probabilistic models supported such improvements but its limited documentation restricted their implementation.

5.5 Stochastic Search for Intractable Expectation Gradients

The Edward library is useful for rapid prototyping when the model function can be analytically specified. However, it does not currently support sequentially defined model functions and therefore numerical approximations of solutions to differential equations. This motivated the development of software in C++ to couple variational inference with low-latency ODE integration using the strategy discussed in chapter 2. This section discusses an implementation of variational inference originally developed by the machine learning community and published in 2012.[9] It has been tailored to the specific requirements of numerically integrated ODE model functions.

Equation 5.8 is the sum of two terms, the gradient of the Shannon entropy of the approximate posterior and the gradient of the expectation of the log joint likelihood under the approximate posterior. If we assume that the approximate posterior can be divided into one or more factors q_i and that the join likelihood can be factored according to the chain rule of probability theory into components $e^{f_j(\boldsymbol{\pi})}$ such that

$$Q(\boldsymbol{\pi}|\boldsymbol{\psi}) = \prod_i q_i \tag{5.10}$$

and

$$P(\boldsymbol{x}, \boldsymbol{\pi}|\boldsymbol{\Upsilon}) = \prod_j e^{f_j(\boldsymbol{\pi})} \tag{5.11}$$

then 5.8 can be rewritten in terms of sums these factors in log space and applying the linearity of the gradient and the expected value.

$$\nabla_{\boldsymbol{\psi}} F(\boldsymbol{\pi}) = \sum_i \nabla_{\boldsymbol{\psi}} \mathbb{H}[q_i(\boldsymbol{\pi}|\boldsymbol{\psi})] + \sum_j \nabla_{\boldsymbol{\psi}} \mathbb{E}_Q\big[f_j(\boldsymbol{\pi})\big]. \tag{5.12}$$

In this way, the log joint likelihood function can be separated into the sum of the log likelihood function and the log priors. Now consider a joint log likelihood component f_k such that $\mathbb{E}_Q[f_k]$ is

intractable. In other words, the improper multiple integral in equation 5.4 can't be evaluated analytically.

$$\mathbb{E}_Q[f_k] = \int_{-\infty}^{\infty} f_k(\boldsymbol{\pi}) Q(\boldsymbol{\pi}|\boldsymbol{\psi}) d\boldsymbol{\pi} \tag{5.13}$$

In such a case, we may invoke the following relationships.

$$\nabla_{\boldsymbol{\psi}} \mathbb{E}_Q[f_k] = \nabla_{\boldsymbol{\psi}} \int_{-\infty}^{\infty} f_k(\boldsymbol{\pi}) Q(\boldsymbol{\pi}|\boldsymbol{\psi}) d\boldsymbol{\pi} \tag{5.14}$$

$$= \int_{-\infty}^{\infty} f_k(\boldsymbol{\pi}) \nabla_{\boldsymbol{\psi}} Q(\boldsymbol{\pi}|\boldsymbol{\psi}) d\boldsymbol{\pi} \tag{5.15}$$

$$= \int_{-\infty}^{\infty} f_k(\boldsymbol{\pi}) Q(\boldsymbol{\pi}|\boldsymbol{\psi}) \nabla_{\boldsymbol{\psi}} \ln Q(\boldsymbol{\pi}|\boldsymbol{\psi}) \, d\boldsymbol{\pi} \tag{5.16}$$

$$= \mathbb{E}_Q\left[f_k(\boldsymbol{\pi}) \nabla_{\boldsymbol{\psi}} \ln Q(\boldsymbol{\pi}|\boldsymbol{\psi})\right] \tag{5.17}$$

Above, (5.14) is the definition of the expectation of a continuous distribution, (5.15) applies the fact that $f_k(\boldsymbol{\pi})$ is not a function of any element of $\boldsymbol{\psi}$, and (5.16) uses the identity of exponential distributions that $\nabla_{\boldsymbol{\psi}} Q(\boldsymbol{\pi}|\boldsymbol{\psi}) = Q(\boldsymbol{\pi}|\boldsymbol{\psi}) \nabla_{\boldsymbol{\psi}} \ln Q(\boldsymbol{\pi}|\boldsymbol{\psi})$. The result, (5.17), is that the gradient of the expectation is equal to the expectation of the intractable log probability multiplied by the gradient of the log approximate distribution. This expectation can be approximated via a Monte Carlo sampling routine that involves drawing S independent samples $\boldsymbol{\pi}_s$ from $Q(\boldsymbol{\pi}|\boldsymbol{\psi})$ and computing the average.

$$\mathbb{E}_Q\left[f_k \nabla_{\boldsymbol{\psi}} \ln Q(\boldsymbol{\pi}|\boldsymbol{\psi})\right] \approx \frac{1}{S} \sum_{s=1}^{S} f_k(\boldsymbol{\pi}_s) \nabla_{\boldsymbol{\psi}} \ln Q(\boldsymbol{\pi}_s|\boldsymbol{\psi}) \tag{5.18}$$

Therefore, the full gradient can be approximated with equation 5.10.

$$\nabla_{\boldsymbol{\psi}} F(\boldsymbol{\pi}) \approx \sum_{i} \nabla_{\boldsymbol{\psi}} \mathbb{H}[q_i(\boldsymbol{\pi}|\boldsymbol{\psi})] + \sum_{j \neq k} \nabla_{\boldsymbol{\psi}} \mathbb{E}_Q[f_j(\boldsymbol{\pi})] + \frac{1}{S} \sum_{s=1}^{S} f_k(\boldsymbol{\pi}_s) \nabla_{\boldsymbol{\psi}} \ln Q(\boldsymbol{\pi}_s|\boldsymbol{\psi}) \tag{5.19}$$

In the next section it will be shown that the expectation over the log likelihood function of the TPD signal model is intractable.

5.6 Probabilistic TPD Decomposition

We begin our development of probabilistic decomposition of TPD signals with a discussion of the appropriate distributions of each parameter. We limit our discussion to the kinetically limited model introduced in chapter 2. Recall that for a model of n discrete adsorption sites, we define parameter vectors $\boldsymbol{E_a} = (E_{a_1} \quad E_{a_2} \quad \cdots \quad E_{a_n})^T$ and $\boldsymbol{\theta_0} = (\theta_{0_1} \quad \theta_{0_2} \quad \cdots \quad \theta_{0_n})^T$ where E_{a_i} and θ_{0_i} represent the activation energy and fractional site coverage of site i respectively. We also define a fixed frequency factor vector $\boldsymbol{\nu_{n\times 1}}$, typically with each entry equal to 10^{13} Hz. We also introduce a parameter to characterize the variance of the data about the deterministic model function. To distinguish between variance hyperparameters that will be defined later, we introduce the precision $\tau = 1/\sigma^2$ that is often used in Bayesian statistics. The nonlinear deterministic model function that will appear as a component of the likelihood function is the normalized signal $\bar{s}(t,\ \boldsymbol{E_a},\ \boldsymbol{\theta_0})$ function given in equation 5.20, in which T_i is the initial temperature, t is time, and α is the ramp rate.

$$\bar{s}(t,\ \boldsymbol{E_a},\ \boldsymbol{\theta_0}) = \frac{1}{z} \sum_{i=1}^{n} \theta\left(\theta_{0_i}, E_{a_i}, t\right) \nu_i e^{\frac{-E_{a_i}}{(T_i + \alpha t)}} \tag{5.20}$$

The normalization constant z is computed by 5.21, where T_i and T_f are the initial and final temperatures respectively and T is the temperature at time t.

$$z = \int_{T_i}^{T_f} \frac{d\theta}{dt} dT \tag{5.21}$$

This normalization is performed to allow comparison between samples when the surface area is unknown, as is often the case.

Given that each E_{a_i} can be interpreted as the average bond enthalpy of adsorbates attached to site i, it is normally distributed by the central limit theorem. Therefore, we can model the joint posterior distribution of $\boldsymbol{E_a}$ as multivariate Gaussian normal with position vector $\boldsymbol{\mu}$ and covariance matrix Σ. The conjugate priors are distributions whose posteriors have the same functional form. The normal distribution is the conjugate prior of mean values, which we have established the activation energy to be. Therefore, we will model the prior over $\boldsymbol{E_a}$ as Gaussian normal with position vector μ_0 and covariance matrix Σ.

Similarly, we know that the precision parameter τ is gamma distributed with prior hyperparameters α_0 and β_0 and posterior hyperparameters α and β. The gamma distribution is a strictly positive exponential distribution with the density function given by equation (5.22). The function $\Gamma(\alpha)$ is the gamma function, the continuous generalization of the factorial operation. The parameters α and β are referred to as the shape and rate parameters respectively.

$$\text{Gamma}(\tau|\alpha,\beta) = \frac{\beta^{\alpha}}{\Gamma(\alpha)} \tau^{\alpha-1} e^{-\beta\tau} \tag{5.22}$$

The distribution of the fractional site coverages is interesting given the constraints that the elements of $\boldsymbol{\theta_0}$ must be positive and sum to one. The sites themselves can be thought of as categories and the fractional coverage as a categorical distribution. Thus, the natural choice of prior is the Dirichlet distribution. The elements of the parameter vector $\boldsymbol{a} = (a_1 \quad a_2 \quad \cdots \quad a_n)^T$

are called concentration parameters and are strictly greater than zero. The probability density function of the Dirichlet distribution is given in equation 5.23. Note that the sum over the parameter vector is denoted by the L1 norm notation $|\cdot|$. The hyperparameter vector of the prior distribution of $\boldsymbol{\theta_0}$ is denoted by $\boldsymbol{a_0}$ while that of the posterior is denoted $\boldsymbol{a}$.

$$\mathrm{Dir}(\boldsymbol{\theta_0}|\boldsymbol{a}) = \frac{\Gamma(|\boldsymbol{a}|)}{\prod_{i=1}^{n} a_i} \prod_{i=1}^{n} \theta_i^{a_i - 1} \tag{5.23}$$

As with the other distributions, the hyperparameter vector of the prior distribution of $\boldsymbol{\theta_0}$ is denoted by $\boldsymbol{a_0}$ while that of the posterior is denoted $\boldsymbol{a}$.

The approximate distribution Q is defined to be the product of the approximate distributions over the activation energies, fractional coverages, and the precision. Returning to the notation used previously, we define the parameter set $\boldsymbol{\pi} = \{\boldsymbol{E_a}, \boldsymbol{\theta_0}, \tau\}$, the prior hyperparameters $\boldsymbol{\Upsilon} = \{\boldsymbol{\mu_0}, \Sigma_0, \alpha_0, \beta_o, \boldsymbol{a}_0\}$, and the variational hyperparameters $\boldsymbol{\psi} = \{\boldsymbol{\mu}, \Sigma, \alpha, \beta, \boldsymbol{a}\}$.

$$\mathrm{Q}(\boldsymbol{\pi}|\boldsymbol{\psi}) = q_{E_a}(\boldsymbol{E_a}|\boldsymbol{\mu}, \Sigma) q_\tau(\tau|\alpha, \beta) q_{\theta_0}(\boldsymbol{\theta_0}|\boldsymbol{a}) \tag{5.24}$$

We can therefore write the gradient of the entropy of the approximate posterior as the sum of the gradients of the entropies of the individual factors as in equation (5.12). Distributions in the exponential family have closed form entropies, given in equations (5.25-5.26). Note that $\psi^0(x)$ is the digamma function, which is equal to the first derivative of the log of the gamma function.

$$\mathbb{H}\left[q_{E_a}(\boldsymbol{E_a}|\boldsymbol{\mu}, \Sigma)\right] = \frac{1}{2} \ln 2\pi e|\Sigma| \tag{5.25}$$

$$\mathbb{H}[q_\tau(\tau|\alpha, \beta)] = \alpha - \ln \beta + \ln \Gamma(\alpha) + (1 - \alpha)\psi^0(\alpha) \tag{5.26}$$

$$\mathbb{H}\left[q_{\theta_0}(\boldsymbol{\theta_0}|\boldsymbol{a})\right] = \ln \prod_{j=1}^{n} \Gamma(a_j) - \ln \Gamma(|\boldsymbol{a}|) - (n - |\boldsymbol{a}|)\psi^0(|\boldsymbol{a}|) \\ - \sum_{j=1}^{n} (a_j - 1)\psi^0(a_j) \tag{5.27}$$

The gradients of each of these functions can be derived using tensor analysis or matrix calculus. Matrix calculus was historically developed to deal with multivariate statistics problems and is used here. Table 6.1 gives the partial derivatives of each entropy component with respect to each hyperparameter. We denote $\mathbf{0}_{n\times 1}$ and $\mathbf{1}_{n\times 1}$ as the n dimensional zero and one vectors respectively (that is, all elements are either zero or one accordingly). Analogously, $\mathbf{0}_{n\times n}$ is the zero square matrix in n dimensions. The first polygamma function, which is the second derivative of the log gamma function, is denoted by $\psi^{(1)}$ and the element-wise vector product is indicated by $*$.

Table 5.5 Partial derivatives of the entropy components

Partial Operator	$\mathbb{H}\left[q_{E_a}(\boldsymbol{E_a}\|\boldsymbol{\mu},\Sigma)\right]$	$\mathbb{H}[q_\tau(\tau\|\alpha,\beta)]$	$\mathbb{H}\left[q_{\theta_0}(\boldsymbol{\theta_0}\|\boldsymbol{a})\right]$
$\frac{\partial}{\partial \boldsymbol{\mu}}$	$\mathbf{0}_{n\times 1}$	$\mathbf{0}_{n\times 1}$	$\mathbf{0}_{n\times 1}$
$\frac{\partial}{\partial \Sigma}$	$\frac{1}{2}\Sigma^{-1}$	$\mathbf{0}_{n\times n}$	$\mathbf{0}_{n\times n}$
$\frac{\partial}{\partial \alpha}$	0	$1+(1-\alpha)\psi^{(1)}(\alpha)$	0
$\frac{\partial}{\partial \beta}$	0	$-\frac{1}{\beta}$	0
$\frac{\partial}{\partial \boldsymbol{a}}$	$\mathbf{0}_{n\times 1}$	$\mathbf{0}_{n\times 1}$	$\psi^{(0)}(\boldsymbol{a})-\psi^{(0)}(\|\boldsymbol{a}\|)\mathbf{1}_{n\times 1}$ $-(n-\|\boldsymbol{a}\|)\psi^{(1)}(\|\boldsymbol{a}\|)\mathbf{1}_{n\times 1}$ $-(\boldsymbol{a}-\mathbf{1}_{n\times 1})*\psi^{(1)}(\boldsymbol{a})$

The prior takes a similar structure to the approximate posterior and the joint likelihood can be factored as follows.

$$P(\boldsymbol{x}, \boldsymbol{\pi}|\boldsymbol{\Upsilon}) = P(\boldsymbol{x}|\boldsymbol{\pi}, \boldsymbol{\Upsilon})P(\boldsymbol{\pi}|\boldsymbol{\Upsilon}) \tag{5.28}$$

$$= P(\boldsymbol{x}|\boldsymbol{\pi})P(\boldsymbol{E_a}|\boldsymbol{\mu_0}, \Sigma)P(\tau|\alpha_0, \beta_0)P(\boldsymbol{\theta_0}|\boldsymbol{a}) \tag{5.29}$$

The log prior is separated into the sum of the logs of the factors in equation (5.29) and the gradient of the expectation of the log prior is subsequently distributed across the factors. The result is equation (5.30). We will examine each of the terms on the right-hand side to determine which expectations are tractable.

$$\nabla_{\boldsymbol{\psi}}\mathbb{E}_Q[\ln P(\boldsymbol{x}, \boldsymbol{\pi}|\boldsymbol{\Upsilon})] \tag{5.30}$$

$$= \nabla_{\boldsymbol{\psi}}\mathbb{E}_Q[\ln P(\boldsymbol{x}|\boldsymbol{\pi})]$$

$$+ \nabla_{\boldsymbol{\psi}}\mathbb{E}_Q[\ln P(\boldsymbol{E_a}|\boldsymbol{\mu_0}, \Sigma)] + \nabla_{\boldsymbol{\psi}}\mathbb{E}_Q[\ln P(\tau|\alpha_0, \beta_0)]$$

$$+ \nabla_{\boldsymbol{\psi}}\mathbb{E}_Q[\ln P(\boldsymbol{\theta_0}|\boldsymbol{a}_0)]$$

Recall that the data are assumed to be normally distributed about the model function. This is equivalent to assuming that the residuals are normally distributed and should be satisfied if they are independent and identically distributed. Equations (5.31-35) show the derivation of the expected value of the log likelihood under Q in terms of the nonlinear model function. Let m denote the number of data points and s_i denote a normalized measured signal value.

$$\mathbb{E}_Q[\ln P(\boldsymbol{x}|\boldsymbol{\pi})] = \mathbb{E}_Q\left[\ln \prod_{i=1}^{m} P(x_i|\boldsymbol{\pi})\right] \tag{5.31}$$

$$= \mathbb{E}_Q\left[\ln \prod_{i=1}^{m} \sqrt{\frac{\tau}{2\pi}}\, e^{-\frac{\tau}{2}\left(s_i - \bar{s}(\boldsymbol{E_a}, \boldsymbol{\theta_0}, t_i)\right)^2}\right] \tag{5.32}$$

$$= \mathbb{E}_Q\left[\ln\left(\sqrt{\frac{\tau}{2\pi}}\right)^m e^{-\frac{\tau}{2}\sum_{i=1}^m \left(s_i - \bar{s}(\boldsymbol{E_a}, \boldsymbol{\theta_0}, t_i)\right)^2}\right] \tag{5.33}$$

$$= \mathbb{E}_Q\left[\frac{m}{2}(\ln\tau - \ln 2\pi) - \frac{\tau}{2}\sum_{i=1}^m \left(s_i - \bar{s}(\boldsymbol{E_a}, \boldsymbol{\theta_0}, t_i)\right)^2\right] \tag{5.34}$$

$$= \frac{m}{2}\left(\psi^{(0)}(\alpha) - \ln\beta - \ln 2\pi\right) \tag{5.35}$$

$$- \frac{\alpha}{2\beta}\mathbb{E}_{\{q_{E_a}, q_{\theta_0}\}}\sum_{i=1}^m \left(s_i - \bar{s}(\boldsymbol{E_a}, \boldsymbol{\theta_0}, t_i)\right)^2$$

The expectation over the summation in the third term on the right-hand side of equation (5.35) represents an intractable integral since $\bar{s}(\boldsymbol{E_a}, \boldsymbol{\theta_0}, t_i)$ cannot be written analytically in terms of $\boldsymbol{E_a}$ and $\boldsymbol{\theta_0}$. Therefore, a stochastic search vector will need to be constructed to approximate the gradient of this term. The other terms in the above can be differentiated with respect to the hyperparameters in $\boldsymbol{\psi}$ to show that, while q_τ need not be sampled to find the gradient components in the α and β directions, the approximate sum of squared residuals is needed**.**

$$\frac{\partial \mathbb{E}_Q[\ln P(\boldsymbol{x}|\boldsymbol{\pi})]}{\partial\alpha} = \frac{m}{2}\psi^{(1)}(\alpha) - \frac{1}{2\beta}\mathbb{E}_{\{q_{E_a}, q_{\theta_0}\}}\sum_{i=1}^m \left(s_i - \bar{s}(\boldsymbol{E_a}, \boldsymbol{\theta_0}, t_i)\right)^2 \tag{5.36}$$

$$\frac{\partial \mathbb{E}_Q[\ln P(\boldsymbol{x}|\boldsymbol{\pi})]}{\partial\beta} = \frac{\alpha}{2\beta^2}\mathbb{E}_{\{q_{E_a}, q_{\theta_0}\}}\sum_{i=1}^m \left(s_i - \bar{s}(\boldsymbol{E_a}, \boldsymbol{\theta_0}, t_i)\right)^2 \tag{5.37}$$

The gradient components of the log approximate distribution are given in equations (5.38-40).

$$\frac{\partial \ln Q}{\partial \boldsymbol{\mu}} = \Sigma^{-1}(\boldsymbol{E_a} - \boldsymbol{\mu}) \tag{5.38}$$

$$\frac{\partial \ln Q}{\partial \Sigma} = -\frac{1}{2}(\Sigma^{-1} - (\boldsymbol{E_a} - \boldsymbol{\mu})(\boldsymbol{E_a} - \boldsymbol{\mu})^T) \tag{5.39}$$

$$\frac{\partial \ln Q}{\partial \mathbf{a}} = \psi^{(0)}(|\boldsymbol{a}|)\mathbf{1}_{n\times 1} - \psi^{(0)}(\boldsymbol{a}) + \ln \boldsymbol{\theta_0} \tag{5.40}$$

The expectations of the log prior distribution factors over Q are given in equations (5.41-3).

$$\mathbb{E}_Q[\ln P(\boldsymbol{E_a}|\boldsymbol{\mu_0}, \Sigma)] \tag{5.41}$$

$$= -\frac{1}{2}\ln(2\pi)^n|\Sigma_0|$$

$$-\frac{1}{2}\left[Tr(\Sigma_0^{-1}\Sigma) + \boldsymbol{\mu^T}\Sigma_0^{-1}\boldsymbol{\mu} - 2\boldsymbol{\mu^T}\Sigma_0^{-1}\boldsymbol{\mu_0} + \boldsymbol{\mu_0^T}\Sigma_0^{-1}\boldsymbol{\mu_0}\right]$$

$$\mathbb{E}_Q[\ln P(\tau|\alpha_0, \beta_0)] = \alpha_0 \ln \beta_0 - \ln \Gamma(\alpha_0) + (\alpha_0 - 1)\left(\psi^{(0)}(\alpha) - \ln \beta\right) - \frac{\beta_0 \alpha}{\beta} \tag{5.42}$$

$$\mathbb{E}_Q[\ln P(\boldsymbol{\theta_0}|\boldsymbol{a}_0)] \tag{5.43}$$

$$= \ln \Gamma(|\boldsymbol{a_0}|) - \sum_{i=1}^{n} \ln \Gamma\left(a_{o_i}\right) + (\boldsymbol{\alpha_0} - \mathbf{1}_{n\times 1})^T \left(\psi^{(0)}(\boldsymbol{a})\right.$$

$$\left. - \psi^{(0)}(|\boldsymbol{a}|)\mathbf{1}_{n\times 1}\right)$$

The partial derivatives of the expected log priors are provided in Table 5.6.

Table 5.6 Partial derivatives of expected log priors

Partial Operator	$\mathbb{E}_Q[\ln P(\boldsymbol{E_a}\|\boldsymbol{\mu_0}, \Sigma_0)]$	$\mathbb{E}_Q[\ln P(\tau\|\alpha_0, \beta_0)]$	$\mathbb{E}_Q[\ln P(\boldsymbol{\theta_0}\|\boldsymbol{a}_0)]$
$\frac{\partial}{\partial \boldsymbol{\mu}}$	$\Sigma^{-1}(\boldsymbol{\mu_0} - \boldsymbol{\mu})$	$\mathbf{0}_{n\times 1}$	$\mathbf{0}_{n\times 1}$
$\frac{\partial}{\partial \Sigma}$	$-\frac{1}{2}\Sigma_0^{-1}$	$\mathbf{0}_{n\times n}$	$\mathbf{0}_{n\times n}$
$\frac{\partial}{\partial \alpha}$	0	$(\alpha_0 - 1)\left(\psi^{(1)}(\alpha)\right) - \frac{\beta_0}{\beta}$	0
$\frac{\partial}{\partial \beta}$	0	$-\frac{1}{\beta} + \frac{\beta_0 \alpha}{\beta^2}$	0
$\frac{\partial}{\partial \boldsymbol{a}}$	$\mathbf{0}_{n\times 1}$	$\mathbf{0}_{n\times 1}$	$(\boldsymbol{a_0} - \mathbf{1}_{n\times 1})$ $*\left(\psi^{(1)}(\boldsymbol{a})\right.$ $\left. - \psi^{(1)}(\|\boldsymbol{a}\|)\mathbf{1}_{n\times 1}\right)$

Thus, we have derived analytical forms or stochastic approximations for each component of the variational gradient. Figure 5.2 shows fits of synthetic data from a hypothetical sample with two different sites that are uniformly distributed across two activation energies: 50 kJ/mol and 55 kJ/mol. This figure shows the impact of changing the value of the $\boldsymbol{a}$ parameter vector. Both elements of the vector are equal in each fit, however the magnitude of the parameter increases from 10 in plot a to 25 in plot b and 50 in plot c. Note that the expected value of a given site concentration θ_i is given by

$$\mathbb{E}[\theta_i] = \frac{a_i}{\sum_{i=1}^{n} a_i}. \tag{5.44}$$

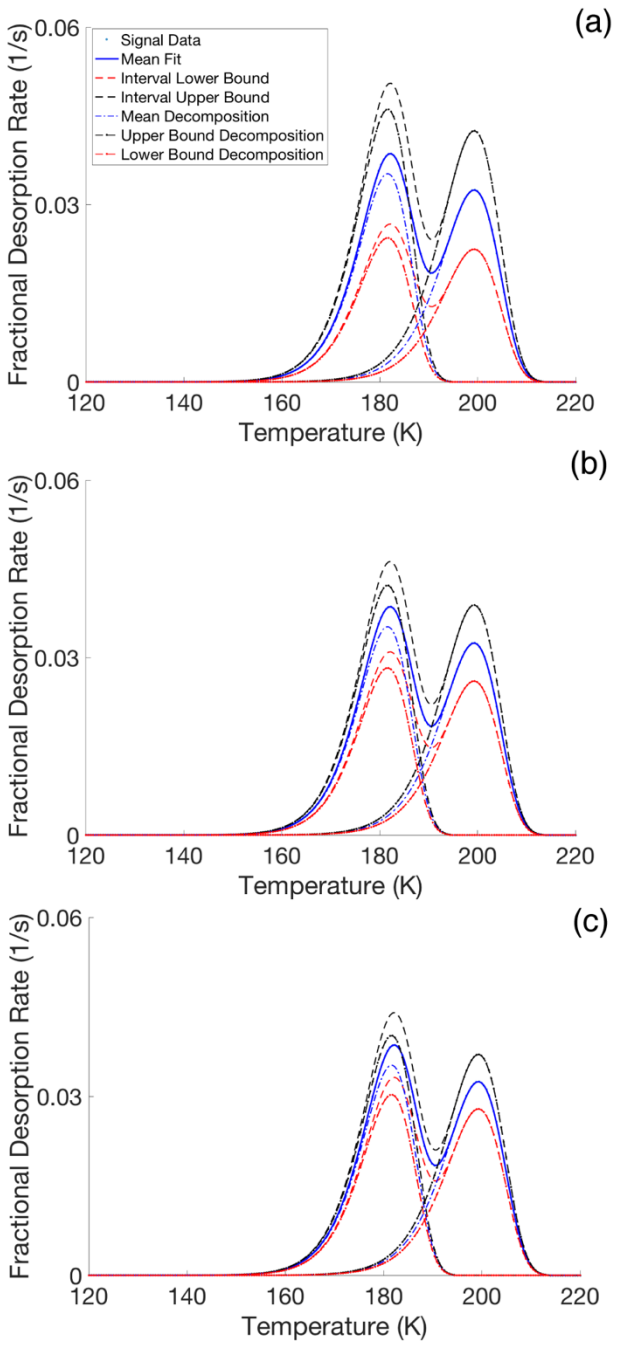

Figure 5.2 Plots of simulated data and fit proposals with varying Dirichlet concentration parameters: $\boldsymbol{a} = (\mathbf{10} \quad \mathbf{10})^{\boldsymbol{T}}$ in plot (a), $\boldsymbol{a} = (\mathbf{25} \quad \mathbf{25})^{\boldsymbol{T}}$ in plot (b), and $\boldsymbol{a} = (\mathbf{50} \quad \mathbf{50})^{\boldsymbol{T}}$ in plot

5.7 References

1. MacKay, D. J. C., *Information Theory, Inference & Learning Algorithms*; Cambridge University Press, 2002.
2. Hibbert, D. B.; Armstrong, N., An Introduction to Bayesian Methods for Analyzing Chemistry Data: Part II: A Review of Applications of Bayesian Methods in Chemistry. *Chemometrics and Intelligent Laboratory Systems* **2009**, *97*, 211-220.
3. Tran, D.; Kucukelbir, A.; Dieng, A. B.; Rudolph, M.; Liang, D.; Blei, D. M., Edward: A Library for Probabilistic Modeling, Inference, and Criticism. *arXiv preprint arXiv:1610.0987* **2016**.
4. Barrie, P. J., Analysis of Temperature Programmed Desorption (TPD) Data for the Characterisation of Catalysts Containing a Distribution of Adsorption Sites. *Phys. Chem. Chem. Phys.* **2008**, *10*, 1688-1696.
5. D G Truhlar, a.; Garrett, B. C., Variational Transition State Theory. *Annual Review of Physical Chemistry* **1984**, *35*, 159-189.
6. Refson, K.; Tulip, P. R.; Clark, S. J., Variational Density-Functional Perturbation Theory for Dielectrics and Lattice Dynamics. *Phys. Rev. B* **2006**, *73*, 155114.
7. E., S. C., A Mathematical Theory of Communication. *Bell System Technical Journal* **1948**, *27*, 379-423.
8. Jaynes, E. T., Information Theory and Statistical Mechanics. *Physical Review* **1957**, *106*, 620-630.
9. Paisley, J.; Blei, D. M.; Jordan, M. I., Variational Bayesian Inference with Stochastic Search. In *Proceedings of the 29th International Coference on International Conference on Machine Learning*, Omnipress: Edinburgh, Scotland, 2012; pp 1363-1370.
10. Moran, C.; M. Marti, R.; E. Hayes, S.; S. Walton, K., *Synthesis and Characterization of Aluminum Carbide-Derived Carbon with Residual Aluminum-Based Nanoparticles*, 2016; Vol. 114.

CHAPTER 6. CARBON DIOXIDE ADSORPTION SITE DISTRIBUTIONS ON COPPER BENZENEDICARBOXYLATE SURFACES

6.1. Introduction

Metal-organic frameworks (MOFs) are a class of crystalline microporous materials with high surface areas and flexible chemical functionality.[1-2] Active research in MOFs targets a wide range of applications, including biosensors, heterogeneous catalysis, and drug delivery.[3-6] Due to their transport properties and modular chemistry, MOFs have shown exceptional performance as active materials in gas separation membranes. In 2014, Rodenas *et al* demonstrated a diffusion-limited synthesis reaction for making metal-benzenedicarboxylate (MBDC) MOF nanosheets and showed that copper benzenedicarboxylate (CuBDC) nanosheets are highly selective for carbon dioxide over methane.[7] The nanosheet form of CuBDC was found to have a much higher selectivity for CO_2 than its three-dimensional bulk crystal analog but the mechanism of this effect is unknown. In this chapter, the variational Bayesian decomposition analysis introduced in chapter 5 will be applied to temperature programmed desorption (TPD) data to arrive at distributions of surface sites for copper benzenedicarboxylate nanosheets.

TPD signals from bulk CuBDC crystals were also recorded. The bulk crystal signals are dramatically obscured by internal diffusion, however qualitative analysis provides insight into the site distribution that is numerically extracted from the nanosheet TPD profiles.

6.2. Experimental

6.2.1 Synthesis

6.2.1.1 Bulk MOF Synthesis

Three dimensional CuBDC nanosheets were synthesized using the bulk-type procedure reported by Carson *et al*.[8] 1.05 g of copper (II) nitrate trihydrate and 0.720 g of terephthalic acid were dissolved in 87 mL N,N-dimethylformamide (DMF). This solution was refluxed at 100˚ C in a 250 mL round bottom flask for 24 hours while stirring. The crystalline product was recovered from the mixture by centrifugation at 6000 rpm for 10 minutes and washed 3 times with 20 mL of methanol. The product was allowed to soak in methanol for at least 3 hours between each wash to allow time for solvent replacement. A portion of the product was activated in a vacuum oven at 170˚ C for 48 hours. The activated sample was characterized by X-ray diffraction (XRD), scanning electron microscopy (SEM), and Brunauer-Emmett-Teller (BET) surface area measurement. The rest of the product was stored in methanol for use in TPD experiments.

6.2.1.2 Nanosheet MOF Synthesis

Two-dimensional MOF nanosheets were synthesized using a modified version of the diffusion mediated approach described in chapter three. Briefly, 300 mg of terephthalic acid were dissolved in a mixture of 20 mL DMF and 10 mL acetonitrile, which was then poured into a 100 mL beaker with a radius of 14 mm. A spacer layer of 10 mL DMF mixed with 10 mL acetonitrile was poured slowly into the 100 mL beaker to minimize mixing between the layers. 300 mg copper (II) nitrate trihydrate was dissolved in 10 mL DMF and 20 mL acetonitrile. The copper nitrate solution was poured slowly into the beaker, again to avoid mixing between the layers. The layered mixture was heated to 40˚ C for 24 hours. The crystalline product was recovered by centrifugation at 6000 rpm for 10 minutes. The product was washed three times with methanol, allowing at least three hours between washes to soak in methanol for solvent exchange. A

portion of this product was activated at 170˚ C for 48 hours in a vacuum oven and subsequently characterized by X-ray diffraction, SEM, and BET surface area analysis. The rest was stored in methanol prior to being loaded into the TPD chamber.

6.2.2 Characterization

XRD measurements were performed using a Panalytical X'pert Pro X-ray diffractometer with a copper X-ray source. XRD samples were prepared by drop coating a glass slide with MOF sample suspended in methanol and activating the coating by heating to 170 ˚C for 48 hours. BET surface area measurements were conducted with a Micrometrics Flowsorb III Surface Area Analyzer using nitrogen gas. Scanning electron micrographs were recorded using a Hitachi FE8230 Field Emission Scanning Electron Microscope with a landing potential of 700V.

6.2.3 Temperature Programmed Desorption

TPD measurements were carried out in a custom built ultra-high vacuum chamber with base pressure < 10^{-9} Torr. A gold sample holder was drop coated with MOF sample suspended in methanol. The coated sample holder was then activated in a vacuum oven at 170 ˚C for 48 hours. The sample was then mounted at the end of a Sumitomo 4 K cryostat equipped with a heater cartridge and thermocouple. The cryostat was inserted into the vacuum chamber in close proximity to a Hiden residual gas analyzer (RGA). The chamber was evacuated and baked at 70 ˚C for 24 hours to remove residual gases from the wall and adsorbed water from the MOF sample. After baking, the sample was cooled to 20 K and exposed to 10^{-8} Torr of 99.998% CO_2 for either 500, 1000, or 1500 seconds, corresponding to 5, 10, and 15 Langmuir (L) of surface exposure respectively. After the chamber pressure was allowed to return below 10^{-9} Torr, a

Lakeshore 336 cryogenic temperature controller and heater cartridge was used to heat the sample to 300 K at a rate of 2.5 K/min for the nanosheets and at rates of 2.5, 5, and 7.5 K/min for the bulk crystals. Relative pressure of carbon dioxide in the chamber was measured during heating using the RGA in faraday cup mode.

Rate and coverage procedures were reproduced between three and five times to ensure signal stability. Background measurements of the blank sample were also recorded for each rate and coverage procedure. Exposures were carried out well below the sublimation point of CO_2 to allow ice to build up on the sample and cryostat components. The sublimation signal was used to accurately measure the temperature ramp rate during each experiment.

6.2 Results and Discussion

6.2.1 Crystal Structure and Particle Morphology

Interpretation of the desorption profiles from nanosheet and bulk samples will rely on a consideration of their respective crystal orientations. Figure 6.1 shows graphical representations of prominent lattice planes relative to the pore structure as well as simulated and measured diffraction patterns. As seen previously, the XRD sample preparation by drop casting results in highly oriented nanosheet samples, which explains the dominance of the $(20\bar{1})$ peak at $2\theta = 17.8^{\circ}$.

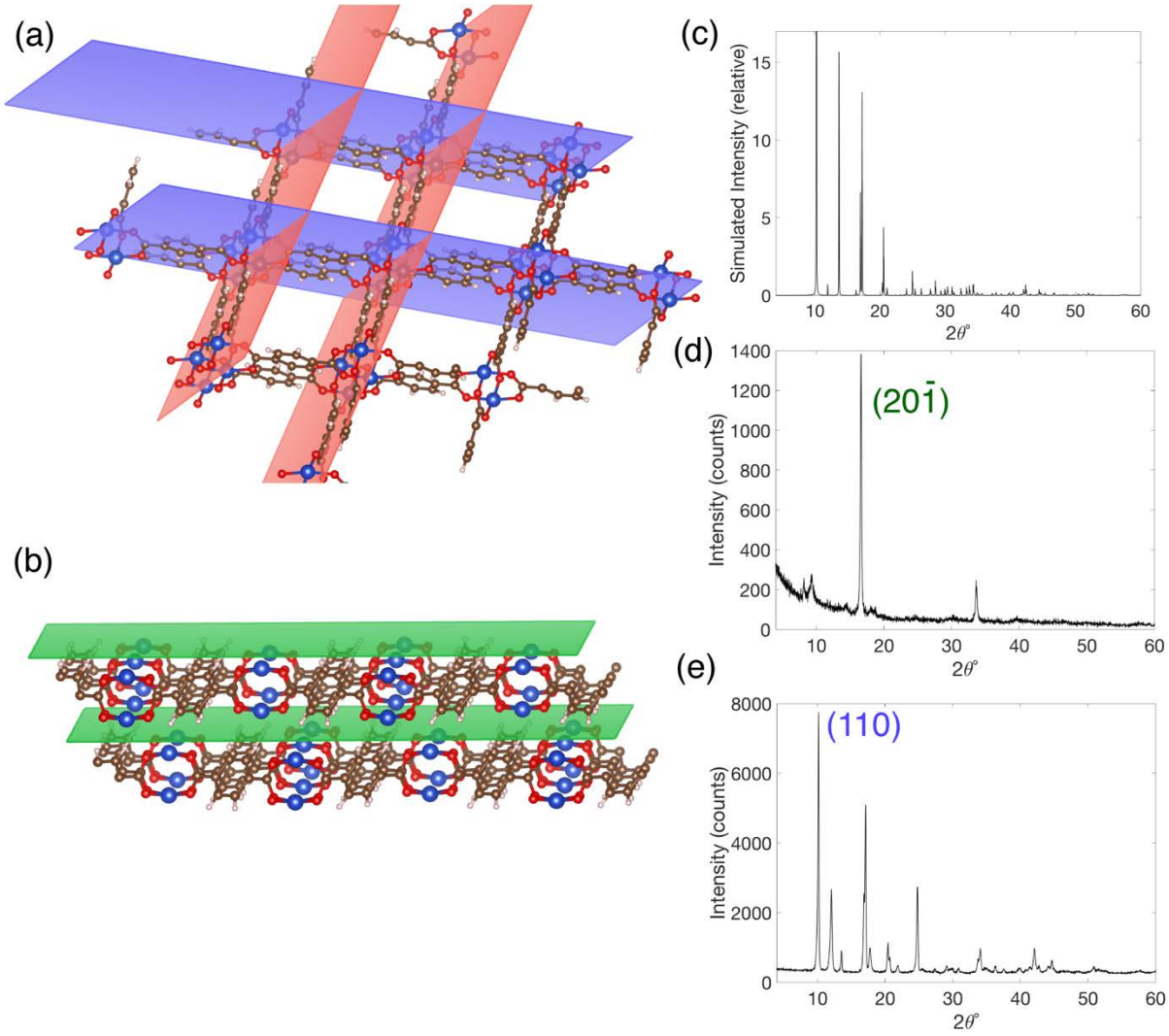

Figure 6.1 Graphical representations of prominent lattice planes in the CuBDC crystal structure. The (110) and $(\bar{1}10)$ planes are shown in blue and red respectively in graphic (a). Graphic (b) shows the $(20\bar{1})$ stacking plane. Plot (c) shows a simulated XRD pattern of CuBDC crystals while plots (d) and (e) show measured patterns from nanosheet and bulk samples respectively. Oxygen is shown in red, copper in blue, carbon in brown, and hydrogen in white.

The pores run normal to the plane of the nanosheets but the specific surface area of the nanosheet sample is relatively small at 51 m^2/g. Thus, it can be concluded that the pores are fairly shallow. The bulk sample, on the other hand, had a reasonably high specific surface area of 299 m^2/g. This is still less than half of the theoretical surface area of 850 m^2/g and is likely due to a mixture of causes including insufficient annealing as well as residual regions of trapped amides inside the pores. Activation of the material above 200 ˚C has been shown to yield specific surface areas approaching the theoretical value. However, such temperatures have been found to degrade nanosheet samples and may produce lattice defects. The activation procedure for both samples was carried out to the same specification as Rodenas *et al* to provide the best possible comparison.

Figure 6.2 shows SEM images of activated CuBDC samples. Many of the bulk crystals in image (b) are oriented such that the layers are stacked parallel to the electron beam and the material can be seen to be separated apart in this dimension. Thus, desorbed gases may diffuse between one-dimensional pore channels. For such a complicated diffusion mechanism, the simple mass transfer model introduced in chapter 3 is unlikely to be accurate.

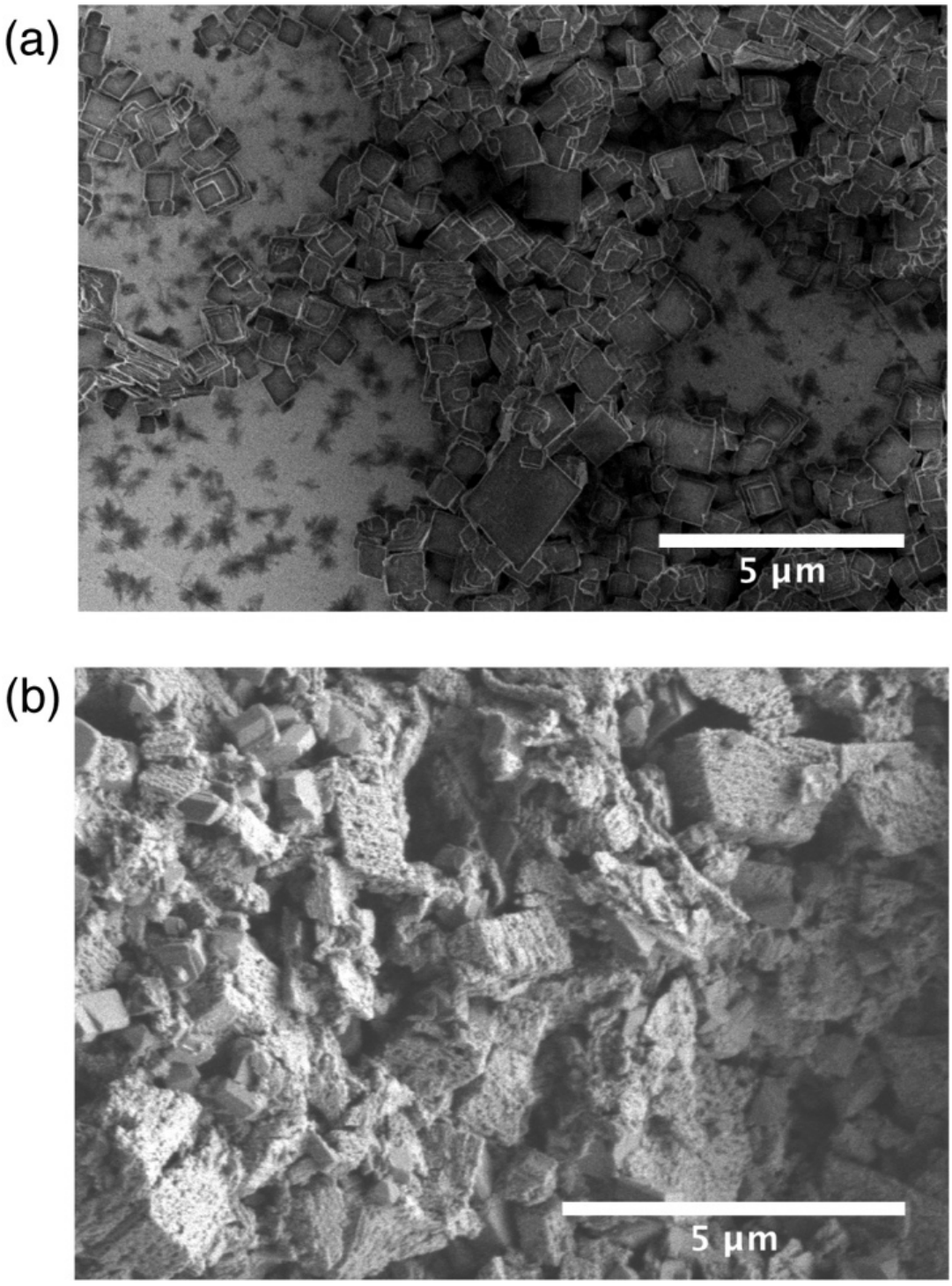

Figure 6.2 Scanning electron micrographs of activated CuBDC nanosheets (a) and bulk crystals (b).

6.2.2 Qualitative analysis of TPD Results

Figure 6.3 shows the baseline corrected TPD profile of CO_2 from bulk CuBDC. The left-hand side of the curve rises sharply because the signal was obscured by the CO_2 ice sublimation peak, which has been removed. As expected, the signal decays slowly after the peak at 94.05 K, indicating that internal diffusion processes are influencing the signal. The peak position doesn't change with the ramp rate, indicating that internal mass transfer is dominated by interactions between the gas and the pore walls rather than between gases. Figure 3b shows a very rough fit of the 7.5 K/min curve. The extracted enthalpy of desorption from bulk CuBDC was 26.0 kJ/mol. There may be higher energy sites such as defects that are otherwise obscured by the diffusion component. Note that TPD peaks at higher temperatures are much broader than at lower temperatures so even though some information was lost behind the ice peak, even this rough fit gives a good estimate for the enthalpy of desorption.

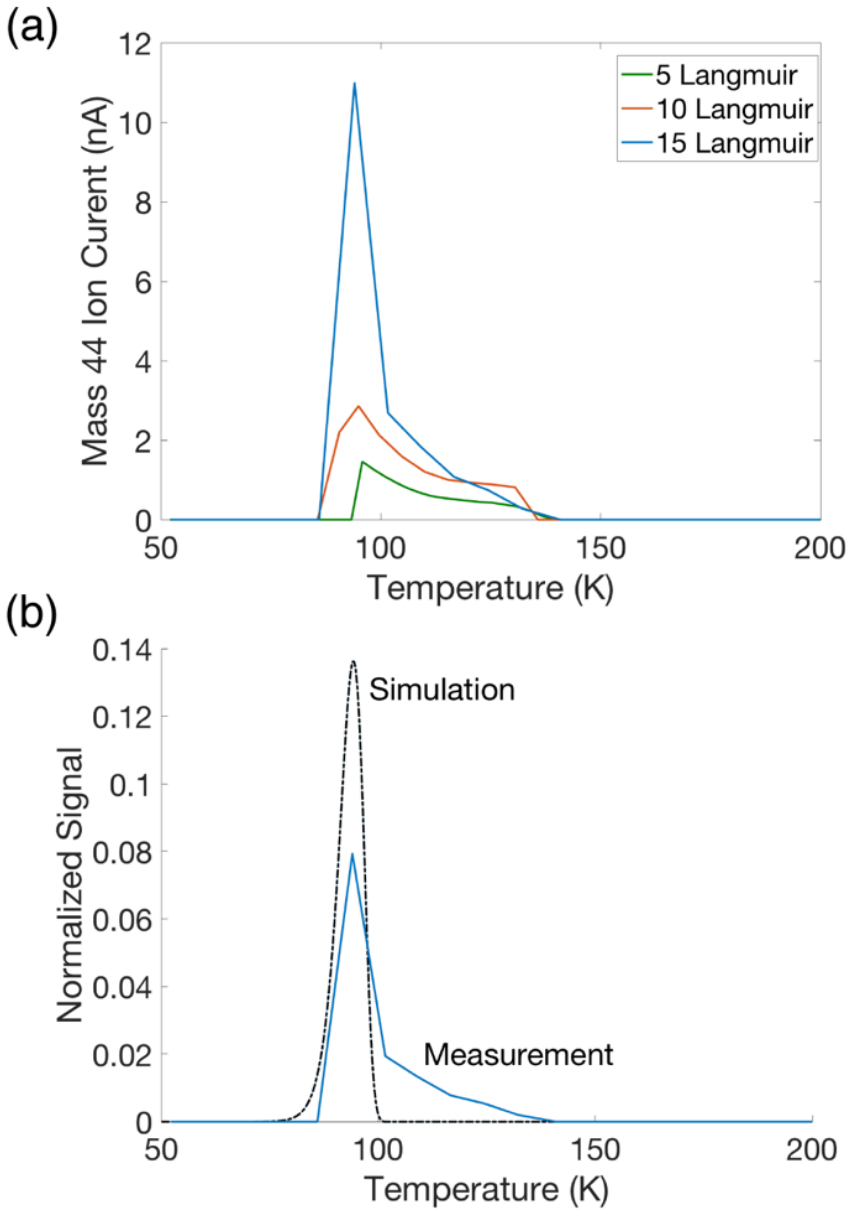

Figure 6.3 Background corrected TPD profiles of CO_2 from bulk CuBDC crystals at varying ramp rates (a). Plot of rough simulation fit of 7.5 K/min signal.

Figure 6.4 shows the background corrected CO_2 desorption profiles from nanosheet samples. These have much more structure than those from bulk crystals. Multiple peaks are present, and their intensity ratios vary based on the initial CO_2 exposure. The peak positions do not vary with exposure and we conclude that the process follows a first order rate law. This is to be expected in this temperature range. Parts of the curves were similarly cut off by the ice peak, however this is only a small fraction of the signal.

A few qualitative conclusions can be drawn from these data. The presence of two peaks means that there are at least two adsorption sites on CuBDC nanosheets and each makes up an appreciable fraction of the surface. The signals decay rapidly at temperatures above the peak, indicating negligible diffusion limitation to the desorption process. The first peak is centered at 110 K, which is 15.6 K higher than the bulk desorption peak. The second peak appears 22 K higher than the first at 132 K. These data are consistent with Rodenas *et al*'s results indicating that CuBDC nanosheets have higher affinity for CO_2 than does the bulk material. The lower energy peak is broad, which suggests that there may be three or more peaks overlapping one another. The distribution of site energies is needed before a structural mechanism for these relatively strong desorption enthalpies can be proposed.

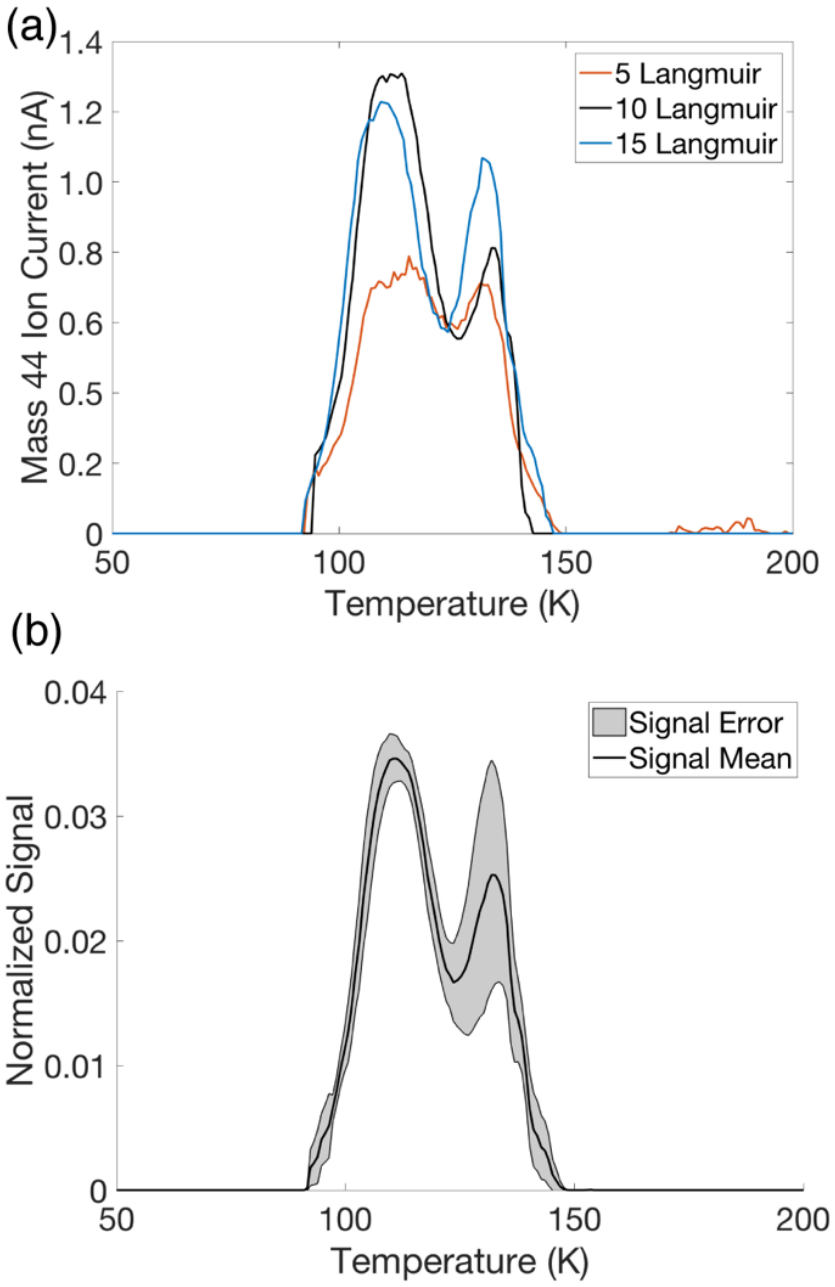

Figure 6.4 Sample TPD curves of CO_2 from CuBDC nanosheets at varying initial exposures (a). Mean TPD curve of over six samples with initial exposure of 10 Langmuir, point-wise standard deviation region shown in gray (b).

Figure 4b shows that there is significant uncertainty in the intensity of the second peak. This uncertainty presents an excellent opportunity to apply the variational Bayesian inference approach introduced in the previous chapter.

6.3.3 Quantitative Analysis with Variational Inference

Bayesian inference requires the rigorous encoding of external knowledge of the system before to running the fitting algorithm. This external knowledge encoded in the fitting in the form of parameterized probability distributions known as priors. Literature information and characterization measurements will be used to construct these priors.

Consider the crystal structure of the CuBDC nanosheets shown in figure 1. While this idealized structure is likely true on average over short length scales, the mesoscale structure is likely very disordered given that the specific surface area is only 50 m^2/g and the internal regions are inaccessible. Fortunately, during the XRD measurements of the nanosheet sample, enough of the crystals were oriented to scatter X-rays off the (110) plane that a small peak at $2\theta = 9.39^{\circ}$ is visible in the pattern. Scherrer analysis of this peak indicates a lower bound on average grain sizes in the plane of the particle of 13.7 nm. Thus, the site prior should account for a high density of defect rich grain boundaries. We will also consider external surface sites and shallow pore sites. These are illustrated by the graphic in figure 6.5.

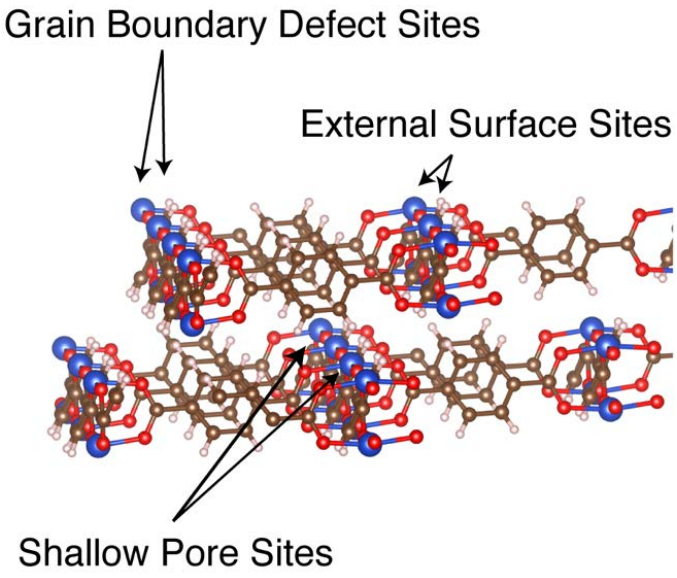

Figure 6.5 Illustration of possible metallic adsorption sites. Oxygen is shown in red, copper in blue, carbon in brown, and hydrogen in white.

Based on the geometry of the lattice, the ratio of external sites to shallow pore sites to grain boundary sites is expected to be 183:183:73 for a square region with side length 13.7 nm. This is to say, of 1/6 the three dominant surface sites are expected to be edge sites. CO_2 bound to these edge sites is likely to have a higher desorption enthalpy than if it were bound to the other sites given that these defect sites are undersaturated with linker bonds. Thus, we expect the higher temperature peak to correspond to desorption from grain boundary sites while the broad lower temperature peak is overlapped contributions from at least the two other sites. In order to ensure fit convergence and accommodate for unknown defect sites, three other sites were also used. These sites have large prior uncertainties in both their concentration and desorption activation energies to account for the fact that little is known or expected about their positions beforehand. Table 6.1 gives the prior mean parameters for each site. The activation energies are assumed to be uncorrelated while the coverage covariances are implicit in the Dirichlet distribution

parameters. Variational inference with stochastic search was run for 250 iterations and the algorithm converged to a local minimum at iteration 235. The results of the fit are shown in Figure 6.6.

Table 6.1 Bayesian Priors for Nanosheet Desorption Fit

Site Identity	$\boldsymbol{\mu_{Ea}}$	$\boldsymbol{\sigma_{E_a}}$	$\boldsymbol{a_{\theta_0}}$	$\mathbb{E}[\boldsymbol{\theta_0}]$	$\sqrt{\mathrm{Var}(\boldsymbol{\theta_0})}$
External	30 kJ/mol	2 kJ/mol	5	0.34	0.12
Shallow Pore	30 kJ/mol	2 kJ/mol	5	0.34	0.12
Grain Boundary	35 kJ/mol	2 kJ/mol	1.67	0.12	0.08
Unknown 1	32 kJ/mol	7 kJ/mol	1.0	0.07	0.06
Unknown 2	32 kJ/mol	7 kJ/mol	1.0	0.07	0.06
Unknown 3	32 kJ/mol	7 kJ/mol	1.0	0.07	0.06

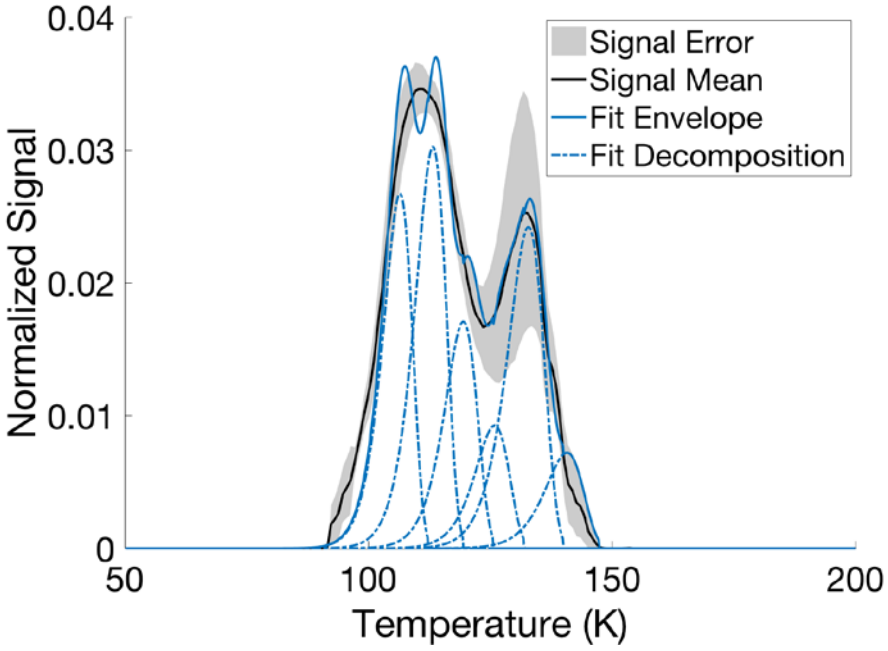

Figure 6.6 Bayesian fit of CO_2 TPD signal from CuBDC nanosheet sample.

Table 6.2 Posterior Parameter Distributions Given Nanosheet TPD Data

Site Identity	$\boldsymbol{\mu_{Ea}}$	$\boldsymbol{\sigma_{E_a}}$	$\boldsymbol{a_{\theta_0}}$	$\mathbb{E}[\boldsymbol{a_0}]$	$\sqrt{\mathrm{Var}(\boldsymbol{a_0})}$
External	31.14 kJ/mol	0.17 kJ/mol	8.0	0.21	0.07
Shallow Pore	33.18 kJ/mol	0.16 kJ/mol	9.6	0.25	0.07
Grain Boundary	39.0 kJ/mol	0.17 kJ/mol	8.9	0.23	0.07
Unknown 1	37.0 kJ/mol	0.51 kJ/mol	3.2	0.08	0.04
Unknown 2	35.1 kJ/mol	0.60 kJ/mol	5.7	0.15	0.06
Unknown 3	41.5 kJ/mol	0.92 kJ/mol	2.8	0.07	0.04

While the fit isn't perfect, the simulated curve falls within one standard deviation of the signal mean over most of the temperature range as shown by the solid blue line superimposed on the gray band in Figure 6.6. The posterior distributions are listed in Table 6.2. Note that the variances of the posterior distribution are much smaller than those of the prior. This should make intuitive sense given that the prior represents a vague estimate of the parameters while the posterior is a refinement of that estimate in light of data. There are a number of interesting implications indicated by the posterior distribution over the fit parameters. The first is the collection of high activation energy curves that comprise the signal. In addition to the prominent feature ascribed to grain boundary sites, there are three other sites with higher desorption enthalpies the external and pore sites that contribute to the main peak. The two lower-energy unknown peaks, labelled *Unknown 1* and *Unknown 2* in Table 6.2, may be external or shallow pore sites at locations of unusual surface topography such as corrugated regions induced by buried grain boundaries.

The concentration of grain boundary defects was found to comprise nearly a quarter of the entire surface with relatively small uncertainty in this parameter. This suggests that, if this peak is indeed associated with desorption from unsaturated metal sites, that there are a large number of such sites relative to saturated sites. This population likely includes grain boundary defects as well as other missing linker defects more generally.

6.4 Conclusion

Temperature programmed desorption was used in combination with X-ray diffraction and BET surface area analysis to explore the mechanism for the increased binding affinity for CO_2 of CuBDC nanosheets compared to bulk CuBDC. Variational Bayesian inference via stochastic gradient ascent was used to incorporate information from auxiliary measurements into the nonlinear fit of the TPD profile. All CO_2 adsorption sites on CuBDC nanosheets were found to have higher activation enthalpies than those on the bulk crystals. The desorption activation energy from the bulk crystal was measured to be roughly 26.0 kJ/mol, while it was found to range from 31.14 to 41.5 kJ/mol for the nanosheet samples.

The bimodal nanosheet TPD profile indicates a high density of defect sites on the material's surface. These defects play a role in the increased affinity for CO_2 observed by Rodenas *et al* but do not entirely explain the phenomenon given that the peaks from pristine sites are also shifted to higher temperatures than that of the bulk material. High resolution surface imaging via scanning probe microscopy may shed more light on this problem by characterizing the distribution of surface topographies present on the nanosheet sample.

6.5 References

1. Eddaoudi, M.; Li, H.; Yaghi, O. M., Highly Porous and Stable Metal−Organic Frameworks: Structure Design and Sorption Properties. *J. Am. Chem. Soc.* **2000**, *122*, 1391-1397.
2. Eddaoudi, M.; Moler, D. B.; Li, H.; Chen, B.; Reineke, T. M.; O'Keeffe, M.; Yaghi, O. M., Modular Chemistry: Secondary Building Units as a Basis for the Design of Highly Porous and Robust Metal−Organic Carboxylate Frameworks. *Acc. Chem. Res.* **2001**, *34*, 319-330.
3. Barea, E.; Montoro, C.; Navarro, J. A. R., Toxic Gas Removal - Metal-Organic Frameworks for the Capture and Degradation of Toxic Gases and Vapours. *Chem. Soc. Rev.* **2014**, *43*, 5419-5430.
4. Czaja, A. U.; Trukhan, N.; Muller, U., Industrial Applications of Metal-Organic Frameworks. *Chem. Soc. Rev.* **2009**, *38*, 1284-1293.
5. Li, J.-R.; Kuppler, R. J.; Zhou, H.-C., Selective Gas Adsorption and Separation in Metal-Organic Frameworks. *Chem. Soc. Rev.* **2009**, *38*, 1477-1504.
6. Ming-Xue, W.; Ying-Wei, Y., Metal–Organic framework (MOF)-Based Drug/Cargo Delivery and Cancer Therapy. *Adv. Mater.* **2017**, *29*, 1606134.
7. Rodenas, T.; Luz, I.; Prieto, G.; Seoane, B.; Miro, H.; Corma, A.; Kapteijn, F.; Llabrés i Xamena, F. X.; Gascon, J., Metal–Organic Framework Nanosheets in Polymer Composite Materials for Gas Separation. *Nat Mater* **2015**, *14*, 48-55.
8. G., C. C.; Kenneth, H.; Justin, S.; Xiaotao, L.; Christina, H.; A., G. R.; Rina, T., Synthesis and Structure Characterization of Copper Terephthalate Metal–Organic Frameworks. *European Journal of Inorganic Chemistry* **2009**, *2009*, 2338-2343.

CHAPTER 7. REACTIVE SO_2 ADSORPTION ON METAL-ORGANIC FRAMEWORK NANOSHEETS IN HUMID ATMOSPHERE

7.1 Introduction

This chapter appeared in *The Journal of Physical Chemistry C* in May of 2018.[1] It is reproduced here with permission. Metal-organic frameworks (MOFs) are a class of porous materials that are promising candidates for application in molecular separation technologies.[2] These materials are composed of metal nodes linked by bridging ligands to form ordered coordination networks. Open-metal-site MOFs are a subclass of MOFs in which the metal coordination sites are not fully saturated by structural ligands or linkers.[3] After an activation procedure in which solvent molecules are released from the open metal site by heating the material under vacuum, these open metal sites are available to react with guest molecules as Lewis acids, which may be advantageous for applications such as gas storage and separation.[4-6] Open-metal-site MOFs such as HKUST-1 have been proposed for removal of harmful gases from fuel and exhaust streams.[3, 7-9] Sulfur dioxide is a toxic contaminant in coal combustion flue gas and a major contributor to acid rain. It is also a gas for which open metal MOFs have a particularly strong affinity.[10-12] While such materials are stable under dry SO_2 exposure, the relative humidity in flue gases is very high (> 90%).[10, 13-15] Ideally, material candidates should be stable under exposure to the acidic products of reactive adsorption of humid SO_2.[16] The stability of the pore structure of the material is particularly important because this determines the accessibility of sites.[17]

MOF-2 is an open metal MOF comprised of 1,4-benzenedicarboxylate (BDC) linker molecules that bridge metal atoms in a two-dimensional (2D) network. The structure of the nodes in these MOFs is chemically identical to that of HKUST-1 and thus MOF-2 can be thought of as a 2D analog for HKUST-1.[18] The 3D structure of MOF-2 is composed of ordered stacks of the 2D networks held together by non-bonded polar interactions.[18] Other 2D MOFs similar to MOF-2 have recently received attention for applications in catalysis and membrane separation.[19-23] While the 2D coordination networks of these materials are identical to that of MOF-2, their stacking is disordered and as a result, their specific surface area (i.e., that accessible to molecules like SO_2) is limited to the external surfaces.[20] Additionally, the high aspect ratios and highly oriented structures of the particles provide advantages in experimental design including straightforward interpretation of diffraction patterns and X-ray photoelectron spectra. The above factors present an opportunity to understand the changes induced in the 2D surfaces by acid gas exposure, without having to exfoliate the material into individual nanosheets.

Towards this end, in the present work we synthesized copper, zinc, and cobalt benzenedicarboxylate nanosheets (CuBDC, ZnBDC, and CoBDC respectively) and exposed them to different dose durations of 40 ppm SO_2 under high relative humidity (85 % R.H.) in air. The effects of this exposure were characterized by a suite of techniques: X-ray photoelectron spectroscopy (XPS), Fourier Transform Infrared Spectroscopy (FTIR), powder X-ray diffraction (PXRD), and scanning electron microscopy (SEM). These measurements were compared to control groups in humid environments as well as the pristine activated materials to determine the chemical and structural changes induced by humid SO_2 exposure. Trends in the structural dynamics as a function of the metal center were established. We consider the chemical, structural, and morphological data together to yield insights into the mechanism of catalytic

oxidation of SO_2 in MOF nanosheets, the nature of lattice defects created by SO_2 exposure, and the stability of the chemisorbed SO_2.

7.2 Experimental Section

7.2.1 Synthesis of MOF nanosheets

MOF nanosheets were synthesized by the layered, diffusion-mediated method reported by Rodenas *et al.*[20] The procedure was modified for larger-scale nanosheet production using standard laboratory glassware. Details specific to each material are included in the following subsections. In general, the miscible layers of the reaction system consist of mixtures of N,N-dimethylformamide (DMF) and acetonitrile (CH_3CN) in varying ratios. Layers were added sequentially in order of decreasing density such that mixing was minimal. The three layers, referred to as the metal layer, the spacer layer, and the linker layer, initially contain dissolved ionic metal compounds, no solute, and benzenedicarboxylic acid (BDCA) respectively. A standard 100 ml beaker (14 mm radius) was used as the reaction vessel in each case. Precipitated MOF crystals were recovered by centrifugation at 6000 rpm for 20 minutes. MOF product was washed three times with CH_3CN and twice with dichloromethane, allowing at least three hours between each wash for solvent exchange. All samples were activated under vacuum at 150 °C for 24 hours.

Copper benzenedicarboxylate (CuBDC). The linker layer was prepared by dissolving 300 mg BDCA in a mixture of 20 ml DMF and 100 ml CH_3CN and poured into the reaction vessel. A spacer layer comprised of a mixture of 10 ml DMF and 10 ml CH_3CN was poured over to the linker layer. The metal layer was then prepared by dissolution of 300 mg $Cu(NO_3)_2 \cdot 3H_2O$ in a

mixture of 10 ml DMF and 20 ml CH_3CN and poured over the spacer layer. The layered mixture was then allowed to react at 40 °C for 24 hours before MOF precipitate was recovered.

Zinc benzenedicarboxylate (ZnBDC). The linker layer was prepared by dissolving 200 mg BDCA in a mixture of 20 ml DMF and 100 ml CH_3CN and poured into the reaction vessel. A spacer layer comprised of a mixture of 10 ml DMF and 10 ml CH_3CN was poured over to the linker layer. The metal layer was then prepared by dissolution of 100 mg $Zn(CH_3COO)_2 \bullet 2H_2O$ in a mixture of 10 ml DMF and 20 ml CH_3CN and poured over the spacer layer. The layered mixture was then allowed to react at 40 °C for 24 hours before MOF precipitate was recovered.

Cobalt benzenedicarboxylate (CoBDC). The linker layer was prepared by dissolving 70 mg BDCA in a mixture of 20 ml DMF and 100 ml CH_3CN and poured into the reaction vessel. A spacer layer comprised of a mixture of 10 ml DMF and 10 ml CH_3CN was poured slowly over to the linker layer. The metal layer was then prepared by dissolution of 70 mg anhydrous $Co(CH_3COO)_2$ in a mixture of 10 ml DMF and 20 ml CH_3CN and poured slowly over the spacer layer. The layered mixture was then allowed to react at room temperature for 24 hours before MOF precipitate was recovered.

7.2.2 Exposure to humid atmosphere with trace SO_2

To minimize diffusion effects associated with exposure of a powdered material, the samples were prepared as thin films coated on glass slides. Activated samples were exposed to 40 ppm of SO_2 in air with relative humidity of 85% for time intervals of 1 and 2 days at room temperature (25 °C). The acid gas mixture was prepared according to previous literature reports and is described in our previous work in detail.[24-25] Briefly, the SO_2 gas was generated from a 400 ml aqueous solution of 0.5 mg/ml $NaHSO_3$ at a pH of 3.7 at 45 °C. Air at 60 ml/min was

bubbled through the solution and carried humid SO_2 gas stream to the exposure unit (Secador mini-desiccator). Gas concentration inside the transparent exposure unit was continuously monitored with the portable PAC 7000 SO_2 detector (Dräger). The relative humidity was continuously monitored by a commercial humidity sensor (Ambient Weather). The water bath, acid gas generator and exposure unit were all placed inside a fume hood with high exhaust rates and handled with caution. All samples of a given dose were exposed at the same time in the same chamber to maintain consistency. A control set was also tested by placing activated samples inside the exposure chamber for 1 and 2 days at 85% relative humidity and 0 ppm SO_2. In order to generalize these results for comparison with analogous work on other MOFs, we report the doses in terms of overall exposure in ppm-days, by multiplying the average concentration (40 ppm) with the dose duration to yield 0, 40, and 80 ppm-days.[25-26] Small quantities of exposed samples were transferred to gold coated silicon following exposure for XPS and SEM characterization.

7.2.3 Characterization of Exposure Effects

X-ray photoelectron spectra were measured using a Thermo Scientific K-Alpha+ X-ray Photoelectron Spectrometer System. Fourier Transform Infrared (FTIR) spectra were measured using a Bruker Vertex 70 FTIR spectrometer. SEM images were recorded using a Hitachi SU8230 field emission scanning electron microscope. X-ray diffraction patterns were measured using a Panalytical X'Pert Pro with an X'celerator detector and copper K_α source (λ = 1.54056 Å).

7.3. Results and Discussion

The evolution of the surface structure and sulfur adsorption chemistry will be considered in the context of the crystal structures and the metal chemistries of the three MOFs. All three types of 2D sheets take the MOF-2 structure, in which the unidirectional rhombohedral pores shown in Figure 7.1a are formed by four BDC linkers bridging two metal ions at each corner. The coordination complexes at the corners have the paddle wheel geometry (Figure 7.1b), with each metal bound to four oxygen atoms. The 3D structure consists of ordered stacking of these 2D networks (Figure 7.1c). The nanosheets show preferred orientation, with CuBDC favoring the $(\bar{2}01)$ orientation while that of ZnBDC and CoBDC favors (011). This difference in orientation is shown in Figure 1d and e. A graphical representation of the lattice planes and comparison of measured and simulated XRD patterns can be found in Figure A1. The degree to which the stacking is ordered determines the accessibility of the internal pore structure to guest molecules. The electronic configuration of the metal center also affects the stacking pattern by influencing the orientation of the aromatic rings with respect to the stacking direction.[14]

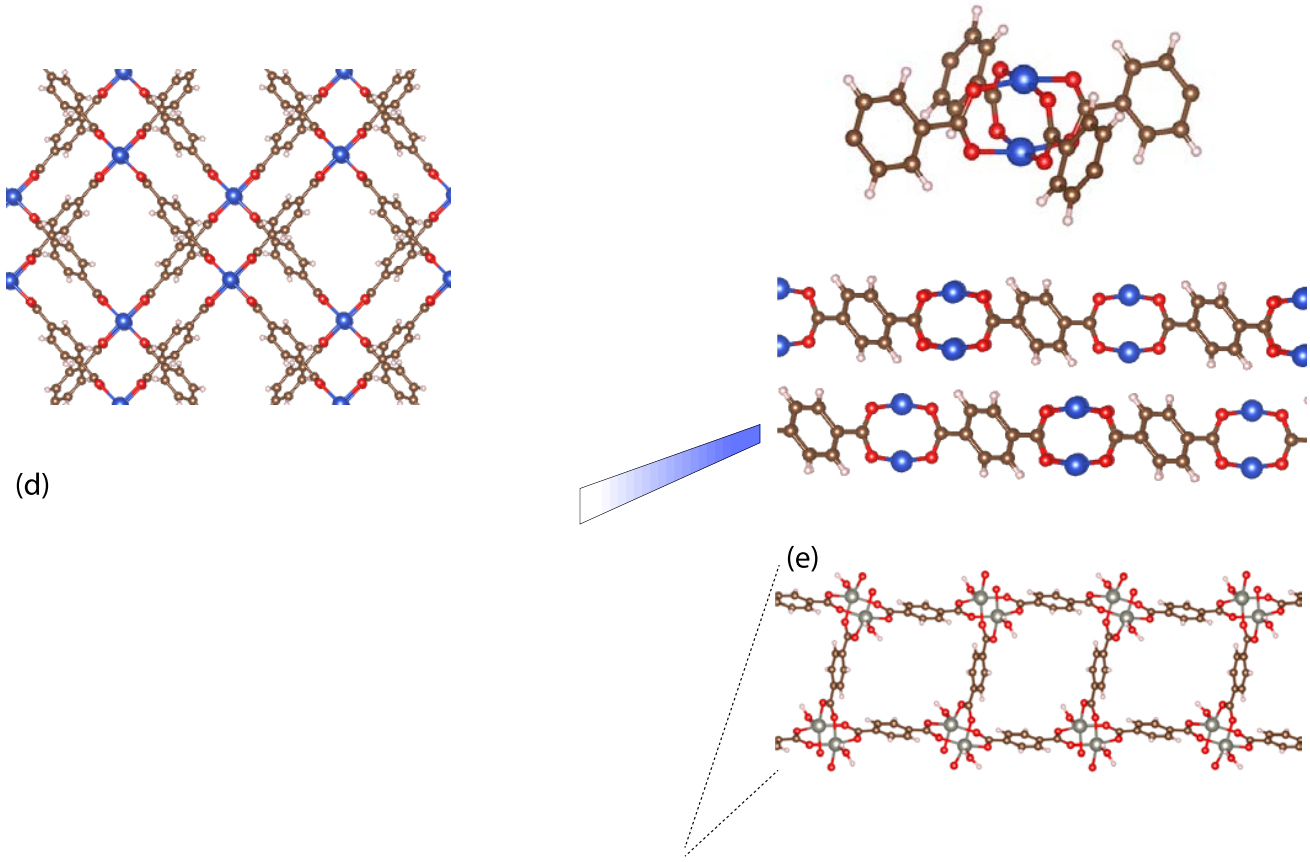

Figure 7.1 Models of crystal orientations of CuBDC (above) and ZnBDC (below). Top-down view of the pore opening of CuBDC nanosheets shown in (a), off-axis view of paddle-wheel coordination complex in (b), and side-view of laminar stacking pattern in (c). Top-down view of ZnBDC laminar stacking pattern shown in (d) and side-view of pore opening shown in (e). Copper atoms are shown in blue, zinc in grey, carbon in brown, oxygen in red, and hydrogen in grey.

As noted by Rodenas *et al*, the internal pore structure is not easily accessible even to small molecules such as nitrogen.[20] The nitrogen BET surface areas of CuBDC, ZnBDC, and CoBDC are 50, 22, and 46 m^2/g respectively, and are exclusively due to their external surfaces.[20] This is likely due to disordered stacking of the internal layers of the sheets, as will be discussed in greater detail below. As will be shown, these materials also have an abundance of native lattice defects as well as variations in pore shape, that introduce the potential for interesting chemical interactions with guest gases. The following discussion aims to understand the reaction between the sulfur atmosphere and MOF nanosheet materials by starting with the local chemical changes and subsequently observing the crystallographic and morphological degradation of the particles. The chemical state of the samples measured by XPS is presented first, followed by the progression of the vibrational spectra over the course of the exposure, with the structural impact of these chemical changes presented in the evolution in the XRD patterns and SEM images. Because humidity is known to induce structural and chemical changes in carboxylate MOFs, FTIR spectra and X-ray diffraction patterns of the control group samples are included in the appendix.[27] The most significant structural change observed across relative humidity exposures was the change in inter-laminar lattice spacing of CuBDC as the material became loaded with water. This is consistent with literature reports for water-induced decomposition of carboxylate MOFs, in which structural changes occur over a period of weeks rather than days.[28]

7.3.1 Reactive adsorption and chemical evolution

We first examine the distribution of oxidation states of sulfur in each material after 80 ppm-days of exposure. **Figure 7.2** shows the sulfur 2p XPS signals from each sample. These spectra all exhibit peaks at 169 and 162 eV with different intensities. The absence of a peak from

molecular SO_2 at 167 indicates that adsorbed sulfur has been oxidized or reduced.[29] The higher energy peak may correspond to sulfur in the +4 or +6 oxidation state, indicating a conversion of sulfur dioxide to sulfite or sulfate respectively.[30] This result is unsurprising given that aqueous oxidation of SO_2 is known to proceed in both the presence and absence of transition metals.[13, 31] The lower energy peak indicates sulfur present in the +1 or +2 oxidation state.[30] Sulfur is in the +4 oxidation state in SO_2 and the reduction to the +2 state in an oxidizing humid environment is surprising. The relative intensities of these peaks vary across the materials. CuBDC shows a larger presence of the reduced sulfur product while ZnBDC and CoBDC show a preference for the oxidized product. Table 7.1 gives the integrated peak areas and corresponding relative concentrations. Doublets are reported as the sum of both peak integrals with the location given as the center of the lower-energy ($j = 1/2$) peak. The relative concentrations represent the fractions of the total sulfur content of the material comprised of sulfide and sulfate. The number of sulfur atoms per unit cell were computed as the ratio of sulfur concentration to half of the associated metal concentrations given that there are two metal atoms per unit cell. Concentrations were computed as the fraction of the integrated signal associated with a given element scaled by the appropriate ionization cross sections. Based on these concentrations, the three materials have comparable sulfur dioxide uptake, and after 80 ppm-days every metal site is associated with at least one sulfur atom.

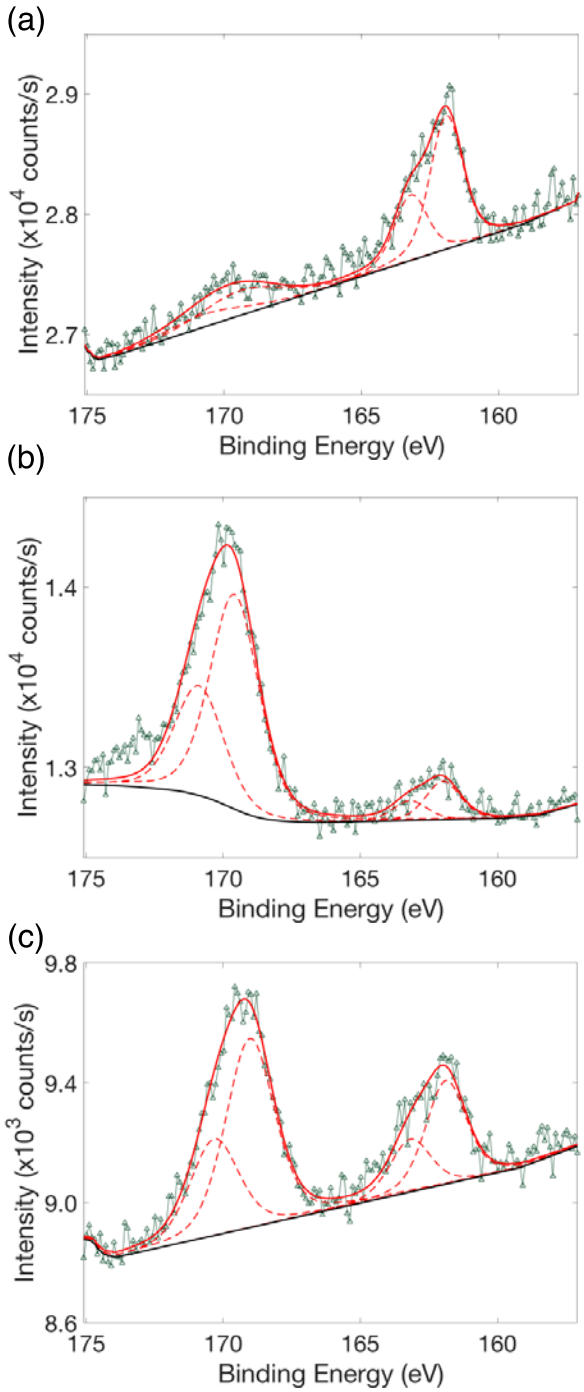

Figure 7.2 Sulfur 2p region of XPS spectra of CuBDC (a), ZnBDC (b), and CoBDC (c) measured after 80 ppm-days of exposure. Measured data are represented by green triangles, overall fits shown by red solid lines, and decomposition by red dashed lines.

Table 7.1 Integrated Sulfur Peak Intensities after 80 ppm-days Humid SO_2 Exposure

Material	Position (eV)	Integrated Absolute Intensity (eV x Counts)	Relative Concentration	Sulfur atoms per unit cell
CuBDC	162	2758	69 %	1.41
	169.1	1257	31 %	0.64
ZnBDC	162	571.0	11%	0.29
	169.5	4456	89 %	2.27
CoBDC	161.9	1074	31 %	0.85
	169.1	2346	69 %	1.85

Normalized overlays of the deconvoluted Cu 2p, Co 2p, and Zn 2p XPS spectra of the three materials before and after humid SO_2 exposure are shown in Figures 7.3a-c. The Cu 2p spectrum shows a dramatic change after exposure, with a second large doublet peak shifted by 2 eV higher than the doublet associated with the pristine material. A shake-up satellite peak at 943.9 eV is visible in the exposed spectrum (red).[30, 32] Such features generally coincide with paramagnetism, indicating the presence of an unpaired electron in the Cu 2p level. The shifted doublet at 936 eV corresponds to a copper atom in which the shielding of the 2p level from the nucleus is reduced.[30] In other words, the local electron density in the shifted peak is lower than that of the original peak at 932 eV, indicating a change in the ligand environment, such as linker removal. The Zn 2p spectrum also shows two doublet peaks after exposure where there was a single doublet before. Like the shifted Cu 2p doublet, the shifted Zn 2p doublet is consistent with loss of electron density from the zinc atom corresponding to linker removal. The Co 2p signal

shows much less change with exposure than the other two metals. Two doublets centered at 782.2 and 786.8 eV are present both before and after exposure. This suggests a high defect density in pristine CoBDC and that it increases with humid SO_2 exposure.

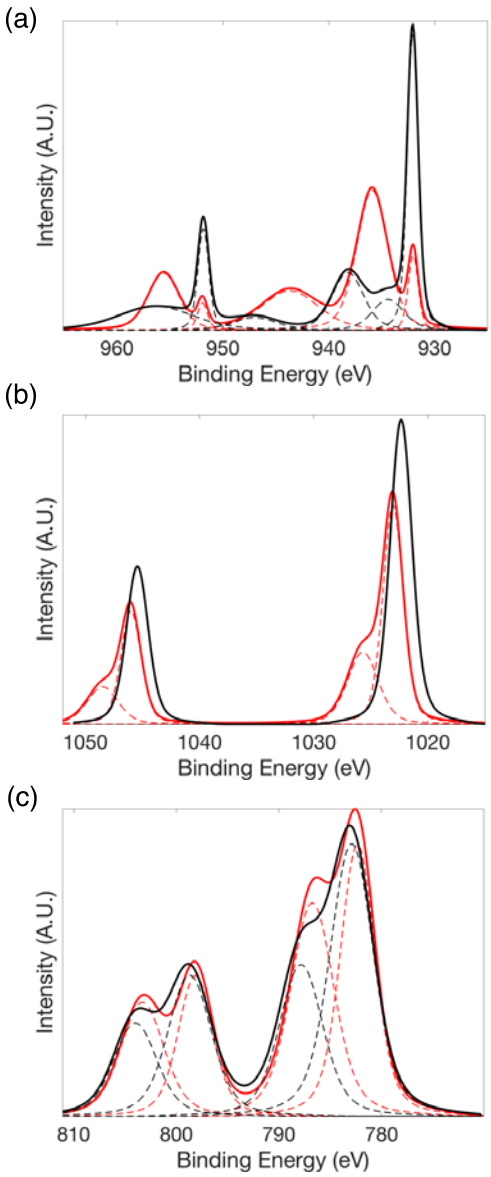

Figure 7.3 Cu 2p (a), Zn 2p (b), and Co 2p (c) fits of XPS spectra measured from CuBDC, ZnBDC, and CoBDC after 0 (black) and 80 (red) ppm-days of exposure to humid SO_2. Data points have been removed for clarity and can be found in the appendix. Peaks have been normalized to the signal envelope and the background has been subtracted for comparison.

Table 7.2 Integrated Metal Peak Intensities after 80 ppm-days Humid SO_2 Exposure.

Material	Position (eV)	Integrated Absolute Intensity (eV x Counts)	Relative Intensity	Notes
CuBDC	932.0	2852	12 %	doublet
	936.0	16547	65 %	doublet
	943.9	6100	23 %	satellite
ZnBDC	1023	2091	67 %	doublet
	1026	1038	33 %	doublet
CoBDC	782.2	1900	50 %	doublet
	786.8	1893	49 %	doublet

The normalized C 1s XPS spectra from samples after activation (black) and 80 ppm-days humid SO_2 exposure (red) are shown in Figure 7.4. The integrated peak intensities are given in Table 7.3. The strong peak at 284.8 eV in each spectrum is associated with carbons in the aromatic ring of the BDC. The spectra also show a peak near 287 eV corresponding primarily to the O-C-O carbons on the carboxylate linker as well as residual C-O methanol carbons.[30] The carbon XPS spectrum of CuBDC prior to exposure also contains large π-π^* satellite features at 290.6 and 294.5 eV. These peaks are normally found in graphitic carbons and correspond to the high delocalization of π electrons in those materials.[30] In CuBDC, the copper's electronic configuration ($[Ar]3d^{10}4s^1$) is unfilled, allowing a large degree of π electron delocalization in network prior to exposure. After exposure, defects induced in the lattice prevent this delocalization and the peak is reduced. The O-C-O peak at 286.8 eV is very strong both before

and after exposure and a carbonyl peak is not resolvable from the signal. In the case of ZnBDC, there are no π- π^* satellite features because the metal's electron shell is full and long-range delocalization is not possible in this material. Prior to exposure, ZnBDC shows an O-C-O peak at 286.8 eV and the aromatic ring peak at 284.8 eV. These peaks remain after exposure, with an additional carboxylic acid peak at 288.8 eV which may correspond to linkers that have been protonated and separated from the metal center. In CoBDC, the spectrum from the pristine activated sample provides further evidence that the material has a high defect density prior to exposure, since a large carbonyl peak is present and corresponds to uncoordinated linkers. This peak grows somewhat with exposure, similar to Figure 7.3.

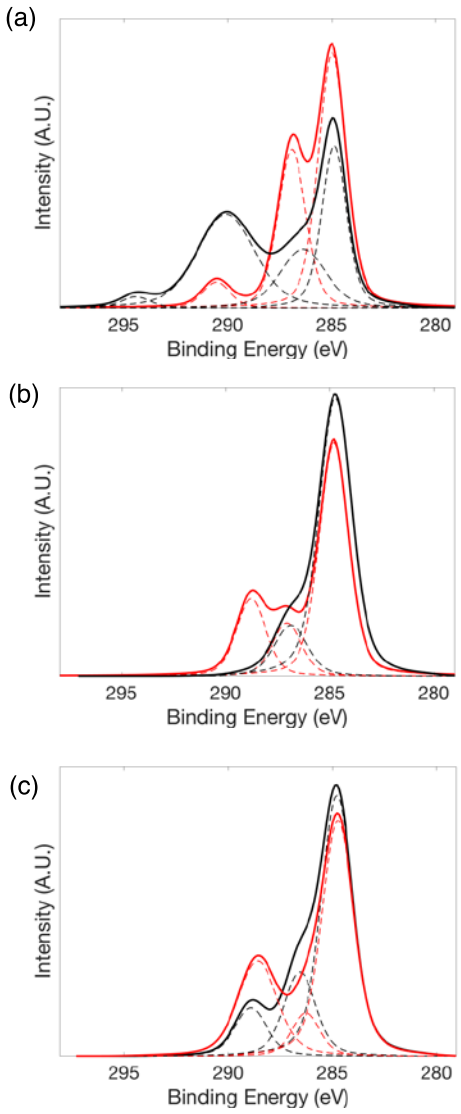

Figure 7.4 Carbon 1s XPS fits from CuBDC (a), ZnBDC (b), and CoBDC (c). Black spectra were measured from pristine samples and red spectra were measured from samples after 80 ppm-days. Data points have been removed for clarity and can be found in the appendix. Peaks have been normalized to the signal envelope and the background has been subtracted for comparison.

Table 7.3 Integrated Carbon Peak Intensities after 80 ppm-days Humid SO_2 Exposure

Material	Position (eV)	Integrated Absolute Intensity (eV x Counts)	Relative Intensity	Functional group
CuBDC	284.8	18941	45 %	C=C
	286.8	19539	47 %	O-C-O
	290.6	3178	8 %	C=C, satellite
ZnBDC	284.8	3536	25 %	C=C
	287.1	4328	31 %	O-C-O
	288.8	6303	45 %	O-C=O
CoBDC	284.8	10255	66 %	C=C
	286.6	1889	12 %	O-C-O
	288.6	3309	21%	O-C=O

Chemical changes within the MOF nanosheets were also probed using transmission FTIR spectroscopy (Figure 7.5). The widths of the particles range from 5 nm to 20 µm, causing Rayleigh scattering of visible and infrared wavelengths. This resulted in irregular baseline features in the FTIR spectra that have been computationally corrected via baseline interpolation. All FTIR signals have been normalized to the aromatic C=C peak at 1510 cm^{-1}, which is unlikely to have changed across exposures given the relatively high stability of the linker's ring structure. The prominent features of the CuBDC FTIR spectra include an acid C=O stretch at 1691 cm^{-1}, C=C stretches at 1557 and 1510 cm^{-1}, and the symmetric and asymmetric O-C-O stretches at 1384 and 1572 cm^{-1} respectively.[33]

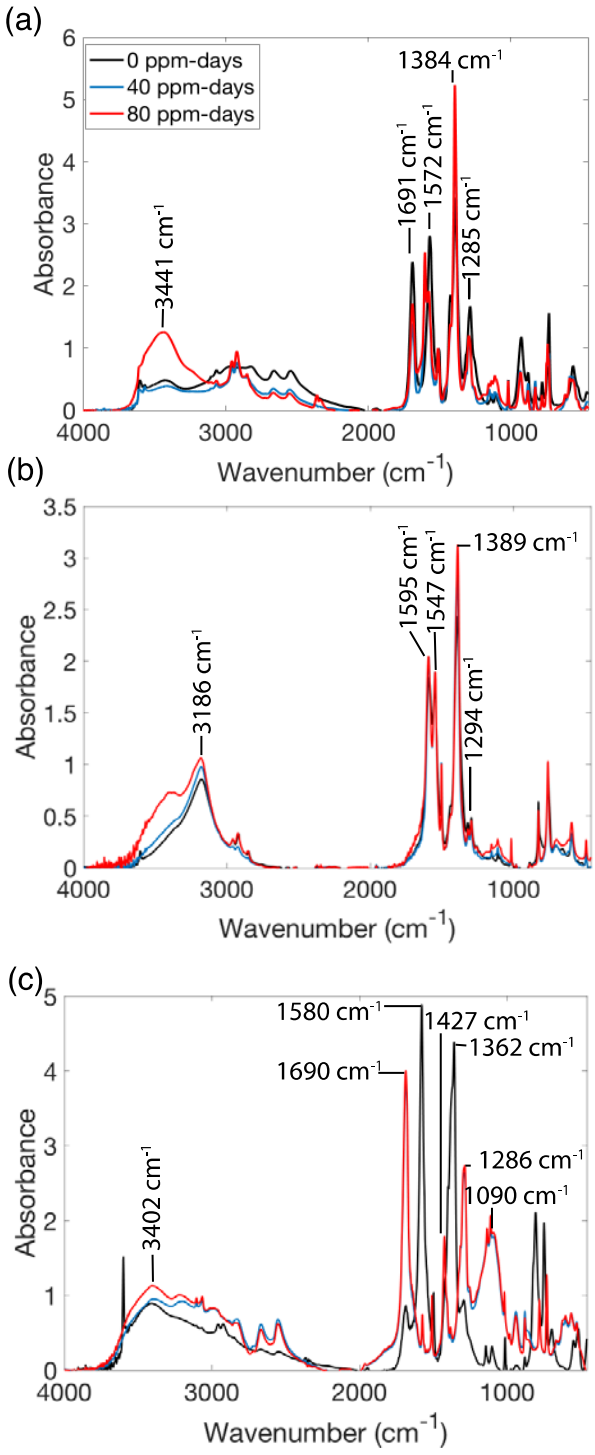

Figure 7.5 Transmission FTIR spectra of CuBDC (a), ZnBDC (b), and CoBDC (c), after 0 (black), 40 (blue), and 80 (red) ppm-days of humid SO_2 exposure.

The acid C=O absorption at 1691 cm^{-1} indicates a substantial quantity of terephthalic acid trapped inside the material. This is consistent with the inaccessibility of the pore structure due to irregular stacking, as discussed above. A new peak at 1605 cm^{-1} appears after exposure with a stronger intensity than the C=C peaks adjacent to it, this is attributable to the bending mode of adsorbed water, the loading of which increases as defects are induced in the lattice. The hydrogen bonding peak at 3441 cm^{-1} also grows relative to the isolated symmetric and asymmetric water stretches at 3620 and 3568 cm^{-1} respectively, owing to increased heterogeneity in the degraded sample. The peak at 1285 cm^{-1} is in a region typically attributed to ether v(C-O) absorptions.[30] Given that its intensity decreases with SO_2 exposure, we attribute this peak to the M-C-O stretch.[34] There were no significant changes in the region below 1285 cm^{-1}. The FTIR spectrum of the CuBDC control sample (Figure A2) showed much more prominent water absorption than the sample exposed to the humid sulfur atmosphere, as indicated by very strong peaks at 3451 and 1600 cm^{-1}. The control sample spectrum also shows large overtone aromatic C-H stretches at 2959 and 2956 cm^{-1} that are not otherwise visible in CuBDC spectra but are visible in all the ZnBDC and CoBDC spectra.[33] This may be the result of an increase in interlayer spacing with water uptake. The major deviations across exposure times in the ZnBDC FTIR spectra are mainly due to irregularities in the baseline. There are notable differences between the ZnBDC and CuBDC spectra. Specifically, none of the ZnBDC spectra contain a peak near 1690 cm^{-1}. This can also be interpreted as an absence of uncoordinated terephthalic acid inside the material. The FTIR spectra of CoBDC illustrates the dynamics of the acid-gas induced change in the local bond structure of the material and also contains mechanistic information in sulfate formation within the material. The behavior of the peak at 1690 cm^{-1} in CoBDC contrasts with that of CuBDC, in that it grows dramatically with exposure to humid SO_2.

This peak is attributed to free carboxylate functionalities associated with unbound linker defects that are introduced by acid exposure. The increased intensity of the metal-oxygen-carbon stretch at 1286 cm^{-1} with exposure appears to contradict the previous statement, but it should be noted that this peak overlaps a broad sulfite peak at 1090 cm^{-1}.[35] This is consistent with the CoBDC S2p XPS spectra, which shows comparable sulfate and reduced sulfur concentrations.

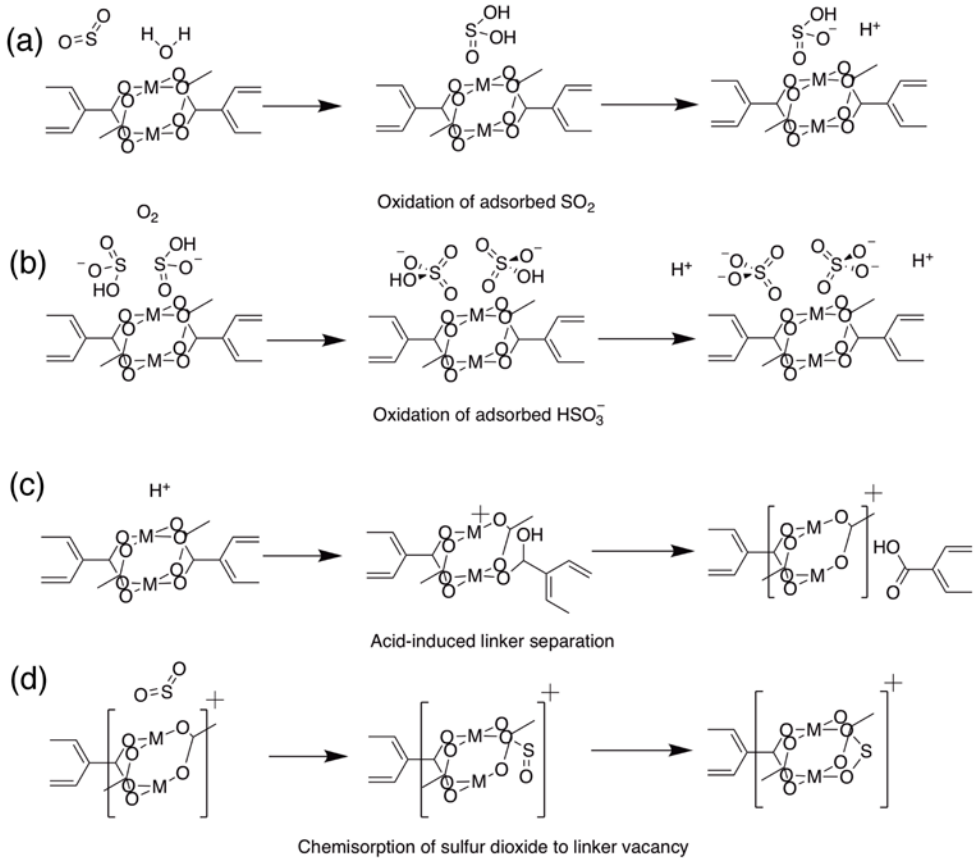

Figure 7.6 Proposed mechanisms for oxidation of adsorbed SO_2 (a), oxidation of adsorbed bisulfite (b), acid-induced linker separation (c), and chemisorption of SO_2 on the resulting defect site (d). Zinc or Cobalt atoms are indicated by "M".

The oxidation states of sulfur, when considered in the context of the changes in in the local bonding structure of these MOFs, point to a stepwise mechanistic pathway for the reactive adsorption of SO_2 in Zn and Co-BDC MOFs. Previous work describes mechanisms of gas-phase oxidation of SO_2 in dark, humid atmosphere.[25] While these may be sources of sulfite and sulfate, we focus our discussion here on possible mechanisms of oxidation at the MOF surface. Given that these materials have a high affinity for water, we expect these reactions to proceed comparably oxidation of aqueous SO_2.[31] A schematic of the proposed mechanisms is given in Figure 7.6. The sulfite peak present at 1090 cm^{-1} in the CoBDC spectrum after exposure supports the first step of the mechanism in which co-adsorbed water and SO_2 react to form a bisulfite ion shown in Figure **7.**6a.[31] The sulfite signal is absent in the ZnBDC FTIR spectrum but the sulfur XPS spectrum shows a large concentration of oxidized sulfur. There is a small, broad peak at 1111 cm^{-1} in the ZnBDC FTIR spectra that is absent prior to exposure and grows with dose. This peak is attributable to SO_4^{2-}, indicating oxidation of bisulfate produced by the initial reaction as shown in Figure 7.6b.[36] The acidic species produced by the first two reactions then attack the oxygens bound to the metal centers, causing the linkers to separate and leaving two unsaturated metals for subsequent SO_2 adsorbates to bridge through oxygen-metal bonds (Figure 6c and d). Metal-sulfur dioxide complexes formed through metal-oxygen bonds, while uncommon, are not unheard of in transition metals and this configuration is consistent with the reduced sulfur XPS signal.[37] The dramatic increase in intensity of the C=O peak at 1690 cm^{-1} indicates a conversion of metal-bound oxygens to uncoordinated carboxylic acids. The resulting unsaturated metal center is then susceptible to chemisorption by SO_2.

The disproportionate ratio of reduced sulfur to oxidized sulfur in CuBDC suggests either a different mechanism or a very high concentration of native missing linker defects. A single-step

linker displacement reaction mechanism is consistent with the decrease in the C-O-M IR peak at 1284 cm^{-1} as well as the strong preference for reduced sulfur. This mechanism is shown in Figure 7.7. We note that both the multistep and single step mechanisms resulting in reduction of sulfur dioxide are hypothetical and are proposed here as a possible explanation for the XPS results.

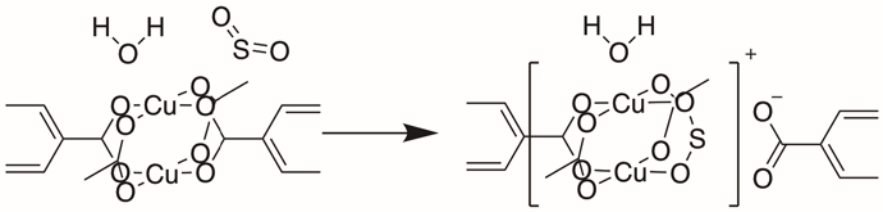

Figure 7.7 Single step linker displacement by SO_2 in CuBDC.

7.3.2 Structural Evolution

The impact of the interaction between the MOFs and the humid SO_2 atmosphere on the crystal structure was measured using grazing-angle X-ray diffraction. The XRD patterns for CuBDC, ZnBDC, and CoBDC, measured after 0, 40, and 80 ppm-days exposure, are given in Figure 7.8. Samples were mounted on glass slides, and hence the broad amorphous silica background peak is often visible. Miller indices of the peaks were assigned using the Vesta package based on Cu MOF-2, Zn MOF-2, and Co MOF-2 crystal structures. The indices and *d*-spacings of the pristine materials are listed in Table 7.4. As shown in Figure A1, only a subset of the brag peaks appear in each pattern due to the highly oriented crystal structures of the nanosheets. The CuBDC pattern shows reflections indexed at $(20\bar{1})$ and $(40\bar{2})$which are perpendicular to the basal plane of the material and thus a measure of interlayer separation. As the CuBDC nanosheets are exposed to larger doses of humid SO_2, the $(20\bar{1})$ peak at 18.63˚ recedes and new peaks at 17.73˚ and 15.57˚ appear.

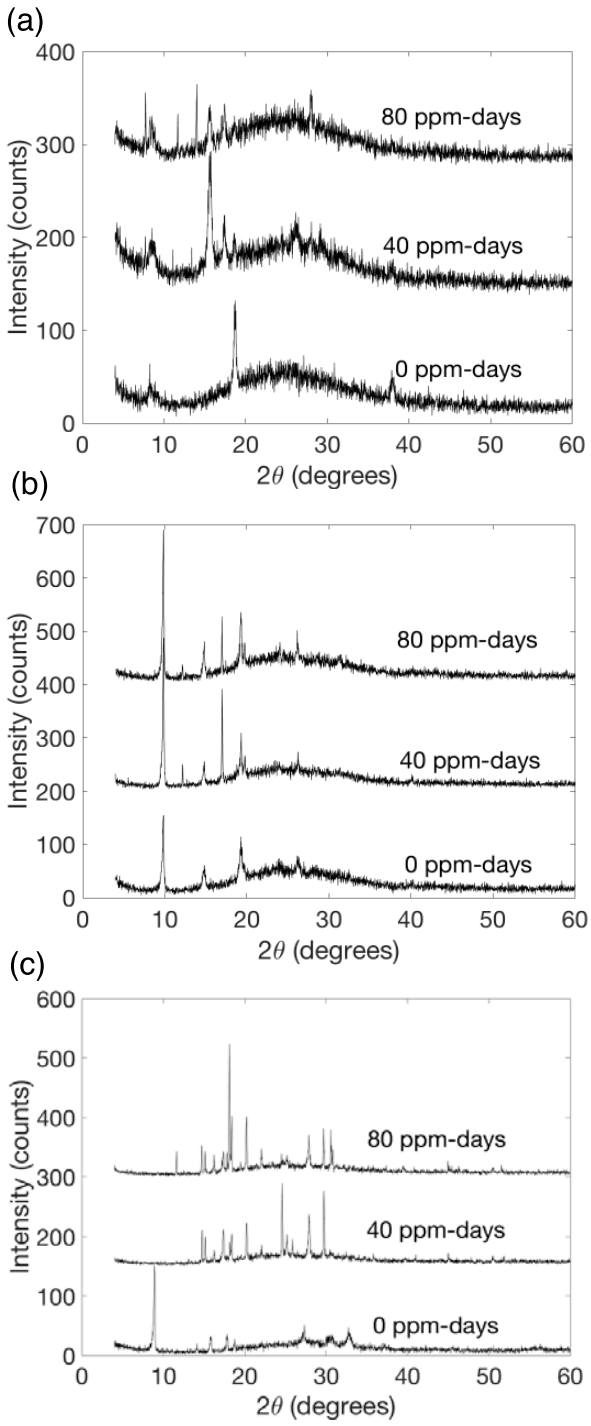

Figure 7.8 XRD patterns of CuBDC (a), ZnBDC (b), and CoBDC (c) after 0, 40, and 80 ppm-days of exposure to humid SO_2.

The peak at 17.73˚ ($d = 5.06$ Å) corresponds to regions in which the layers have been separated by water saturation (see appendix, Figure A3). The peak at 15.57˚ ($d = 5.68$ Å) is not present in the control samples and is attributed to sulfate or sulfide species separating the layers. This peak diminishes after 80 ppm-days as a critical fraction of linkers are replaced by bridging SO_2 ligands and the crystallinity of the lattice itself degrades. The layer stacking in ZnBDC is shifted relative to that of CuBDC due to the coordination chemistry of the metal nodes.[14] Because the orientation of the crystals sees the pores running perpendicular to the plane of the particle, the lower index (110) peak at 9.83˚ gives information about the intra-pore spacing of Zn atoms while changes in the higher index (301) peak at 19.33˚ can result from changes in the inter-layer spacing. Note that the (110) peak does not change with exposure but the (301) peak splits into a small peak at 19.73˚ and a larger peak at 19.29˚ after two days of exposure. This indicates that some layers of the crystal have been pushed apart while others have been pushed together. This change also occurs in the control sample and can be attributed to water adsorption. The CoBDC structure, which exhibits no change in the control sample, is seen to undergo a large change in the test sample that results in the loss of the intra-pore (110) peak at 8.81˚ and the appearance of a number of other peaks at higher angles. As with the FTIR spectrum, most of the change takes place between 0 and 40 ppm-days and there is little difference between the 40 and 80 ppm-days patterns, indicating that the structural changes occur early in the exposure duration.

Table 7.4 XRD Peak Assignments for Pristine MOF nanosheets (0 ppm-days)

Material	Peak Position	d-spacing (Å)	Index
CuBDC	18.63˚	4.83	$(20\bar{1})$
	38.11˚	2.49	$(40\bar{2})$
ZnBDC	9.83˚	8.99	(110)
	14.79˚	5.98	$(11\bar{1})$
	19.27˚	4.63	(301)
	26.17˚	3.40	(131)
CoBDC	8.81˚	10.03	(110)
	15.87˚	5.58	$(11\bar{1})$
	17.77˚	5.00	$(20\bar{1})$
	27.35	3.26	(131)
	30.51	2.93	$(33\bar{1})$
	32.55	2.75	(150)

7.3.3 Morphological Evolution

Figure 7.9 shows representative SEM images of the CuBDC material after 0, 40, and 80 ppm-days exposure. Erosion of the particle shapes appears to proceed from the edges toward the center. As indicated by arrows, CuBDC nanosheets have the most sharply defined edges, and this process is therefore most easily observed in this case. As the particles are exposed to larger doses the edges become more irregular, with an increasing number of the top surfaces of the sheets becoming wrinkled as well. SEM images of the control samples after two days of exposure to 85% relative humidity are shown in Figure A4.

The ZnBDC particles also show degradation at the edges but the top surface does not visibly change under any exposure (Figure S5). This effect occurs both in the presence and absence of SO_2 and thus is attributed to effects of humidity. Both CuBDC and ZnBDC particles change relatively little compared to CoBDC particles, which are seen to curl and aggregate after 40 ppm-days of exposure (Figure S5). These aggregates are likely dense (nonporous) structures with significant crystalline order, as indicated by the XRD patterns in Figure 7c. Given that the CoBDC particles are fully intact in the control sample group, this effect is fully attributable to the acidic atmosphere.

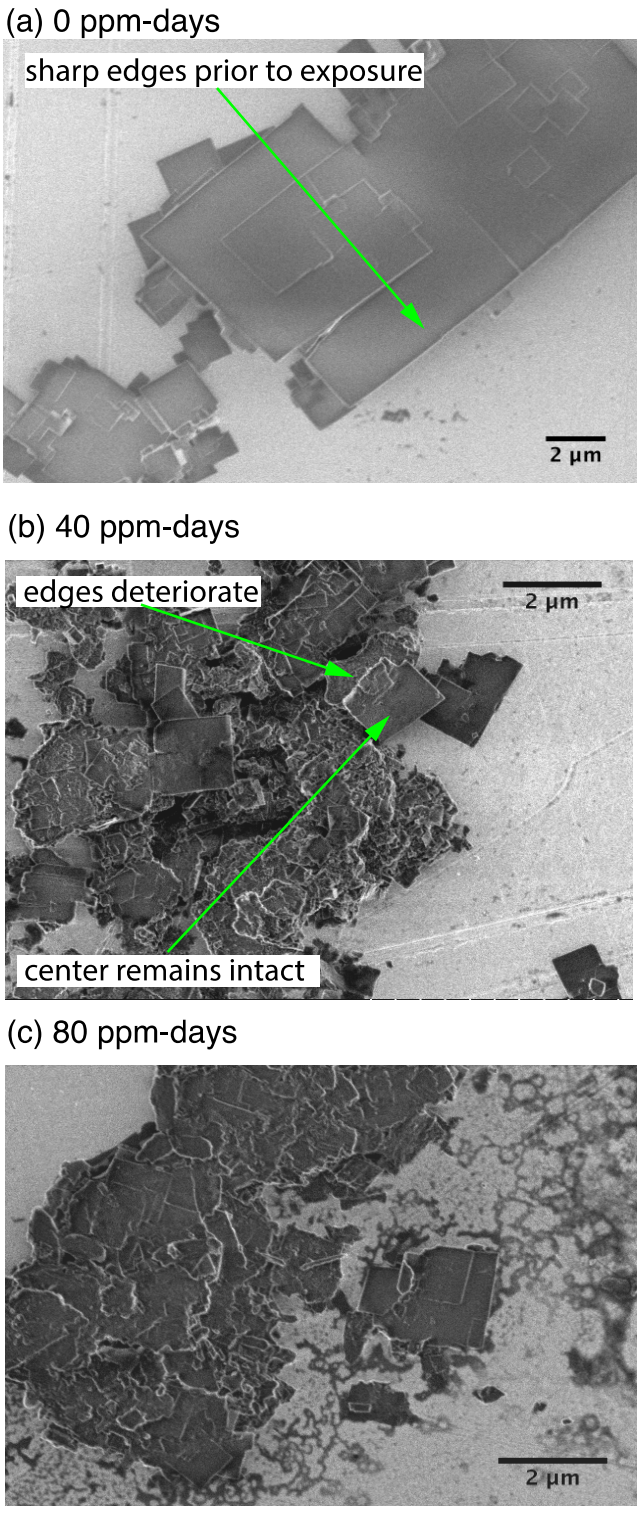

Figure 7.9 Scanning electron micrographs of CuBDC nanosheets after 0 (a), 40 (b), and 80 (c) ppm-days of exposure (from top to bottom respectively).

7.5. Conclusion

We have investigated in detail the chemical and structural modifications induced in 2D MOF nanosheets by exposure to humid SO_2 atmosphere, using a combination of vibrational spectroscopy, X-ray diffraction, X-ray photoelectron spectroscopy, and scanning electron microscopy. These modifications, when considered in the context of induced defect densities as well as the environments of the chemisorbed sulfur species, provide critical information about the microscopic surface structure. Both the rate of catalytic oxidation of SO_2 and the material stability in the resulting acidic environment, are important to determining their usefulness in applications where SO_2 is present. While the dramatic structural changes observed in CoBDC make it unsuitable for use in SO_2 separation, the large presence of sulfite inside the material lends insight into the oxidation reaction mechanism and its dependence on the chemical properties of the material. ZnBDC exhibits minimal structural change after exposure and its FTIR spectrum indicates the presence of sulfate species. After 80 ppm-days of exposure all three materials are effectively "fully loaded" with at least one sulfur atom associated with each metal atom. In CuBDC, 88% of adsorbed sulfur dioxide was found in a reduced oxidation state. The hypothetical bridging configuration for this state was proposed in Figures 7.6 and 7.7 will be the subject of future computational work. Given that SO_2 captured in this way is not converted to sulfuric acid, such a mechanism might be useful in wet desulfurization technologies.

Supporting Information

Additional experimental data and control results can be found in the appendix. Figures A1 and A2 show FTIR spectra and XRD patterns respectively of control samples. Figure A3 shows scanning electron micrographs of ZnBDC and CoBDC before and after humid SO_2 exposure.

Figures A4 and A5 respectively show metal and carbon XPS signal data before and after exposure.

7.6 References

1. Elder, A. C.; Bhattacharyya, S.; Nair, S.; Orlando, T. M., Reactive Adsorption of Humid SO_2 on Metal–Organic Framework Nanosheets. *J. Phys. Chem. C* **2018**, *122*, 10413-10422.
2. Rowsell, J. L. C.; Yaghi, O. M., Metal–Organic Frameworks: A New Class of Porous Materials. *Micropor. Mesopor. Mater.* **2004**, *73*, 3-14.
3. Bae, J.; Choi, J. S.; Hwang, S.; Yun, W. S.; Song, D.; Lee, J.; Jeong, N. C., Multiple Coordination Exchanges for Room-Temperature Activation of Open-Metal Sites in Metal–Organic Frameworks. *ACS Appl. Mater. Interfaces* **2017**, *9*, 24743-24752.
4. Dzubak, A. L.; Lin, L.-C.; Kim, J.; Swisher, J. A.; Poloni, R.; Maximoff, S. N.; Smit, B.; Gagliardi, L., Ab Initio Carbon Capture in Open-Site Metal–Organic Frameworks. *Nat Chem* **2012**, *4*, 810-816.
5. Lee, K.; Howe, J. D.; Lin, L.-C.; Smit, B.; Neaton, J. B., Small-Molecule Adsorption in Open-Site Metal–Organic Frameworks: A Systematic Density Functional Theory Study for Rational Design. *Chem. Mater.* **2015**, *27*, 668-678.
6. Howarth, A. J.; Peters, A. W.; Vermeulen, N. A.; Wang, T. C.; Hupp, J. T.; Farha, O. K., Best Practices for the Synthesis, Activation, and Characterization of Metal–Organic Frameworks. *Chem. Mater.* **2017**, *29*, 26-39.
7. Barea, E.; Montoro, C.; Navarro, J. A. R., Toxic Gas Removal - Metal-Organic Frameworks for the Capture and Degradation of Toxic Gases and Vapours. *Chem. Soc. Rev.* **2014**, *43*, 5419-5430.
8. Wang, X.-L.; Fan, H.-L.; Tian, Z.; He, E.-Y.; Li, Y.; Shangguan, J., Adsorptive Removal of Sulfur Compounds Using IRMOF-3 at Ambient Temperature. *Appl. Surf. Sci.* **2014**, *289*, 107-113.
9. Levasseur, B.; Petit, C.; Bandosz, T. J., Reactive Adsorption of No_2 on Copper-Based Metal−Organic Framework and Graphite Oxide/Metal−Organic Framework Composites. *ACS Appl. Mater. Interfaces* **2010**, *2*, 3606-3613.
10. Britt, D.; Tranchemontagne, D.; Yaghi, O. M., Metal-Organic Frameworks with High Capacity and Selectivity for Harmful Gases. *Proc. Natl. Acad. Sci. U.S.A.* **2008**, *105*, 11623-11627.
11. Poullikkas, A., Review of Design, Operating, and Financial Considerations in Flue Gas Desulfurization Systems. *Energy Tech. Policy* **2015**, *2*, 92-103.
12. Olatunji, S. O.; Fakinle, B. S.; Jimoda, L. A.; Adeniran, J. A.; Adesanmi, A. J., Air Emissions of Sulphur Dioxide from Gasoline and Diesel Consumption in the Southwestern States of Nigeria. *Pet. Sci. Technol.* **2015**, *33*, 678-685.
13. Flamm, D. L.; Bacon, D. D.; Kinsbrin, E.; English, A. T., Chemical Reaction of Sulfur Dioxide at High Humidity and Temperature: Implications for Accelerated Testing. *J. Electrochem. Soc.* **1981**, *128*, 679-685.

14. Howe, J. D.; Liu, Y.; Flores, L.; Dixon, D. A.; Sholl, D. S., Acid Gas Adsorption on Metal–Organic Framework Nanosheets as a Model of an "All-Surface" Material. *J. Chem. Theory Comput.* **2017**, *13*, 1341-1350.
15. Xie, J.; Yan, N.; Qu, Z.; Yang, S., Synthesis, Characterization and Experimental Investigation of Cu-Btc as Co2 Adsorbent from Flue Gas. *J. Env. Sci.* **2012**, *24*, 640-644.
16. Datta, S. J., et al., Co_2 Capture from Humid Flue Gases and Humid Atmosphere Using a Microporous Coppersilicate. *Science* **2015**, *350*, 302-306.
17. Feldblyum, J. I.; Liu, M.; Gidley, D. W.; Matzger, A. J., Reconciling the Discrepancies between Crystallographic Porosity and Guest Access as Exemplified by Zn-Hkust-1. *J. Am. Chem. Soc.* **2011**, *133*, 18257-18263.
18. Kim, H. K.; Yun, W. S.; Kim, M.-B.; Kim, J. Y.; Bae, Y.-S.; Lee, J.; Jeong, N. C., A Chemical Route to Activation of Open Metal Sites in the Copper-Based Metal–Organic Framework Materials Hkust-1 and Cu-Mof-2. *J. Am. Chem. Soc.* **2015**, *137*, 10009-10015.
19. Li, Y.-N.; Wang, S.; Zhou, Y.; Bai, X.-J.; Song, G.-S.; Zhao, X.-Y.; Wang, T.-Q.; Qi, X.; Zhang, X.-M.; Fu, Y., Fabrication of Metal–Organic Framework and Infinite Coordination Polymer Nanosheets by the Spray Technique. *Langmuir* **2017**, *33*, 1060-1065.
20. Rodenas, T.; Luz, I.; Prieto, G.; Seoane, B.; Miro, H.; Corma, A.; Kapteijn, F.; Llabrés i Xamena, F. X.; Gascon, J., Metal–Organic Framework Nanosheets in Polymer Composite Materials for Gas Separation. *Nat Mater* **2015**, *14*, 48-55.
21. Peng, Y.; Li, Y.; Ban, Y.; Jin, H.; Jiao, W.; Liu, X.; Yang, W., Metal-Organic Framework Nanosheets as Building Blocks for Molecular Sieving Membranes. *Science* **2014**, *346*, 1356-1359.
22. Zhao, M.; Lu, Q.; Ma, Q.; Zhang, H., Two-Dimensional Metal–Organic Framework Nanosheets. *Small Methods* **2017**, *1*, 1600030-n/a.
23. Elder, A. C.; Aleksandrov, A. B.; Nair, S.; Orlando, T. M., Interactions on External Mof Surfaces: Desorption of Water and Ethanol from Cubdc Nanosheets. *Langmuir* **2017**, *33*, 10153-10160.
24. Hashimoto, Y.; Tanaka, S., A New Method of Generation of Gases at Parts Per Million Levels for Preparation of Standard Gases. *Environ. Sci. Technol.* **1980**, *14*, 413-416.
25. Bhattacharyya, S.; Pang, S. H.; Dutzer, M. R.; Lively, R. P.; Walton, K. S.; Sholl, D. S.; Nair, S., Interactions of So2-Containing Acid Gases with Zif-8: Structural Changes and Mechanistic Investigations. *J. Phys. Chem. C* **2016**, *120*, 27221-27229.
26. Mounfield, W. P., et al., Synergistic Effects of Water and So2 on Degradation of Mil-125 in the Presence of Acid Gases. *J. Phys. Chem. C* **2016**, *120*, 27230-27240.
27. Tan, K.; Nijem, N.; Gao, Y.; Zuluaga, S.; Li, J.; Thonhauser, T.; Chabal, Y. J., Water Interactions in Metal Organic Frameworks. *CrystEngComm* **2015**, *17*, 247-260.
28. Todaro, M.; Buscarino, G.; Sciortino, L.; Alessi, A.; Messina, F.; Taddei, M.; Ranocchiari, M.; Cannas, M.; Gelardi, F. M., Decomposition Process of Carboxylate Mof Hkust-1 Unveiled at the Atomic Scale Level. *J. Phys. Chem. C* **2016**, *120*, 12879-12889.
29. Guimon, C.; Gervasini, A.; Auroux, A., Xps Study of the Adsorption of So2 and Nh3 over Supported Tin Dioxide Catalysts Used in De-Nox Catalytic Reaction. *J. Phys. Chem. B* **2001**, *105*, 10316-10325.
30. Wagner, C. D.; Riggs, W. M.; Davis, L. E.; Moulder, J. F.; Mullenberg, G. E., *Handbook of X-Ray Photoelectron Spectroscopy*; Perkin-Elmer Corporation: Eden Prairie, Minnesota, 1979.
31. Brandt, C.; van Eldik, R., Transition Metal-Catalyzed Oxidation of Sulfur(Iv) Oxides. Atmospheric-Relevant Processes and Mechanisms. *Chem. Rev.* **1995**, *95*, 119-190.

32. Li, B.; Luo, X.; Zhu, Y.; Wang, X., Immobilization of Cu(Ii) in Kit-6 Supported Co3o4 and Catalytic Performance for Epoxidation of Styrene. *Appl. Surf. Sci.* **2015**, *359*, 609-620.
33. Téllez S, C. A.; Hollauer, E.; Mondragon, M. A.; Castaño, V. M., Fourier Transform Infrared and Raman Spectra, Vibrational Assignment and Ab Initio Calculations of Terephthalic Acid and Related Compounds. *Spectrochim. Acta, Part A* **2001**, *57*, 993-1007.
34. Arenas, J. F.; Marcos, J. I., Infrared and Raman Spectra of Phtalate, Isophtalate and Terephtalate Ions. *Spectrochimica Acta Part A: Molecular Spectroscopy* **1979**, *35*, 355-363.
35. Hintze, P. E.; Kjaergaard, H. G.; Vaida, V.; Burkholder, J. B., Vibrational and Electronic Spectroscopy of Sulfuric Acid Vapor. *J. Phys. Chem. A* **2003**, *107*, 1112-1118.
36. Haynes, W. M., *Crc Handbook of Chemistry and Physics : A Ready-Reference Book of Chemical and Physical Data*, 91st ed. ed.; CRC Press: Boca Raton :, 2009.
37. Zhu, B.; Lang, Z.-L.; Ma, N.-N.; Yan, L.-K.; Su, Z.-M., Bonding Interactions between Sulfur Dioxide (So2) and Mono-Ruthenium(Ii)-Substituted Keggin-Type Polyoxometalates: Electronic Structures of Ruthenium-So2 Adducts. *Phys. Chem. Chem. Phys.* **2014**, *16*, 18017-18022.

CHAPTER 8. CONCLUSIONS

Surface engineering is a crucial step in the development of next generation gas separation and catalysis technologies. Reliable techniques for characterizing distributions of surface functionalities are fundamentally important to this discipline. Mature surface analysis methods, such as X-ray photoelectron spectroscopy, provide a starting point for creating ever more sensitive and robust experiments. The ultimate goal of this branch of research is to be able to quantitatively determine the physical and chemical properties of solid surfaces in order to predict their utility engineering problems. The numerical techniques introduced and applied in this thesis bring us closer to that goal by enabling rational analysis of complex surface data.

The methods developed herein were targeted toward temperature programmed desorption. This experiment is frequently performed by members of the gas capture and catalysis communities. However, the existing literature on the topic of data analysis of TPD signals from complex surfaces is severely lacking. The forthcoming publication of concepts discussed in chapters 2, 3, 5, and 6 will address this problem and provide a rigorous foundation upon which more complex experiments and analysis techniques can be developed. The C++ software developed for variational Bayesian inference of surface distributions using TPD signals will also soon be released under an open source license. As demonstrated, this Bayesian approach can also be applied to Gaussian signal decomposition. In principle, it could also in principle be extended to deconvolution of mixtures of Gaussian and Lagrangian peaks.

There are a number of other directions that future work in this area could take. A particularly interesting addition would be to fit alternative parameterizations for amorphous surfaces presented in chapter 2.7. A wide range of distribution parameterizations could be used to probe the chemical structure of glass or polymeric surfaces. Additionally, experimental

apparatus with a wider range of temperature ramp rates and initial loadings could be used to explore surface and internal diffusion coefficients as well as pore-exit activation barriers. Finally, tandem TPD and XPS apparatus could be employed to measure the electronic structure of adsorbed gases in order to arrive at detailed mechanistic descriptions of solid-gas interactions at low temperatures.

APPENDIX A: SUPPORTING INFORMATION FOR CHAPTER 7

A.1 Crystal Orientation

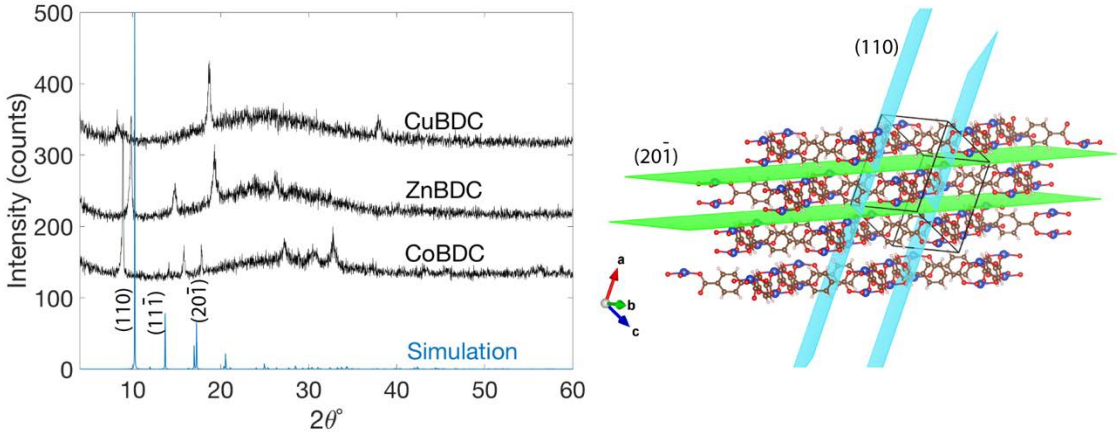

Figure A1. X-ray diffraction patterns of pristine M-BDC nanosheets and simulated diffraction pattern of CuBDC (left). Model of CuBDC nanosheets with lattice planes (right).

A.2 Control data

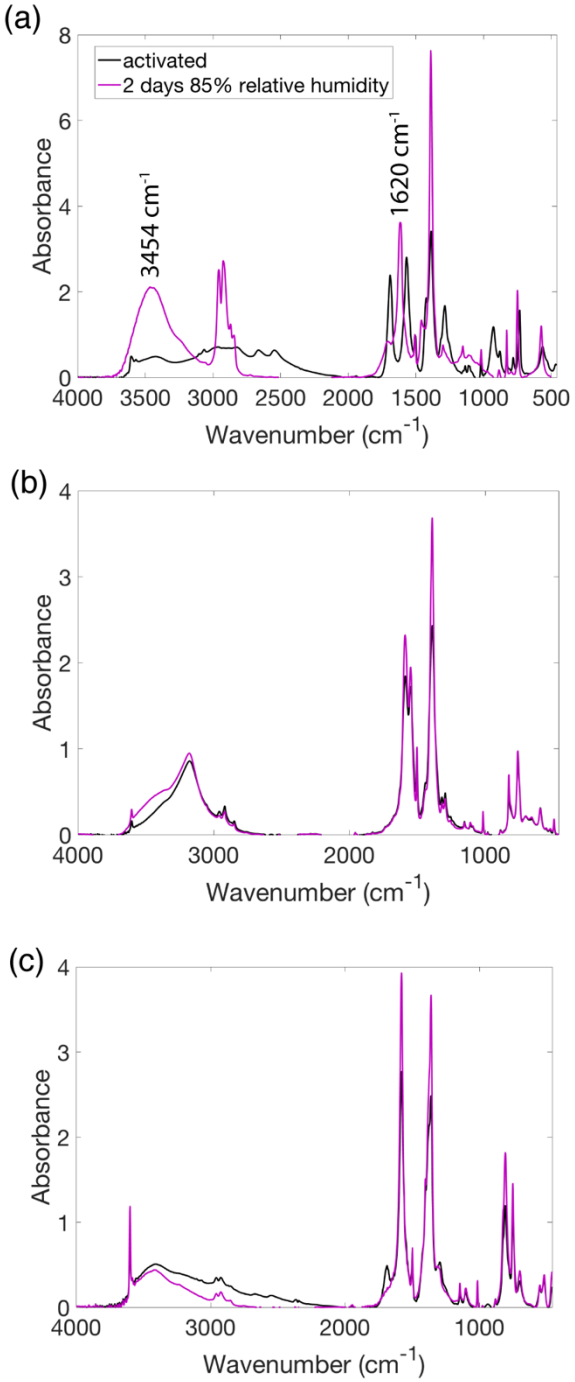

Figure A2. FTIR spectra of CuBDC (a), ZnBDC (b), and CoBDC (c) before (black), and after (violet) 2 days exposure to 85% relative humidity.

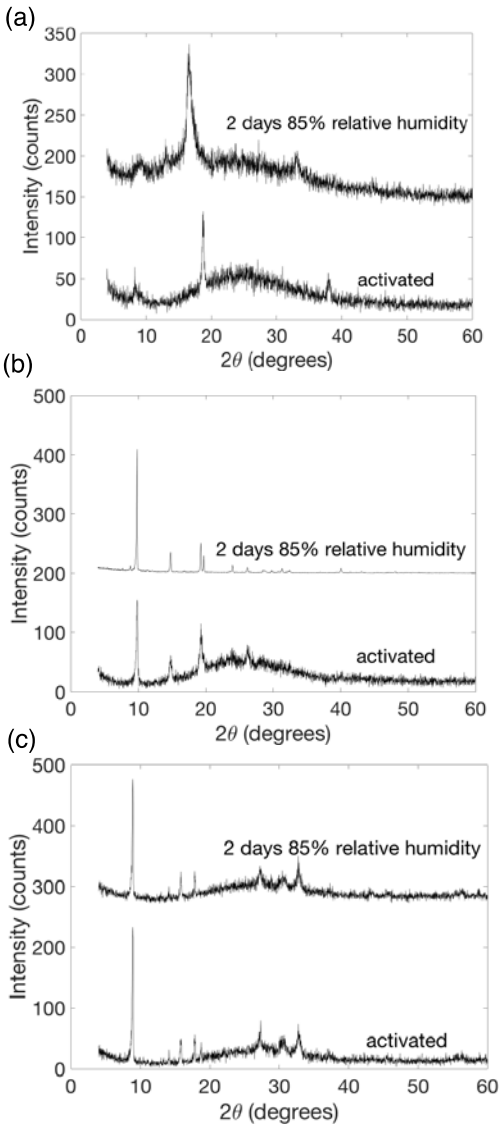

Figure A3. X-ray diffraction patterns of activated and control samples (exposed to 85% relative humidity for 2 days). CuBDC, ZnBDC, and CoBDC labelled (a), (b), and (c) respectively.

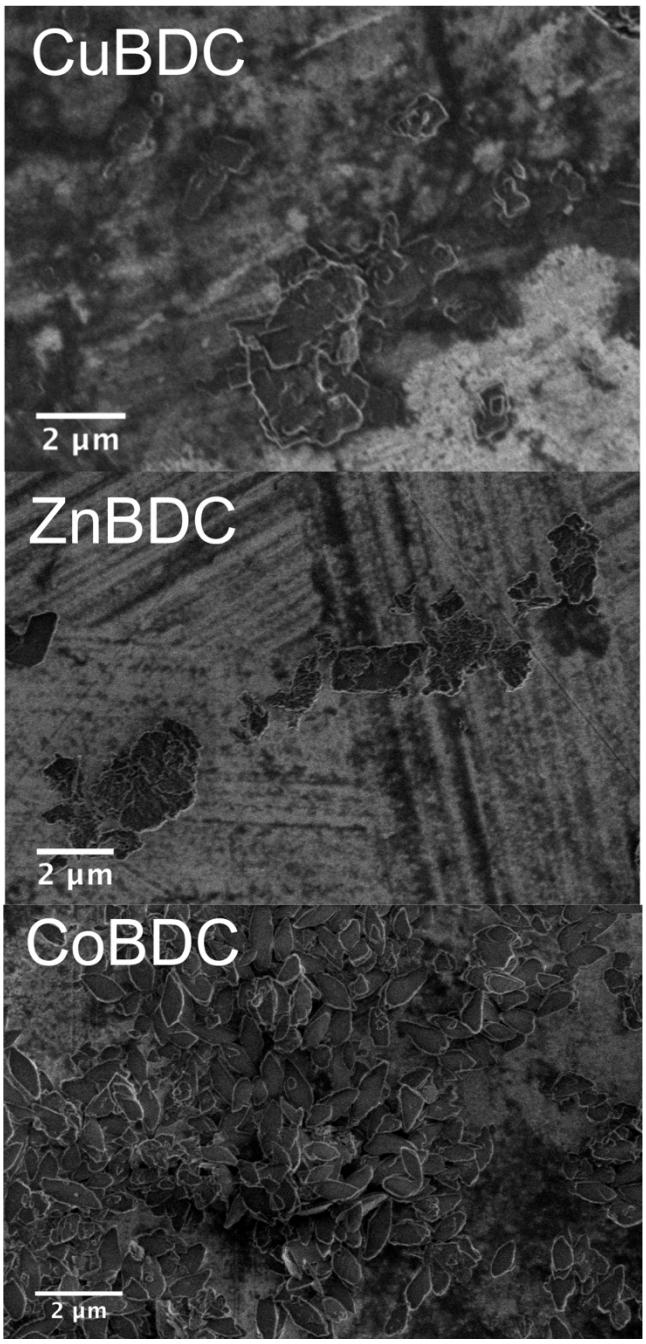

Figure A4. Scanning electron micrographs of CuBDC, ZnBDC, and CoBDC nanoparticles after two days exposure to 85% relative humidity.

A.3 Additional exposure data

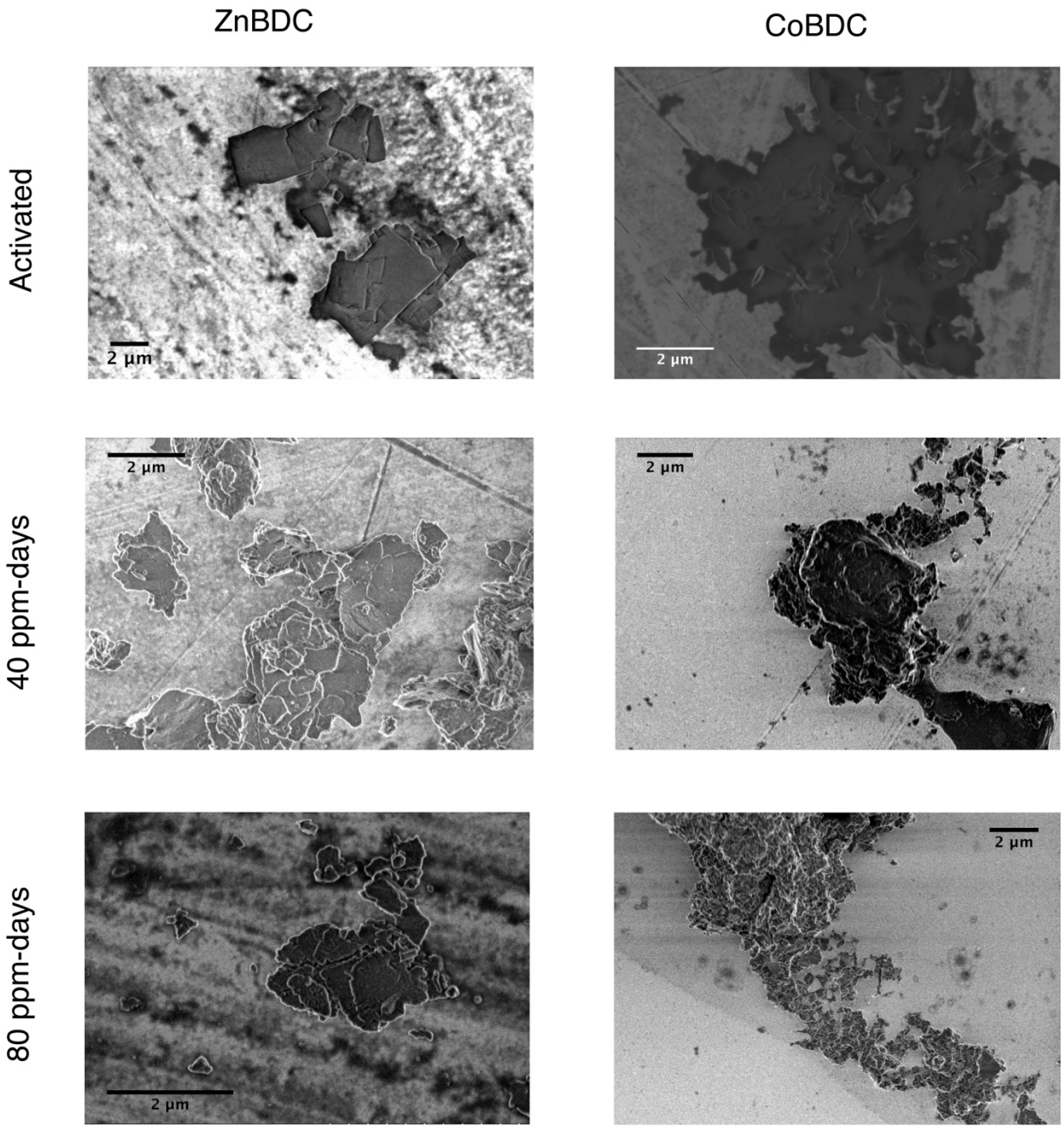

Figure A5. SEM images of ZnBDC and CoBDC nanosheets over progress of exposure to humid SO_2.

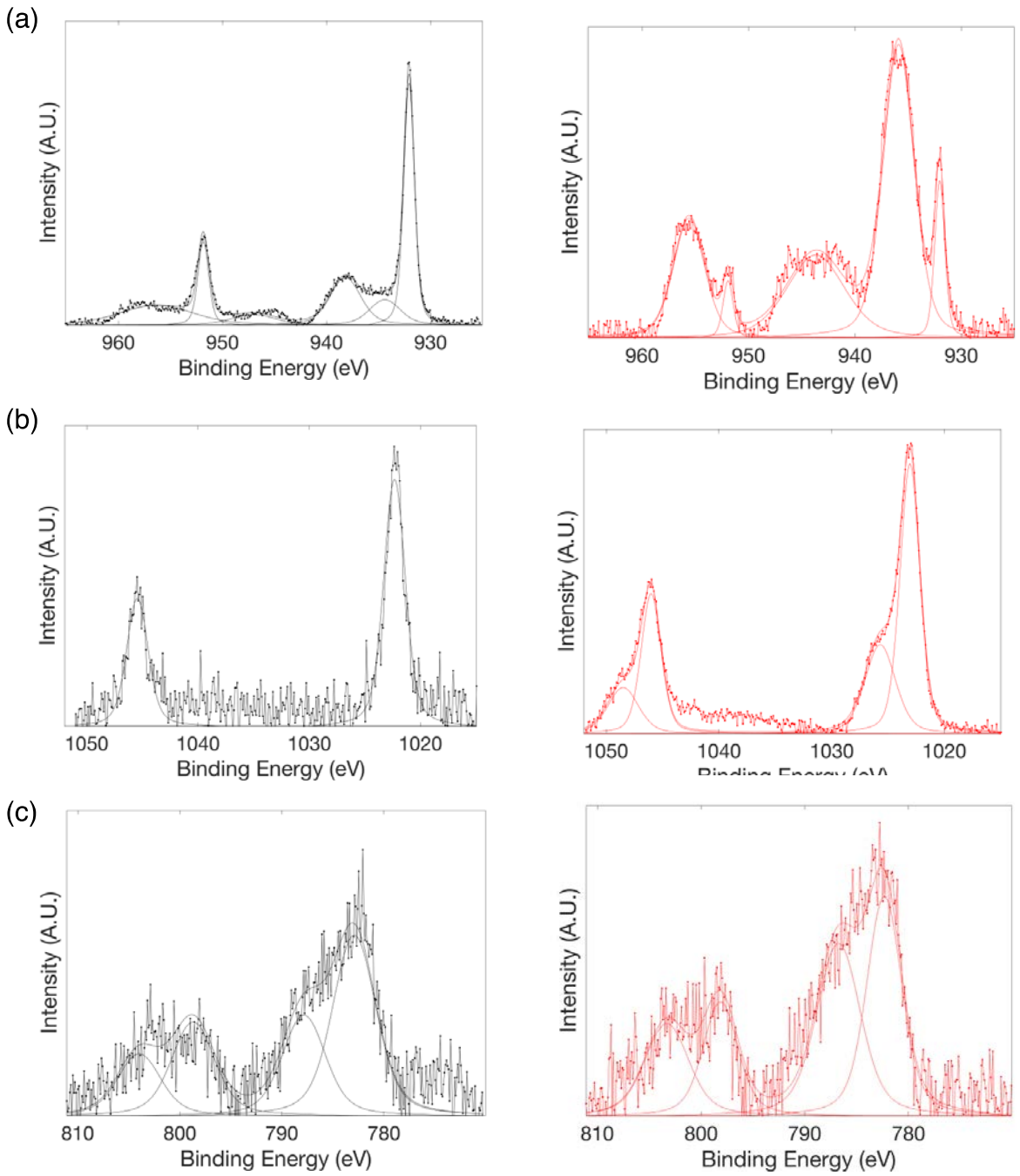

Figure A6. Metal XPS data from CuBDC (a), ZnBDC (b), and CoBDC (c) (Cu2p, Zn2p, and Co2p regions respectively). Data recorded after activation shown on the left and after 80 ppm-days humid SO_2 exposure shown on the right.

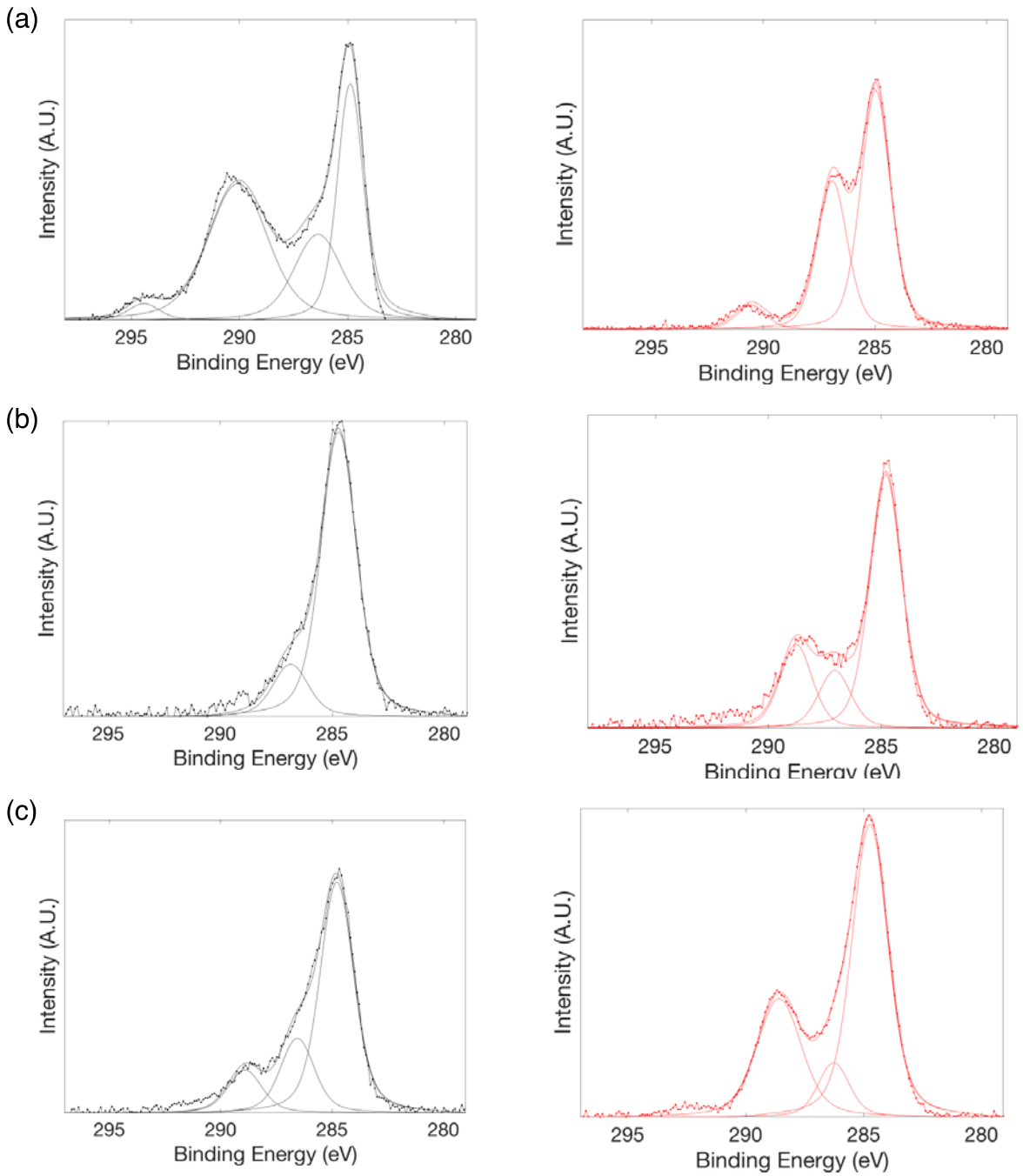

Figure A7. Carbon C1s XPS data from CuBDC (a), ZnBDC (b), and CoBDC (c). Data recorded after activation shown on the left and after 80 ppm-days humid SO_2 exposure shown on the right.